Technical University of Munich

Department of Physics

Physics of Energy Conversion and Storage

Impedance Analysis and Monitoring of Automotive Fuel Cells

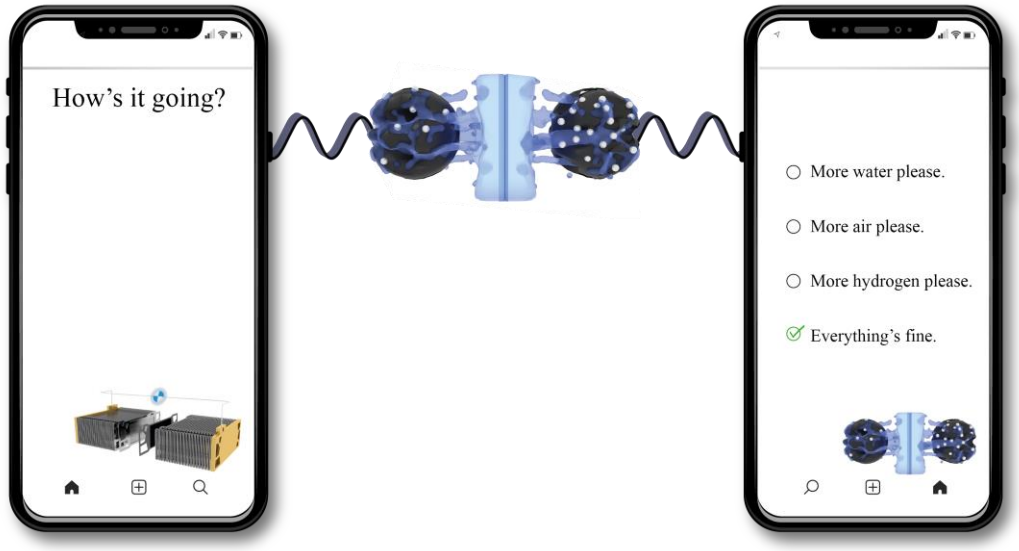

Dissertation

by

Tim Lochner

Department of Physics

Physics of Energy Conversion and Storage

Impedance Analysis and Monitoring of Automotive Fuel Cells

Tim Lochner

Vollständiger Abdruck der von der Fakultät für Physik der Technischen Universität München zur Erlangung des akademischen Grades eines

Doktors der Naturwissenschaften

genehmigten Dissertation.

Vorsitzende: Prof. Dr. Nora Brambilla

Prüfer der Dissertation:

1. Prof. Dr. Aliaksandr S. Bandarenka

2. Prof. Dr. Jens Oluf Jensen (Danmarks Tekniske Universitet)

Die Dissertation wurde am 15.02.2021 bei der Technischen Universität München eingereicht und durch die Fakultät für Physik am 24.03.2021 angenommen.

Abstract

Meeting customer expectations for future mobility will require several drive train technologies to exist in parallel, one of which is based on fuel cells. The performance and lifetime of fuel cell vehicles are determined by the membrane electrode assembly. This work uses electrochemical impedance spectroscopy and novel evaluation algorithms to identify operating conditions and malfunctions in real-time. The approach is based on the linearization of differential impedance analysis and has comparable accuracy to complex non-linear least-squares fitting algorithms. The impedance is measured at five frequencies in the range of the cathode kinetics between 119 Hz and 238 Hz, yielding the characteristic quantities of membrane resistance, charge transfer resistance, and cell capacitance. Operating conditions with not sufficient humidification or with too little supply of hydrogen or oxygen can be distinguished using these quantities.

A physical description of the charge transfer resistance was only possible with the assumption of a temperature-dependent transfer coefficient and diffusive components. The so-called charge transfer resistance in polymer electrolyte fuel cells thus describes not only the kinetics of the cathode but also the diffusion within the catalyst layer. In addition, a more inhomogeneous current density distribution along the air volume flow leads to a larger charge transfer resistance of the cell. Despite this increase in resistance, reactant starvation can still be recognized. However, it is not possible to distinguish between the anode or cathode starvation by evaluating the charge transfer resistance only.

Such a distinction can be made by analyzing the cell capacitance. In oxygen-free operation, the capacitance increases in the range from 0.0 V to 0.4 V due to hydrogen adsorption on the catalyst. The higher the oxygen content, the lower the cell capacitance. At 15 vol.% O_2 and higher, the cell capacitance corresponds to the double layer capacitance. The *OH-adsorption during the reduction of oxygen occurs quickly below 0.4 V. That is why we assume that measurement frequencies up to 1 kHz are too small to detect this process.

Consequently, oxygen starvation can be identified by an increase in cell capacitance, provided that the cell voltage is below 0.4 V.

To determine the dominant degradation mechanisms of fuel cells during vehicle operation, tests were conducted based on customer driving profiles. Local hydrogen starvation due to water droplet formation was found to cause performance loss. The origin was the transition from a wet operating point with high current density to a low load point. Cracks formed within the cathode catalyst layer, and this allowed the increased accumulation of liquid water in these areas. The impedance monitoring method developed here can detect this malfunction, supporting fuel cell performance and lifetime optimization.

An impedance-based operating strategy is proposed for future research. The main challenge is modeling the mass transport behavior and a more advanced understanding of the capacitance. Impedance spectroscopy can replace costly sensor technology and establish direct “communication” with the electrochemically active layer during vehicle operation.

Zusammenfassung

Um Erwartungen an die Mobilität der Zukunft erfüllen zu können, werden mehrere Antriebstechnologien parallel existieren. Die Leistung und Lebensdauer von Brennstoffzellenfahrzeugen werden durch die Membran-Elektroden-Einheit bestimmt. Diese Arbeit nutzt elektrochemische Impedanzmessungen und neuartige Auswertealgorithmen, um Betriebszustände und Fehlverhalten in Echtzeit zu identifizieren. Der Ansatz basiert auf einer Linearisierung der differentiellen Impedanzanalyse und hat eine vergleichbare Genauigkeit zur iterativen Annäherung des Impedanzverhaltens an elektrische Ersatzschaltbilder. Gemessen wird das Übertragungsverhalten an fünf Frequenzpunkten im Bereich der Kathodenkinetik zwischen 119 Hz und 238 Hz, wobei man die charakteristischen Größen Membranwiderstand, Durchtrittswiderstand und Zellkapazität erhält. Betriebszustände, in denen zu wenig Feuchte, Wasserstoff oder Sauerstoff vorhanden ist, können mit diesen Größen unterschieden werden.

Eine physikalische Beschreibung des Durchtrittswiderstands war nur unter der Annahme eines temperaturabhängigen Transferkoeffizienten und diffusiver Anteile möglich. Der sogenannte Durchtrittswiderstand in Polymerelektrolytbrennstoffzellen beschreibt somit nicht ausschließlich die Kinetik der Kathode, sondern auch die Diffusion von Sauerstoff und Protonen in der Katalysatorschicht. In einem beliebigen Betriebspunkt führt zudem eine inhomogenere Verteilung der Stromdichte entlang des Luftvolumenstroms zu einem größeren Durchtrittswiderstand der Zelle. Trotz dieser Quereinflüsse werden Probleme in der Versorgung mit Reaktanden erkannt. Der Durchtrittswiderstand allein lässt jedoch keine Unterscheidung zwischen Wasserstoff- und Sauerstoffverarmung zu.

Eine solche Unterscheidung ermöglicht die Analyse der Zellkapazität. Im sauerstofffreien Betrieb ist die Kapazität im Bereich von 0.0 V bis 0.4 V stark erhöht, was durch die Wasserstoffadsorption am Katalysator verursacht wird. Je mehr Sauerstoff an der Kathode vorhanden ist, desto geringer wird die Zellkapazität, bis diese ab einem Anteil von

15 vol.% O_2 der Doppelschichtkapazität entspricht. Die *OH-Adsorption bei der Reduktion von Sauerstoff läuft unter einem Potential von 0.4 V sehr schnell ab. Es wird vermutet, dass Messfrequenzen unterhalb von 1 kHz nicht ausreichen, um dies zu detektieren. Da die *OH-Adsorption diese Frequenzen nicht beeinflusst, kann eine Sauerstoffunterversorgung im Betrieb durch den Anstieg der Zellkapazität identifiziert werden kann, sofern die Zellspannung unter 0.4 V ist.

Um die dominanten Degradationsmechanismen von Brennstoffzellen im Fahrzeug zu bestimmen, wurden Tests basierend auf Fahrprofilen von Kunden durchgeführt. Die lokale Wasserstoffunterversorgung aufgrund von Tropfenbildung trug dabei maßgeblich zum Leistungsverlust der Zelle bei. Als Ursache dafür wurde der Übergang von einem feuchten Betriebspunkt mit hoher Stromdichte zu einem Niedriglastpunkt identifiziert. Die Unterversorgung verursachte Bruchstellen innerhalb der Kathoden-Katalysatorschicht, welche die Ansammlung von flüssigem Wasser bestärkte. Die hier entwickelte Methode zur Echtzeit-Überwachung der Impedanz kann dieses Fehlverhalten prinzipiell erkennen und unterstützt somit die Optimierung der Leistung und der Lebensdauer von Brennstoffzellen.

Für zukünftige Arbeiten wird eine Bewertungsstrategie der Impedanz vorgeschlagen, wobei die größten Herausforderungen die Modellierung des diffusiven Verhaltens sowie ein weitergehendes Verständnis der Zellkapazität sind. Die Impedanzspektroskopie hat das Potential kostspielige Sensorik zu ersetzen und eine direkte Kommunikation mit der elektrochemisch aktiven Schicht während des Fahrzeugbetriebs herzustellen.

Acknowledgement

In the following, I would like to thank some people who supported me during my PhD. First of all, I thank my professor Dr. Aliaksandr Bandarenka who was always available and efficiently guided the work in the right direction. I also would like to thank Dr. Markus Perchthaler for the inspiring supervision in the last years, which gave me both creative freedom without losing sight of the goal. It was a real pleasure working with you the last few years. That the balancing act between TUM and BMW never became complicated is thanks to the always open and productive communication between Aliaksandr, Markus and my team leader Dr. Olav Finkenwirth, which I found particularly remarkable in the current turbulent times of industrial promotions.

To Dr. Alin Orfanidi, Dr. Albert Albert, Tuan Anh Dao, and Fengmin Du, I thank you for the enlightening discussion on theory and experiments. Also, the linking of simulation and experiment would not have been possible without the support of Dr. Simon Enz. I would like to thank my colleagues Dr. Andreas Bauer, Krzysztof Jozwiak and Michael Obermaier for their devoted imaging. I am very grateful to Jarek Sabawa for the consistent test bench support and the good exchange around the PhD.

Without the commitment of the students Daniel Sick, Janina Förtsch, Janko Binder, Franziska Hnyk, and Laurens Hallitzky, which went beyond expectations, many results of this work would not have been achieved. The discussions were always enriching and brought us closer to our goal step by step.

I would like to thank Dr. Emma Farndon and Simeon Ziegeler for the support in English and the little extra in some wording. I am also extremely grateful for the unexpected and intensive help in clarifying and structuring my thoughts from Andreas Gusak. Also, many thanks to my brother Jonas and his girlfriend Fiona for the outside view on my attempts to explain this PhD topic and for the linguistic support.

Special thanks go to Nina Dutzel for the creative impulse in questions about image design. Also, thanks to my research group at TUM, especially Dr. Johannes Fichtner, Dr. Sebastian Watzele and Dr. Batyr Garlyyev, for the necessary input on how to write such a thesis in the first place. I would also like to thank Regina Kluge for the good professional and artistic cooperation.

Finally, I would like to express my special thanks to my parents and my siblings. Without your support, which is so self-evident, the last few years would have been more stressful, less efficient and less fun.

List of publications

1. T. Lochner, L. Hallitzky, M. Perchthaler, M. Obermaier, J. Sabawa, S. Enz, A. S. Bandarenka. Local degradation effects in automotive size membrane electrode assemblies under realistic operating conditions. *Appl. Energy* **2020**, *260*, 114291.

2. T. Lochner, M. Perchthaler, J. T. Binder, J. P. Sabawa, T. A. Dao, A. S. Bandarenka. Real-Time Impedance Analysis for the On-Road Monitoring of Automotive Fuel Cells. *ChemElectroChem* **2020**, *7*, 2784-2791.

3. T. Lochner[(1)], R. M. Kluge[(1)], J. Fichtner[(1)], H. A. El-Sayed, B. Garlyyev, A. S. Bandarenka. Temperature Effects in Polymer Electrolyte Membrane Fuel Cells. *ChemElectroChem* **2020**, *7*, 3545-3568.

4. T. Lochner, M. Perchthaler, F. Hnyk, D. Sick, J. P. Sabawa, A. S. Bandarenka. Analysis of the Capacitive Behavior of Polymer Electrolyte Membrane Fuel Cells during Operation. *ChemElectroChem* **2020**, *8*, 96-102.

5. M. Obermaier, M. Rauber, A. Bauer, T. Lochner, F. Du, C. Scheu. Local Fuel Starvation Degradation of an Automotive PEMFC Full Size Stack. *Fuel Cells* **2020**, *20*, 394-402.

6. J. P. Sabawa, F. Haimerl, F. Riedmann, T. Lochner, A. S. Bandarenka. Dynamic and precise temperature control unit for PEMFC single-cell testing. *Eng. Rep.* **2020**, DOI 10.1002/eng2.12345.

List of presentations

1. 25th Topical Meeting of the International Society of Electrochemistry, “New electrochemical processes for energy and the environment”, **2019**, Toledo Spain (oral presentation).

2. ProMotion Dialogtag of the BMW Group, **2019**, Munich Germany (oral presentation).

List of abbreviations

Abbreviations

AC	Alternating current
BEV	Battery electric vehicle
BPP	Bipolar plate
CCM	Catalyst-coated membrane
CDD	Current density distribution
CNLS	Complex non-linear least-squares
CO_2	Carbon dioxide
COR	Carbon oxidation reaction
CSD	Current scan device
CV	Cyclic voltammetry or cyclic voltammogram
DC	Direct current
DIA	Differential impedance analysis
ECSA	Electrochemical active surface area
EEC	Equivalent electric circuit
EIS	Electrochemical impedance spectroscopy or spectra
FCEV	Fuel cell electric vehicle
GDL	Gas diffusion layer
H^*	Adsorbed hydrogen
H_2	Molecular hydrogen
HER	Hydrogen evolution reaction
HFR	High-frequency resistance
HOR	Hydrogen oxidation reaction
HUPD	Hydrogen underpotential deposition
LOM	Local operating model
MEA	Membrane electrode assembly
N_2	Molecular nitrogen
$^*OH$	Adsorbed OH
O^*	Adsorbed oxygen
O_2	Molecular oxygen

OCV	Open circuit voltage
OER	Oxygen evolution reaction
ORR	Oxygen reduction reaction
PEMFC	Polymer electrolyte membrane fuel cell
Pt	Platinum
PTFE	Polytetrafluorethylene
RTIM	Real-time impedance monitoring
SEM	Scanning electron microscope
SU	Setup
THDA	Total harmonic distortion

Symbols

A	Area
b	Tafel slope
C	Capacitance
c_{ref}	Oxygen concentration in the flow field
D_b	Oxygen diffusion coefficient in GDL
F	Faraday constant
f	Frequency
i	Current
i	Imaginary unit ($i^2 = -1$)
$\hat{I}$	Current amplitude in impedance measurement
j	Current density
$j_{0,ORR}$	Exchange current density of the ORR
l_b	GDL thickness
L_{eff}	Effective inductance
l_t	Catalyst layer thickness
$\dot{n}$	Molar flow
N_A	Molar volume at standard conditions
p	Gas pressure
P	Arbitrary parameter
Q	Electric charge

q	Electric charge normalized to oxygen-free conditions
R	Resistance and Universal gas constant
R^2	Goodness of fit using root mean square method
RH	Relative humidity
t	Time
T	Time constant
T_{cell}	Cell temperature
U	Voltage
$\hat{U}$	Voltage amplitude in impedance measurement
V	Volume
$\dot{V}$	Volume flow
W	Warburg element
W_{short}	Finite-length Warburg element
x_{Rct}	Air stoichiometry indicator
z	Number of electrons participating in the reaction
Z	Impedance
Z_{Im}	Imaginary part of the impedance
Z_{Re}	Real part of the impedance
α	Transfer coefficient
β	Symmetry factor
η	Overpotential
κ_{ion}	Ionic conductivity
λ	Stoichiometry for gaseous reactants, membrane water content
υ	Sweep rate for cyclic voltammograms
φ	Electrode potential and phase shift in impedance measurements
ω	Angular frequency

Subscripts

a	Anode
abs	Absolute value
Active	Active (Area)
ads	Adsorption
air	Air

bal	Balanced (Area)
c	Cathode
calc	Calculated value
CDD	Current density distribution
cell	Fuel cell
ch	Channel
ct	Charge transfer
diff	Diffusion
dl	Double layer
Faraday	According to Faraday’s law of electrolysis
H_2	Hydrogen
HUPD	Hydrogen underpotential deposition
inlet	Position where the gas enters the fuel cell
mean	Mean value
meas	Measured value
mem	Membrane
outlet	Position where the gas exits the fuel cell
par	Parasitic
Pt	Platinum
SEM	Scanning electron microscope
sim	Simulated value
supply	Supplied to the fuel cell
tot	Total

Content

1 Relevance of Fuel Cell Electric Vehicles and Research Motivations

"... various alternative powertrain systems will exist alongside one another in future, as there is no single solution that addresses the full spectrum of customers' mobility requirements worldwide." (BMW Group Press Release 2020).[1]

1.1 The Rise of Renewable Energy Sources

In 2015 world-leading scientists concluded that reducing greenhouse gas emissions is inevitable to prevent dangerous interference with the climate system, and maintain sustainable food production and economic development.[2,3] Global oil supply is dominated by local players,[4] making the energy networks of countries without fossil fuels vulnerable, thereby increasing the likelihood of international conflicts.[5] Urban air pollution from the combustion of fossil fuels causes high cardiovascular and respiratory mortality rates,[6] leading people in heavily affected cities to buy more battery electric vehicles (BEVs).[7] Consequently, the share of renewable energy sources on the total final energy consumption[a] increased annually by 3% since 2007 in OECD countries.[8] In 2019, 94% of the world's installed renewable energy capacity provided energy in the form of electricity, with hydropower, wind power and photovoltaics being the primary sources, while other technologies such as bio- and geothermal power still have small contributions.[8]

[a] The total final energy consumption is the amount of energy that is made available to the consumer (e.g. industry, households, agriculture, transport sector).

As most renewable energies supply energy in the form of electricity, electrification of processes is a powerful instrument to reduce global greenhouse gas emissions.[9,10] The transport sector accounted for one-quarter of global CO_2-emissions (status 2018)[11] since fossil fuels are the main energy source for cars, trucks, buses, ships and airplanes. Batteries can link renewable electricity and electric motors to replace combustion engines and electrify transport applications. This is already being consistently implemented for passenger cars (e.g. BMW iX3, VW ID3, Tesla). The sale of BEVs was increasing strongly in recent years, reaching a global market share[b] of 2.6% and even 4.9% in China in 2019.[12,13]

It is not enough to electrify passenger cars to achieve the climate goals of the Paris Agreement of 2015;[2] all sectors (industry, energy, transport, agriculture, chemicals, etc.) must operate on a greenhouse gas-free basis. Heavy industry (e.g. steel, cement and glass manufacturing) is essential as this accounts for one-third of the global greenhouse gas emissions (status 2015).[11,14] Fossil sources facilitate nowadays the production of steel, glass and ammonia. Ore is converted to steel using coke, releasing CO_2.[15] Glass is produced by melting limestone or dolomite, releasing CO_2.[16] Ammonia (e.g. fertilizer for agricultural processes) is produced from coal, natural gas, or heavy oil, releasing CO_2.[17] Hydrogen is an alternative to fossil fuels in steel, glass and ammonia production.[18,19,30] When hydrogen is produced from renewable electricity, the heavy industry emissions switch from CO_2 to water.

Wind and solar power accounted for 30% of the global renewable electricity production in 2018[20] and its shares increased in recent years, especially in the European Union.[21] To utilize hourly and multi-day fluctuations in renewable power generation, storage technologies are necessary. As batteries have high conversion efficiencies and high cost per capacity, they are economically feasible to counterbalance short-term fluctuations, especially from photovoltaic systems.[22] Hydrogen storage shows a lower well-to-wheel efficiency[c] when, e.g., used in fuel cell electric vehicles (FCEVs), but the storage cost per

[b] Market share is the share of new electric vehicle registrations as a percentage of total new vehicle registrations.[13]

[c] Well-to-wheel efficiency describes the combination of all efficiencies from the energy supply (e.g. with wind and solar power) to the kinetic energy of the vehicle.

capacity is lower compared to batteries, and therefore, it is cost-optimal to balance multi-day and seasonal fluctuations of wind power.[22,23,29]

BEVs are heavy, have shorter driving ranges and longer refueling times compared to internal combustion engine vehicles,[24,25] which limits the commercial use e.g. for taxis, trucks and buses, as these applications need to maximize the availability of the vehicle to be competitive. To overcome range and refueling barriers, hydrogen fuel cells can serve e.g. as a range extender in BEVs, to increase the technical feasibility and fully electrify the transport sector.[24,25,26,27] The well-to-wheel efficiency of BEVs is higher than that of FCEVs,[28] thus more installed renewable energy power is needed when using FCEVs in the transport sector.[29]

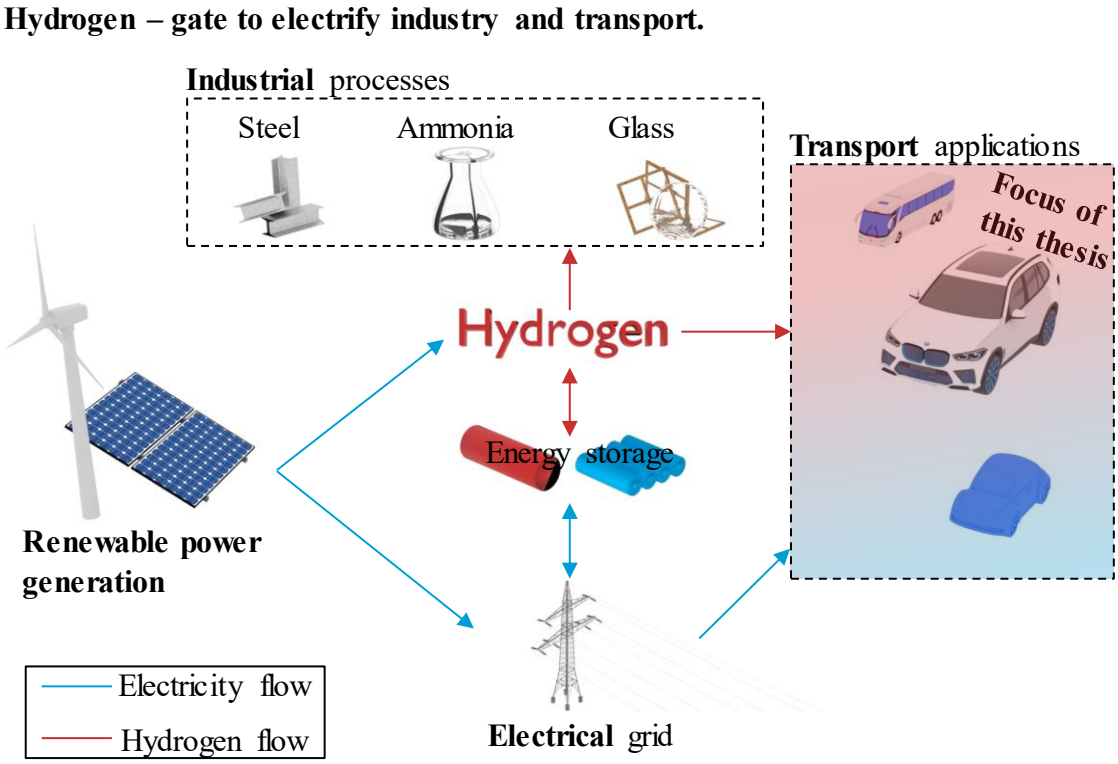

Figure 1.1. Energy flow chart using hydrogen to electrify industrial processes, balance power generation fluctuations and fuel transport applications.[30]

As hydrogen will be produced in electrolyzers from water and electricity, it links renewable electricity with the chemical and heavy industry while complementing BEVs in the transport sector (**Figure 1.1**).[30,31,32] Hydrogen is a feedstock that enables the electrification

and decarbonization of many processes that currently have severe greenhouse gas emissions. Therefore, many states such as Japan, China, California and Germany consider implementing a hydrogen infrastructure and initiated hydrogen strategies. The cost of hydrogen is a critical barrier for this technology, as this accounts for e.g. ~80% of the total cost in ammonia production,[30] which explains why the production of ammonia nowadays continues to rely on fossil fuels.

1.2 Hydrogen Fuel Cells for Transport Applications

Many car manufacturers,[33,34,35,36,37] like the BMW Group, continue to invest in low-carbon emission technologies such as the fuel cell drive train.[38] Hydrogen as a fuel for mobility applications is the economically most promising market.[39] The global amount of FCEV passenger cars increased by 69% from 2018 to 2019[40] while the number of hydrogen refueling stations nearly tripled (**Figure 1.2**).[41] Several governments are working on an expansion of green drive train technologies by banning the sale of combustion engines[42] and setting target numbers for FCEVs. Great Britain, France and California announced that they would no longer register vehicles with combustion engines from 2040.[43] In 2025, California, China and Japan are targeting a total of ~300,000 FCEVs on the roads, which will increase to about three million in 2030.[44,45,46,47]

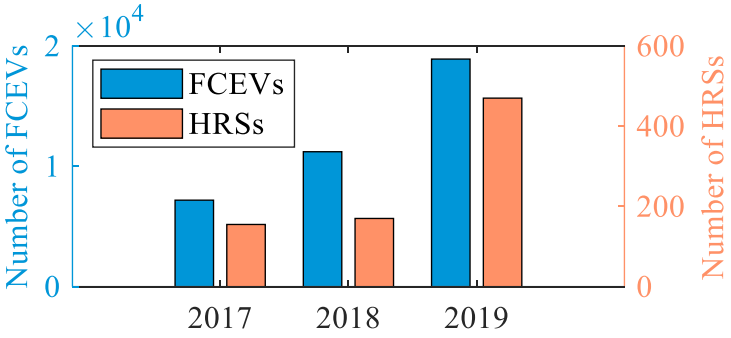

Figure 1.2. Global amounts of fuel cell electric vehicles (FCEVs, blue) and hydrogen refueling stations (HRS, orange) from 2017 to 2019.[40,41]

The polymer electrolyte membrane fuel cell (PEMFC) is the most common fuel cell type used for transport applications due to its high power density, low start-up times, ability to

respond to rapid load changes, non-corrosive electrolyte, high voltage, tolerance to CO_2, and its compact and simple design.[48] A disadvantage of PEMFCs is the use of platinum as a catalyst, which is expensive, as the global supply is currently 90% dependent on a single country (South Africa),[49] and other growing markets, such as the glass industry, compete for platinum.[50] One of the major technical challenges for FCEVs is the low gravimetric density of hydrogen,[51,52] which limits the range due to the installation space in vehicles. Therefore, the efficiency of the fuel cell system plays an essential role in increasing the driving range. To be competitive to battery electric and combustion engine vehicles, the reliability and durability of FCEVs must be further improved.[32,53,54,55,56] The water management of fuel cells is vital, as this triggers the dominant lifetime limiting mechanisms. Condensation of water inside the fuel cells blocks the hydrogen gas stream leading to non-reversible performance losses.[57,58,59,60] When water is absorbed, the polymer membrane swells. When water is released, it shrinks. Thus, varying water contents of the membrane lead to mechanical stress, which results in pinholes and cracks inside the membrane.[59,61,62] Pinholes are a safety risk, as the membrane does not anymore prevent direct contact between hydrogen and oxygen. Expert surveys show that, apart from the catalyst, the most critical component for the service life of a fuel cell system is the membrane.[63]

It is crucial to have real-time information on the membrane water content during operation to overcome efficiency, reliability and degradation issues in FCEVs. Electrochemical impedance spectroscopy (EIS[d]) is an *operando* technique that does not interfere with system operation and provides information on operational parameters such as membrane humidification.[64,65,66,67,68,69] For an EIS measurement, the fuel cell is excited and the response signal is evaluated. To interpret the response, physical models of the fuel cell are needed.[70,71,72,73,74,75,76] EIS is used as a real-time indicator for water content in FCEVs using several simplifications of the aforementioned physical models.[77,78,79,80,81,82]

[d] The abbreviation EIS stands for electrochemical impedance spectroscopy and electrochemical impedance spectra.

1.3 Aim of this Research

In addition to membrane hydration, the EIS signal also contains information on other operating parameters such as cell temperature, hydrogen supply, and air supply.[65,66,83,84,85] Optimization of these parameters during vehicle operation reduces fuel consumption and extends the durability of the FCEV. Current EIS real-time analysis on fuel cell systems is mainly empirical. This is primarily due to the long measurement times of several minutes required to describe an EIS measurement with physical models. Nevertheless, impedance data analysis based on such models allows the determination of critical operating parameters. If materials or geometries of a fuel cell are changed, a new performance map must be determined for empirical models. In contrast, physical models have the advantage that only characteristic parameters must be adjusted.

If the EIS analysis reliably determines operating parameters, it can also serve as input for safety concepts, thus saving costs for temperature and other sensors.[86] This thesis attempts to contribute to understand further the link between empirical results and physical impedance models on PEMFCs, resulting in the following tasks:

1. Design a measurement method for impedance data acquisition and processing to analyze automotive size fuel cells and stacks in real-time, whereby a physical interpretation of the data should still be possible.

2. Develop a physical interpretation of impedance data of a PEMFC during automotive operation in normal and critical operating states.

3. Identify detectable critical operating conditions using the EIS signal to create a reliable impedance sensing technique that is universally applicable to PEMFCs.

This thesis contributes to (1) lowering the cost of sensors in the system, (2) increase the lifetime of fuel cells, (3) optimize the hydrogen consumption of the system, and thus maximize the benefits of FCEVs for the customer.

2 Theoretical Considerations on Fuel Cells and Impedance Spectroscopy

Parts of this chapter were published by the author of this thesis (among others) in the article 'Temperature Effects in Polymer Electrolyte Membrane Fuel Cells'.[87]

The following chapter describes relevant failure modes during fuel cell operation and impedance spectroscopy to detect them. An introduction of the underlying electrocatalytic reactions to the operation of a fuel cell stack is given in section 2.1. The next part (2.2) explains the relevant malfunctions that occur in FCEVs. Section 2.3 describes and evaluates key concepts of EIS, and (section 2.4) how the related resistances and capacitances are used to monitor the operating parameters of fuel cells.

2.1 Operating Conditions – from Electrocatalysis to Fuel Cell Stacks

This chapter describes the ideal operation and related malfunctions on different levels of a fuel cell, starting at the electrocatalytic layers in chapter 2.1.1, the membrane electrode assembly (MEA) in chapter 2.1.2, the fuel cell in chapter 2.1.3, and finally, the fuel cell stack (chapter 2.1.4).

2.1.1 Electrocatalysis

The membrane and catalyst layers are the most critical components in terms of the lifetime of a fuel cell.[63] To protect them, it is crucial to ensure that the electrochemical reactions

can occur as intended during system operation. An illustration of a catalyst-coated membrane (CCM) is given in **Figure 2.1**.

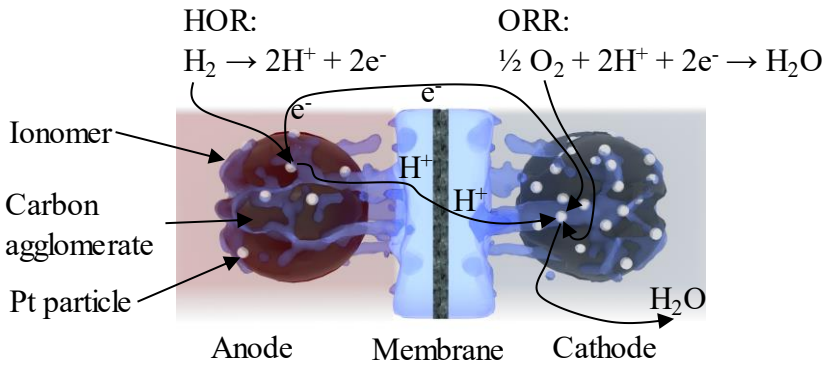

Figure 2.1. Catalyst-coated membrane, including the electrochemical reactions of anode and cathode. Abbreviations: Hydrogen oxidation reaction (HOR), oxygen reduction reaction (ORR). Inspired by Yamada *et al*.[88]

A fuel cell generates electricity at an ideal voltage of 1.23 V at standard conditions[89] by converting hydrogen and oxygen to water (**Figure 2.1**). The corresponding electrochemical reactions take place in the catalyst layers. At the anode, hydrogen is converted to protons and electrons, which is called hydrogen oxidation reaction (HOR).[90] At the cathode, the protons and electrons originating from the HOR are recombined with oxygen to form water; this is the oxygen reduction reaction (ORR).[91] Electrons can flow within the catalyst layers, and an external electric circuit conducts them from the anode to the cathode.[92] This external electrical circuit allows the utilization of power from the electrochemical reaction.

The HOR and ORR typically take place on a platinum-based catalyst immobilized on a carbon support, as shown in **Figure 2.1**.[93] The HOR kinetics is very fast, leading to voltage losses in the range of ~5 mV during operation, and therefore the anode platinum loading is relatively low (~0.05 $mg_{Pt}/cm^2_{electrode}$).[90] The ORR is limited by kinetics and also by diffusion. The catalyst loading should be high to increase the amount of reaction sites and reduce the travel length for oxygen diffusion (~0.2 $mg_{Pt}/cm^2_{electrode}$).[90,94,95] The required amount of hydrogen and oxygen for the reaction depends on the electrical current between anode and cathode. For the PEMFC to deliver a certain current i_{tot}, the volume flows of hydrogen and oxygen must comply with Faraday's law of electrolysis.

Thereby, $\dot{V}_{Faraday} = i_{tot} N_A z^{-1} F^{-1}$, where the number of electrons participating in the reaction z is four for O_2 and two for H_2, F is the Faraday constant (96485 C mol^{-1}) and N_A is the molar volume at standard conditions ($22.4 \cdot 10^{-3}$ m^3 mol^{-1}). Ideally, the electric current in the electrocatalytic layer i_{tot} corresponds to the current transferred *via* the external circuit i_{cell}. We label any additional effects as parasitic currents i_{par} and therefore $i_{tot} = i_{cell} + i_{par}$.[96]

A proton-conducting phase, the ionomer (bluish film in **Figure 2.1**), covers the catalyst to expand the electrochemical active region into the electrode bulk and to increase the mechanical stability of the carbon particles.[97] The catalyst and ionomer need to be well distributed on the carbon support to reduce oxygen mass transport losses.[98] The membrane material is typically made of perfluorosulfonic acid with a central mechanical reinforcement based on woven polytetrafluorethylen (PTFE) fabrics.[99] Main functions of the membrane are (1) reactant gas separation, (2) electrical electrode separation and (3) the transfer of protons between anode and cathode.[100,101] As high power densities and therefore, high current densities (3 A cm^{-2} to 5 A cm^{-2}) need to be achieved for automotive fuel cell operation, minimizing the ohmic losses across the polymer membrane is essential. This led to a continuous decrease in membrane thickness to about 10 µm nowadays.[102]

This thesis deals with the detection of critical operating conditions. As the CCM is the most vulnerable component of an FCEV,[63] the system needs to ensure an undisturbed operation. This can be structured into three basic functions, namely (1) the molar flows of hydrogen and oxygen correspond to Faraday's law of electrolysis, (2) protons can move from anode to cathode, and (3) electrons can move from anode to cathode. Typical issues related to (1) are water droplets inside the catalyst layer as they hinder gas diffusion,[95,96] electrical shorts and gas leakages across the membrane, which increase the parasitic currents.[103] The proton transfer between anode and cathode depends on the water content of the polymer phase and is inhibited in case of a poor contact area between polymer and carbon particles.[95] Delamination of the fuel cell layers additionally impedes the electron transfer between anode and cathode.[104]

When operating a fuel cell, the corresponding parameters should avoid the problems mentioned above, such as droplet formation, electrical short circuits or delamination between the layers. The electrochemical fuel cell reactions as illustrated in **Figure 2.1** take

place at certain temperatures (20 °C to 120 °C), polymer water contents λ_{mem}[e] (7 to 11),[62,105] partial pressures of hydrogen (up to 2 bar_{abs}) and oxygen (up to 0.5 bar_{abs}) and electrical currents (up to 5 A cm^{-2}). These conditions impact membrane and electrode degradation.[106,107] The higher humidity and/or temperature, the faster is the degradation of electrodes and membrane.[108,109,110] High electrode potentials, temperatures and humidities enhance carbon support oxidation leading to losses in PEMFC performance.[111,112,113,114] As PEMFC degradation is affected not only by operating parameters but also by materials and construction methods, we refer to the literature for more detailed descriptions.[115,116]

Controlling the operating parameters of a fuel cell during operation can significantly enhance its lifetime. The most critical operational faults are described in detail in chapter 2.2.

2.1.2 Membrane Electrode Assembly

A gas diffusion layer (GDL) is adjacent to the anode and cathode of the CCM, respectively, as illustrated in **Figure 2.2**. We name the combination of CCM and GDLs as MEA. The GDL connects the bipolar plates (BPP) with the catalyst layer, whereby the GDL significantly influences the state of the anode and cathode.

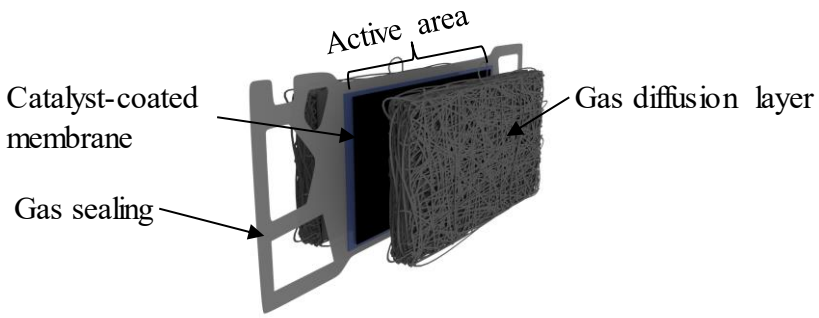

Figure 2.2. Automotive size membrane electrode assembly with enclosing gas diffusion layers.

[e] λ_{mem} = moles H_2O per moles of the functional SO_3^- groups.

The GDLs enable the transport of reactant gases to the electrodes and remove the produced water from them.[115,117,118] Additionally, they link the catalyst layer and the BPPs electrically (see following chapter 2.1.3) by ensuring a homogeneous pressure distribution as they are compressible. A GDL consists of a macro-porous layer heading towards the BPPs and a micro-porous layer that is in contact with the catalyst layer. The polymer in the membrane and catalyst layers needs to be hydrated during operation, whereas the electrodes must not contain water droplets. The basic function of the GDL is, therefore, to remove liquid water from the electrode layers while maintaining the humidity inside the polymer under dry and wet operating conditions.[115] Wet operating conditions occur if, for example, the inflowing gases are strongly humidified or if the cell current is high and therefore, much water is produced in the cathode catalyst layer. The GDL is also responsible for a homogeneous gas distribution within the catalyst layers.[115]

The macro-porous structure of a GDL has a thickness of ~300 µm[119] and consists of carbon fibers for electrical conductivity[115] and a polymer (i.e., PTFE) to adjust its hydrophobicity towards water removal.[120] The microporous structure is made of carbon powder and a polymer with a typical thickness of ~50 µm.

Several things can malfunction inside the GDL during fuel cell operation. Water droplets (i.e. during freeze/thaw cycles) induce a loss of hydrophobicity, which in turn leads to increased water contents inside the GDL.[121,122,123,124] Flooded locations impede the diffusion of hydrogen and oxygen, and therefore, the gas flows might not fulfill Faraday's law of electrolysis as described in chapter 2.1.1. Furthermore, several mechanisms cause thinning of the GDL, which in turn increases the contact resistances between the fuel cell layers.[115] Contrary, if the GDL compression is too high, the gas permeability collapses,[125] which lowers the fuel cell performance and efficiency.

The processes within the GDL, especially reactant gas diffusion and electrical resistance, influence the impedance response of the fuel cell. Thus, physically meaningful impedance-based real-time monitoring must take these processes into account, which will be described in chapter 2.4.4.

2.1.3 Fuel Cell – Local Processes

BPPs with imprinted flow fields enclose the MEA as illustrated in **Figure 2.3**. In this thesis, we label the combination of MEA and BPPs as a fuel cell. The flow fields are the main geometric parameter to obtain a homogeneous electrochemical profile along the electrodes of an MEA, as they control the distribution of reactant gases, humidification and temperature.[122] Water droplet formation inside the GDL or the catalyst layers can originate from poor flow field designs and surface structures, which need to be considered when building a physical impedance model.

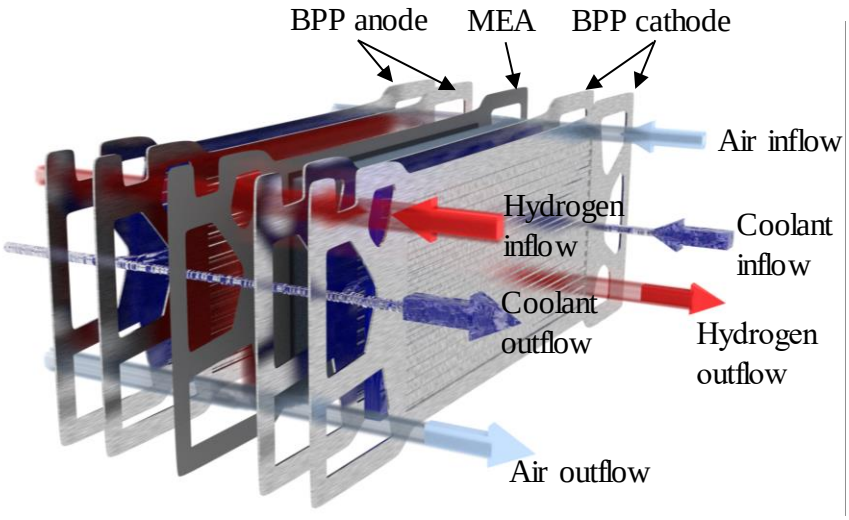

Figure 2.3. Fuel cell consisting of two bipolar plates (BPPs) and a membrane electrode assembly (MEA), including the flow regimes for air, hydrogen and coolant. Geometry is taken from ref. [126].

In automotive applications, the BPPs typically consist of two metallic monopolar plates made of stainless steel or titanium,[93] on which the cathode and anodic flow field structure is imprinted. Hydrogen streams through the anode manifold (see hydrogen inflow in **Figure 2.3**), follows the channels of the anode BPP and exits the fuel cell at the hydrogen outflow. As shown in **Figure 2.3**, the airflows in the opposite direction to the hydrogen flow, which is called the counter-flow regime.[243] FCEVs have power outputs of more than 100 kW, which makes liquid cooling of the individual cells necessary.[127] The liquid flows between the two monopolar plates of the anode and cathode.[128,129] The flow configuration

in **Figure 2.3** (hydrogen-air counter-flow, air-coolant co-flow) has the best performance at any current density in terms of membrane hydration.[127,130,131]

The kinetics of the ORR depend on the oxygen partial pressure. Consequently, the gradient of partial pressure along the flow field determines the homogeneity of the electrochemical profile. As the flow field controls air distribution across the MEA, the BPP design has a great influence on the local processes within the catalyst layer. The partial pressure of the reactants decreases from inflow to outflow if an electric current is drawn. If the flows are calculated according to Faraday's law of electrolysis $\dot{V}_{Faraday}$ (see chapter 2.1.1), the partial pressures at the outlet are zero. The ratio of supplied reactant volume $\dot{V}_{supply}$ to $\dot{V}_{Faraday}$ is called stoichiometry λ. The higher the stoichiometries of oxygen and hydrogen, the lower the reactants' partial pressure gradient. An inhomogeneous distribution of the ORR overpotentials causes an uneven distribution of the current density along the flow field. The local current density impacts the local temperature[131,132,133] and thereby (1) the reaction kinetics, (2) the degradation of all layers, (3) the water drag and back diffusion across the membrane and (4) the polymer proton conductivity.[87,134] Another challenge for the BPP design is the condensation of water in the flow field channels at low temperatures,[134,135] leading to a rapid performance decay and stack failure.[62,122]

Summing up, the main challenge related to BPPs and the imprinted flow fields is to minimize local inhomogeneities inside the electrodes and membrane in terms of hydration, temperature and gas partial pressures. Typical malfunctions due to local effects are described in chapter 2.2.

2.1.4 Fuel Cell Stack – Global Processes

An electrical motor inside an FCEV needs to deliver the power of ~100 kW at ~400 V. As a single fuel cell delivers ~0.5 kW at ~0.6 V (250 cm² active area), more than 200 cells are typically stacked to build a fuel cell system (**Figure 2.4**). The electrical current inside the stack passes from the current collector of the cathode towards the anode connecting the fuel cells in series. The electric current flowing through each cell in the stack i_{cell} is the same. The load in **Figure 2.4** utilizes the power. The reactant gas and coolant flows enter the stack through manifolds that connect all fuel cells in parallel. Due to the parallel flow connections, the amount of fluid (hydrogen, air, coolant) that reaches each cell varies. As the electrical current through each cell is equal, but the flow of reactant gases can be

different, the hydrogen and oxygen stoichiometries vary along the stack. The operation of individual cells below a stoichiometry of 1 is a typical malfunction caused at the stack level, which we refer to in this work as global starvation effects.

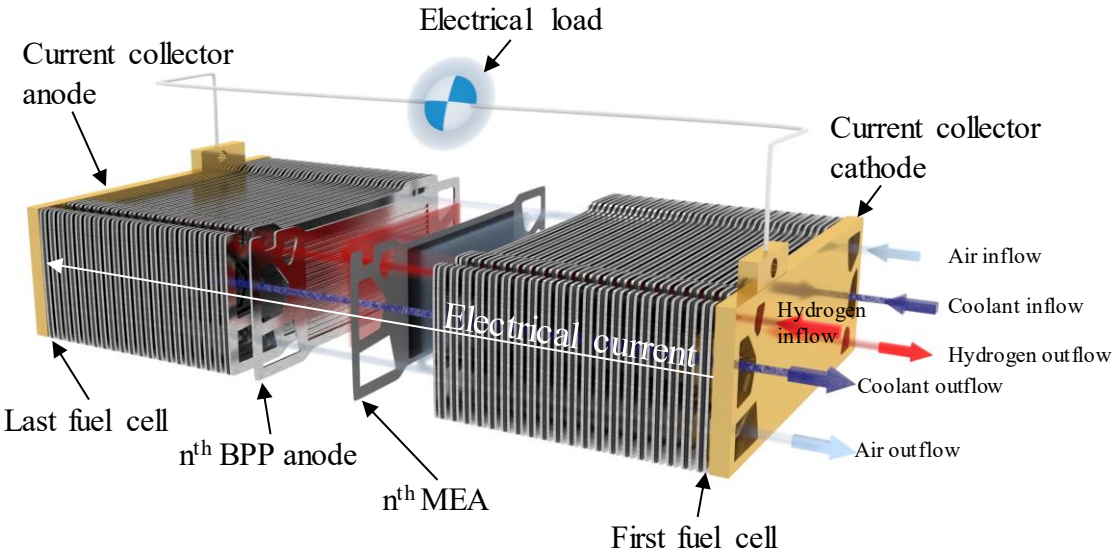

Figure 2.4. Fuel cell stack including fluid and electrical flow regimes. The abbreviations are membrane electrode assembly (MEA) and bipolar plate (BPP).

An inhomogeneous distribution of reactants can also lead to water droplet formation inside the MEA or cause pinholes in the membrane, which allow direct contact of the reactant gases and induce high local temperatures. Pinholes cascade to neighboring cells as the BPPs link those thermally and electrically.[136] The coolant distribution impacts the temperature distribution inside the stack that can be in the range of 10 °C as determined by Noorkami *et al.*[137] For this work, it is important to notice that temperature, humidification and reactant gas stoichiometries vary from cell to cell in a stack. It is not feasible to use conventional mass flow sensors to measure such cell to cell variations, making EIS a promising solution.

2.1.5 Summary

The electrochemical reactions inside the catalyst layer fail if the supply with reactants, electrons, or protons are inhibited. This inhibition can occur at all levels of the setup, in the

catalyst layer, GDL, flow fields and manifolds of a fuel cell stack. A methodology to detect related problems is EIS.

2.2 Typical Malfunctions During Fuel Cell Operation

This chapter describes the most frequent and harmful operational malfunctions that are relevant for FCEVs. Reactant starvations evolve, i.e., when water droplets form inside the MEA or BPPs, leading to severe degradation of all fuel cell components (see chapters 2.2.1 and 2.2.2).[138] The membrane develops cracks and crazes when exposed to dry conditions, which in turn leads to gas crossover, short circuits and heat development (see chapter 2.2.3).[138]

2.2.1 Local and Global Hydrogen Starvation

The hydrogen starvation phenomenon also called fuel starvation, is divided into the local and global/overall/gross starvation mechanisms. During reactant gas starvation, the potentials between electronic and ionic phase shift in anode and cathode.

In normal PEMFC operation, the ORR takes place at the cathode at an electrode potential (relative to the membrane ionic potential) of ~0.6 V, and the HOR occurs at the anode at ~0.0 V.[139] This is illustrated in **Figure 2.5 A** close to the hydrogen inlet $H_{2,inlet}$. At this location, there is a sufficient amount of hydrogen at the anode (red shaded area in **Figure 2.5**) and oxygen at the cathode (light blue shaded area) to supply the required electrons and protons from the electrochemical reactions for the ORR.

The global hydrogen starvation occurs when the supplied hydrogen amount $\dot{n}_{H2}$ is lower than the hydrogen flow $\dot{n}_{H2,Faraday}$ necessary to draw a certain cell current i_{cell} according to Faraday's law of electrolysis.[140] In that case, there is a lack of protons and electrons from the HOR.[139] Thus, the anode potential climbs to more positive values until the oxidation of the carbon support (COR) and the oxygen evolution reaction (OER) occur (see **Figure 2.5 A** close to $H_{2,outlet}$).[106,141,142] The anode potential rises to values between 1.5 V and 2.5 V, which is more positive than the cathode potential, causing a cell voltage reversal.[106,141,143] A global hydrogen starvation leads to severe degradation of the anode catalyst layer and is identified by cell voltages below -0.2 V. The heat generated during a

cell voltage reversal causes pinhole formation and electrical shorts across the polymer membrane.[144] At the hydrogen inlet, the currents become very large and can exceed the ORR's limiting current density, inducing the hydrogen evolution reaction (HER) in the cathode catalyst layer.[145] In addition to anode degradation, the cathode catalyst layer's carbon support and platinum particles degrade during global fuel starvation, as reported by Taniguchi *et al.*[141,146,147] One can estimate that a PEMFC may experience global hydrogen starvation for a maximum of 10 s to 1000 s in its entire life span without being destroyed.[148]

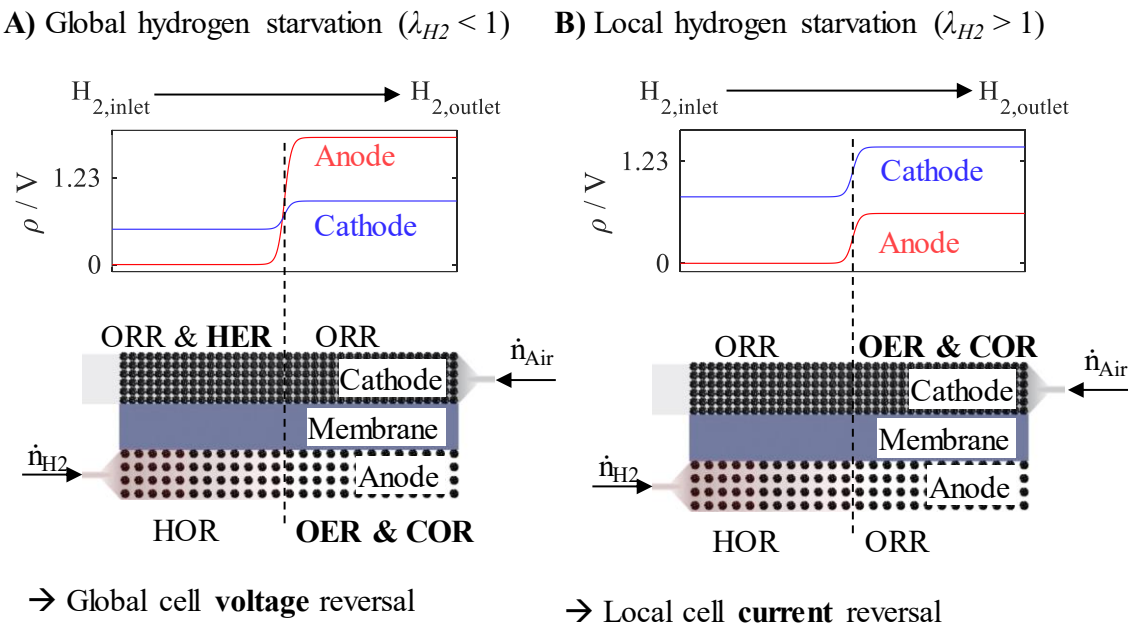

Figure 2.5. Local interfacial potentials φ for **A)** global and **B)** local hydrogen starvation. Symbols and abbreviations: Cell current (i_{cell}), hydrogen molar flow ($\dot{n}_{H2}$, red shading), Faraday's constant (F), Oxygen reduction reaction (ORR), hydrogen oxidation reaction (HOR), oxygen evolution reaction (OER), carbon oxidation reaction (COR), Hydrogen stoichiometry (λ_{H2}).

During fuel cell malfunctions, anodic and cathodic reactions take place on both electrodes. To avoid confusion, we label the electrode that is the cathode during normal fuel operation as a (geometric) cathode. If a cathodic parasitic reaction occurs at the electrode where the HOR typically takes place, we will refer to it as the (geometric) anode.

Local hydrogen/fuel starvation occurs when there are hydrogen-rich and hydrogen-free regions in the anode catalyst layer, as indicated by the red shaded area in **Figure 2.5 B** (Anode).[149] On the left in **Figure 2.5 B** ($H_{2,inlet}$), the normal fuel cell reactions take place at the anode (HOR) and the cathode (ORR) as there is sufficient hydrogen available to provide the required protons and electrons. Close to the anode outlet ($H_{2,outlet}$) there is no hydrogen available, e.g., due to water droplets that block access to this region. The BPPs electrically link the hydrogen-rich and hydrogen-starved regions, guaranteeing a similar interfacial potential difference between anode and cathode.[57,106] In **Figure 2.5 B**, the potential difference close to the anode inlet (normal fuel cell operation) is ~0.8 V (arbitrary value), while the anode potential of the HOR is ~0.0 V. At this potential, there is no anodic reaction at the hydrogen-free region to conserve the current and maintain the potential difference of the hydrogen-rich region.[150] Therefore, the anode and cathode potentials shift to more positive values, as illustrated in **Figure 2.5 B**. At higher potentials, the (geometrical) anode converts oxygen that diffuses from the cathode to the anode through the polymer membrane to form water (ORR).[150] Potentials above 1.23 V at the (geometrical) cathode enhance the COR and OER, which act as a proton donor for the ORR at the (geometrical) anode.[151] The movement of protons from cathode to anode is contrary to normal fuel cell operation and is thus typically called “reverse current effect”.[57] The ORR current at the anode is determined by the oxygen crossover rate, which in turn limits the currents of the COR and the OER at the cathode.[149] A lower oxygen crossover from cathode to anode therefore decreases the degradation of the cathode catalyst layer during local hydrogen starvation events.

2.2.2 Local and Global Oxygen Starvation

Compared to hydrogen starvation, the oxygen supply is considered less relevant with respect to degradation.[152,153] The ORR overpotential increases from air inlet towards air outlet due to the drop in oxygen partial pressure. In the case of oxygen starvation, this increase in overpotential is especially pronounced as the amount of oxygen drops to zero, causing a cathode potential drop to ~0.0 V - ~0.3 V.[154] At such low potentials the HER gets relevant, as illustrated in **Figure 2.6**. Thereby, the protons arriving at the cathode are converted to gaseous hydrogen instead of reacting with oxygen to form water.[154,155] The anode potential was found to increase slightly from ~0 V to ~0.2 V.[152] Dependent on the air stoichiometry, the cathode potential can drop below the anode potential and cause a

reversal of cell voltage (see **Figure 2.6**).[152] As the HER has a low overpotential, the voltage reversal during air starvation typically reaches *ca.* -0.1 V. The occurrence of the HER in the presence of air starvation is referred to in the literature as the "comma-shaped" or "n-shaped" polarization curve phenomenon.[154,155]

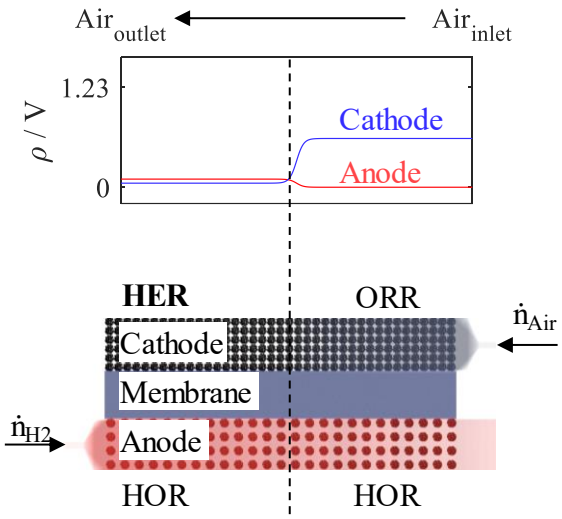

Figure 2.6. Sketch of local interfacial potentials φ during oxygen starvation. Air molar flow $\dot{n}_{Air}$ (light blue shading).[152] ORR: Oxygen reduction reaction, HOR: Hydrogen oxidation reaction, HER: Hydrogen evolution reaction.

The HER's heat generation is significantly lower compared to the ORR and therefore a temperature gradient evolves, leading to inhomogeneous degradation of the MEA in the gas flow direction.[153,155] Air starvation induces the loss of platinum at the cathode,[152] local hot spots[153] and inhomogeneous MEA degradation.[155] It also impairs the dynamic behavior of the fuel cell to load changes and therefore gets more attention as a relevant fuel cell malfunction.[156] Oxygen depletion has the positive effect of reducing platinum oxides due to the low cathode potentials, which leads to a regeneration of the catalyst surface.[155]

2.2.3 Parasitic Currents

Ideally, the polymer membrane separates anode and cathode electrically, prevents direct contact of hydrogen and oxygen, and is only conductive for protons, as illustrated in **Figure 2.1** on page 8. In real systems, the membrane can form cracks and pinholes due to contaminant particles, non-uniform stress distribution and membrane corrosion.[122,157] Chemical corrosion is mainly induced by H_2O_2 that attacks the membrane end groups,

especially at low humidification and high temperatures.[158,159] Pinholes decrease the membrane's electrical resistance and allow the crossover of reactant gases to the adjacent electrode. This crossover increases with increasing pressure differences between anode and cathode, leading to local hot spots as hydrogen and oxygen react within the catalyst layer.[160] When pinholes form close to the anode inlet, their impact on degradation is in general strongest.[161]

Parasitic currents i_{par} are currents that cannot be utilized by the external load, such as electrical shorts and hydrogen crossover across the membrane. They are typically in the range of 0% to 4% of the total cell current[96] and thus, do not severely impact the fuel cell performance.[160] As parasitic currents barely impact the fuel cell performance in operation, voltage-based monitoring is difficult. The open-circuit voltage (OCV) is a quantitative indicator of i_{par} as the electrode potential according to the Butler-Volmer equation depends on the current as $OCV \sim \ln(1/i_{par})$.[162] The OCV is impractical to monitor pinholes in FCEVs as high potentials should be avoided with respect to electrode degradation[106] and as the utilizable power output during OCV is zero. Nonetheless, pinhole formation leads to high voltage degradation rates or even a "sudden death" of fuel cell stacks and needs to be tracked in FCEVs, which will be described in chapter 2.4.[157,160]

2.3 Electrochemical Impedance Spectroscopy

The electrode layers and membrane are the most vulnerable components in a fuel cell system (see chapter 2.1), and thus the operating conditions (e.g. temperature) must be optimal at this level. It is easy to imagine that temperature measured on the (macroscale) stack level in **Figure 2.4** (page 14) will not represent the temperature e.g. inside the (microscale) electrocatalytic layers (**Figure 2.1**, page 8). An ideal operational strategy controls a fuel cell stack at optimum parameter sets concerning performance, efficiency and degradation. This is a challenging task as those often require contradicting operating conditions, as e.g. high relative humidity, *RH*, increases the performance and at the same time enhances catalyst layer degradation.[101,163]

EIS is an *operando* and non-invasive measurement technique sensitive to electrochemical processes and the corresponding operating conditions.[164] It is used to determine

temperature, gas pressures and gas flow rates during fuel cell operation.[78,86,165] The impedance behavior can be recorded from any object (e.g. fuel cell, battery, human, vegetables) and often correlates with its specific properties (e.g. humidification, age, blood sugar, taste).[166,167,168,169] The EIS response is influenced by physical properties of a fuel cell such as diffusivity, rate constant and viscosity but does not provide a direct measure of those.[170] It is incremental to have a physical model of the fuel cell to extract reliable information. Chapter 2.3.1 introduces EIS's measurement concept, while chapters 2.3.2 to 2.3.4 explain different interpretation and modeling approaches. Since the data analysis in this thesis is primarily based on equivalent electric circuits (EECs), this is described in a separate chapter (2.4).

2.3.1 Basics of Impedance Spectroscopy

To record the impedance of an electrochemical device, the latter is perturbated with a regularly repeated current or voltage, typically a sine wave when monitoring fuel cells.[171,172] For a galvanostatic EIS measurement, the electrical current is excited $j(t) = j_0 + \hat{I} \cdot sin(\omega \cdot t)$ with a certain amplitude $\hat{I}$ and (angular) frequency ω, which can be superimposed on a direct current (DC) density j_0. The corresponding voltage response $U(t) = U_0 + \hat{U} \cdot sin(\omega \cdot t + \varphi)$ is recorded where φ is the phase shift between current perturbation and voltage response, U_0 is the DC voltage response, and $\hat{U}$ is the alternating current (AC) voltage amplitude. The ratio of $U(t)$ to $I(t)$ represents the transfer function of the black box in **Figure 2.7**. A physical model is required to interpret its transmission behavior.[170]

To increase the expressiveness of the EIS analysis, the object is excited at various frequencies $f = \omega/(2\pi)$. The Nyquist representation is a common way of illustrating impedance data, which will also be used throughout this thesis (see **Figure 2.7 B**). Thereby, the impedance of the system is separated into the real part (resistance) Z_{Re} and the imaginary part (reactance) Z_{Im}, as $Z = Z_{Re} + iZ_{Im}$.[173] Thereby, i is the imaginary unit ($i^2 = -1$). A comprehensive description of Nyquist plots is given elsewhere.[174]

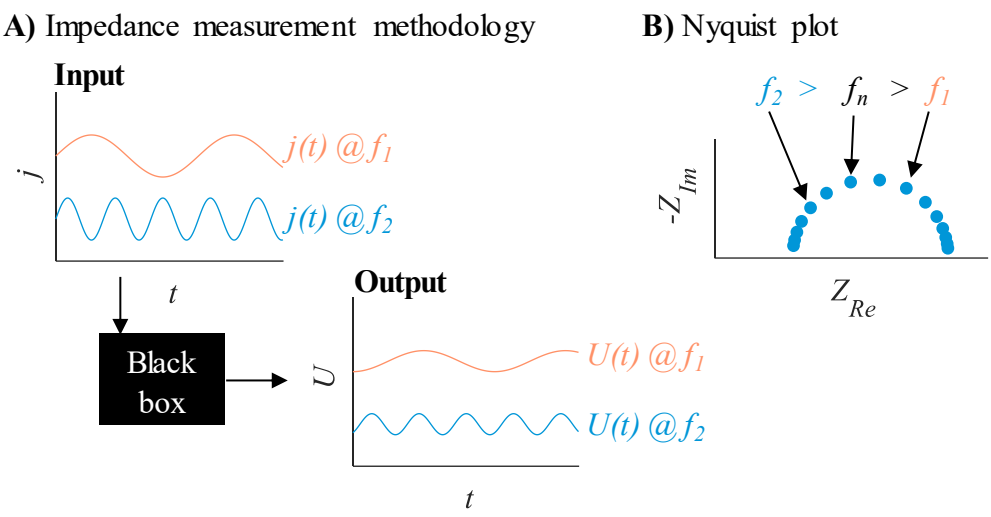

Figure 2.7. A) Principle of electrochemical impedance measurement with a sinusoidal galvanostatic excitation, *j(t)*, and voltage response, *U(t)*, at different frequencies, *f*, inspired by M. E. Orazem.[170] **B)** Nyquist representation of impedance data.

The Kramers-Kronig relations are a mathematical tool to validate the quality of the measured impedance response. In case the impedance data fulfill these relations, the following conclusions can be drawn. (1) Causality: The response is purely related to the perturbation signal; solely first order response is contained in the signal. (2) Linearity: The system was stable with time. (3) Stability: The impedance reaches finite values at hypothetical perturbation frequencies of zero and infinity.[175,176]

2.3.2 Empirical Impedance Analysis

It takes about 200 s to record one EIS between 300 mHz and 1 kHz using ten frequencies per decade. Faulty operating states, such as hydrogen starvation, can lead to the fuel cell stack's total damage within a few seconds.[141] Consequently, a resolution of one second or less is necessary for the detection of faults. Multi-sine[177] and rectangular excitations decrease the measurement time, but to date, impedances in FCEVs are recorded using sinusoidal signals.[178,179] Therefore, state-of-the-art applications evaluate the impact of operating conditions on the impedance at single frequencies.[180] For impedance-based monitoring of BEVs and FCEVs, empirical approaches using single-frequency perturbation are currently most important as they achieve to extract information within a few

seconds.[77,78,85,86,181] A pre-selection of the measurement frequency is necessary to apply empirical impedance approaches for system monitoring.[182]

To date, EIS monitoring of PEMFCs is used to monitor (1) membrane hydration,[78] (2) electrode flooding,[77,183] and (3) air supply.[85] First, membrane hydration is determined using the resistance measured at 300 Hz to 1 kHz.[77,78,180,184,185,186] Second, imaginary and real part of the impedance below 10 Hz correlate with flooding of fuel cell electrodes.[77,186,187] Third, air supply rates are determined by measurements at 0.1 Hz in addition to the cell current.[85]

A limitation of the empirical impedance evaluation approach is the lack of an underlying physical model. To minimize the measurement and evaluation effort, the data are recorded only at selected frequencies.[77,78,86] This makes physical interpretation of the signal difficult and increases the risk of cross-influences. To give an example, the impedance at low frequencies (0.1 Hz to 0.5 Hz) is either used to indicate airflow rates or flooding,[77,85] which is a consequence of the impedance being sensitive to several electrochemical processes. For real-time monitoring of fuel cell systems, unique impedance characteristics need to be determined to identify normal and critical operating states. The dehydration of a fuel cell is often measured using the real part of the impedance at ~300 Hz.[188] The high-frequency resistance (HFR) is the physically meaningful value to determine the hydration of the membrane. Depending on the operating parameters, the frequency of the HFR changes. To give an example, during flooding, the HFR is relatively constant, but its frequency shifts. Because of this, the resistance at 300 Hz rises, which falsely indicates membrane dehydration instead of electrode flooding.[189] Consequently, measuring the HFR instead of the resistance at a fixed frequency is reasonable.

Impedance measurements at a single frequency carry a high risk of misinterpretation. If applied in FCEVs, comprehensive knowledge of the fuel cell is vital. In this thesis, we will not use the single-frequency approach. Nevertheless, the findings of empirical impedance research support the determination of detectable phenomena in PEMFC operation, such as dehydration and air starvation.

2.3.3 Process Models

EECs, as developed by Randles and Dolin, were derived for planar electrodes.[190] In a PEMFC, there are several components such as BPPs and GDLs that contribute to the impedance of the cell, which cause a deviation in the impedance characteristics of fuel cells compared to e.g. single-crystal measurements.[191,192] Other artifacts in PEMFC EIS measurements are caused by (1) the highly porous structure of the electrodes, (2) adsorption processes on platinum, (3) and catalyst poisoning. Such processes were investigated using physical process models.[193] Physical-based impedance process models can predict measured EIS data and fill thereby the gap between equivalent electric circuit models for the electrochemically active layer (see chapter 2.4) and transport processes in PEMFCs.[164] In this thesis, process models will be considered to gain a deeper understanding of the EEC modeling results.

2.3.4 Model-free Impedance Analysis

Model-free impedance evaluation is the mathematical treatment of impedance data without implying an underlying physical model. The advantage of model-free analysis is that no knowledge of the system under study is required before the analysis.[164] The frequency dependence of the impedance data remains, contrary to complex non-linear least-squares (CNLS) fitting or process model procedures, where distinct fuel cell characteristics are extracted.

Differential impedance analysis (DIA) is an objective data processing methodology, as it does not assume a physical model describing the system.[194] This approach is investigated in this work for real-time monitoring of FCEVs as it (1) keeps the physical model as simple as possible, (2) requires little computational time, and (3) provides stable and fast data processing.[195] To analyze an impedance measurement using DIA, it is scanned in the frequency domain using a local operating model (LOM). This procedure will be described using **Figure 2.8**.

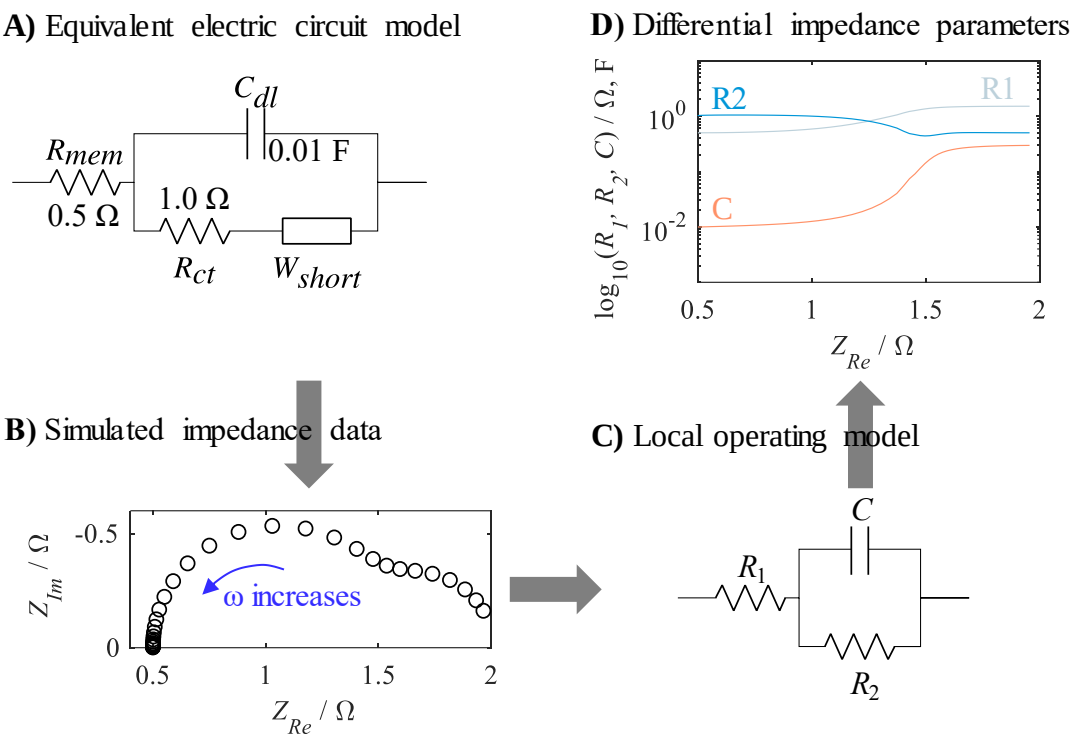

Figure 2.8. Investigation of the differential impedance procedure by **A)** defining a bounded-Randles model with R_{mem} = 0.5 Ω, C_{dl} = 0.01 F, R_{ct} = 1 Ω, $W_{s,R}$ = 0.6 Ω, $W_{s,c}$ = 0.6 s^{-1}, **B)** simulating the model, **C)** scanning the simulated spectra with a local operating model (LOM) and **D)** visualizing R_1, R_2 and C of the LOM *versus* the resistance Z_{Re} according to **Eq. 3**, **Eq. 4**, and **Eq. 5**. Note that at Z_{Re} = 0.5 Ω, $R_1 \approx R_{mem}$, $R_2 \approx R_{ct}$ and $C \approx C_{dl}$. Inspired by Vladikova *et al.*[196]

To mimic an EIS measurement, an EEC was assumed (**Figure 2.8 A**), which was simulated in the frequency range between 300 mHz and 10 kHz as shown in **Figure 2.8 B**. The simulated spectrum was scanned with a LOM shown in **Figure 2.8 C** consisting of two ohmic resistors R_1, R_2, and a capacitance, C. This LOM represents a simple first-order system which can be described mathematically by **Eq. 1** where $T = R_2C$.[194] To determine the LOM parameters (R_1, R_2, C), the derivatives of the real $\partial Z_{Re}/\partial\omega$ and imaginary $\partial Z_{Im}/\partial\omega$ components in **Eq. 1** are build, while for convenience, the derivative of the effective inductance $\partial L_{eff}/\partial\omega$ is typically used.[194]

$$Z_{LOM} = R_1 + \frac{R_2}{1+\omega^2T^2} + \mathrm{i}\frac{\omega R_2 T}{1+\omega^2T^2} \qquad \textbf{Eq. 1}$$

The frequency ω dependent time-constant $T(\omega)$ is calculated according to **Eq. 2**.

$$T(\omega) = \frac{\partial L_{eff}(\omega)}{\partial Z_{Re}(\omega)} \qquad \textbf{Eq. 2}$$

The LOM parameters are then obtained according to **Eq. 3** for R_2, **Eq. 4** for R_1, and **Eq. 5** for C.

$$R_2(\omega) = -\frac{\partial Z_{Re}(\omega)}{\partial \omega} \cdot \frac{\left(1+\omega^2 T^2\right)^2}{2\omega T^2} \qquad \textbf{Eq. 3}$$

$$R_1(\omega) = Z_{Re}(\omega) - \frac{R_2(\omega)}{1 + \omega^2 T^2} \qquad \textbf{Eq. 4}$$

$$C(\omega) = \frac{T(\omega)}{R_2(\omega)} \qquad \textbf{Eq. 5}$$

Thus, determining the derivatives of real and imaginary components of the EIS data in **Figure 2.8 B** allows the calculation of the (frequency-dependent) LOM parameters as shown in **Figure 2.8 D**. Note, that the LOM values (R_1, R_2, C) at Z_{Re} = 0.5 Ω in **Figure 2.8 D** are equal to the simulated values of R_{mem}, R_{ct}, and C_{dl}, respectively. This is important because parameters that are usually measured at low measuring frequencies and thus long measuring times can now be determined at high frequencies. To give an example, the resistance R_{ct} is 1 Ω and can be found in the Nyquist plot (**Figure 2.8 B**) at Z_{Re} = 1.5 Ω (3 Hz). R_{ct} is detected in the DIA **Figure 2.8 D** at Z_{Re} = 0.5 Ω (10 kHz).

Another model-free impedance evaluation technique was presented by Kurzweil *et al*. Thereby, the impedance is analyzed based on the real part capacitance, C_{Re}, for optimal, humid and dry operating states.[80] The corresponding Nyquist plots are illustrated in **Figure 2.9 A**, while the real part of the capacitance *versus* the cell resistance is shown in **Figure 2.9 B**. Identifying the optimal operating parameter set is more evident when the real part capacitance is used instead of the imaginary component of the impedance. The larger the capacitance and the smaller the resistance, the better the operating condition. The challenge of applying this methodology in a real-time analysis is the selection of an

appropriate measurement frequency, which can be, for example, 100 Hz, as shown in **Figure 2.9 B**.

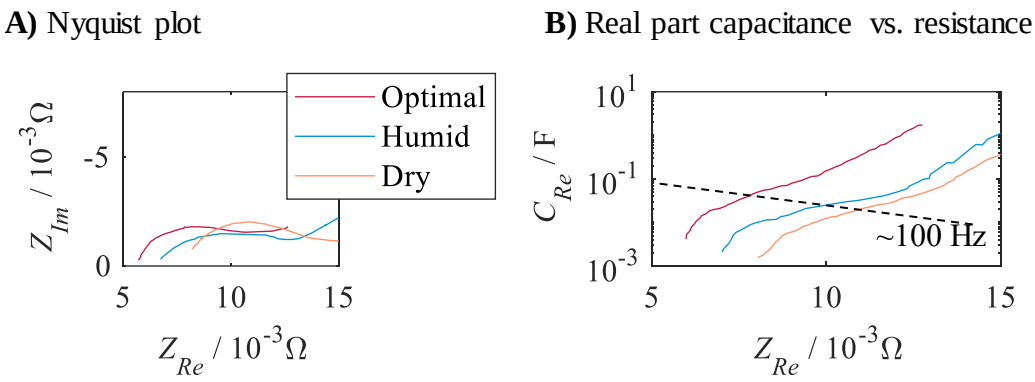

Figure 2.9. Model-free impedance evaluation for optimal (red), humid (blue) and dry (orange) operating states of an alkaline electrolyzer using **A)** the Nyquist representation and **B)** the real part of the cell capacitance as a function of its resistance. Reproduced with permission from ref. [80].

Distribution of relaxation times is another model-free and wide spread impedance post-processing technique,[164] which requires high-quality data sets. In noisy environments, such as automotive applications, the distribution of relaxation times method leads to misinterpretation, and the mathematical result becomes unstable.[197,198] For this reason, the method seems inapplicable to monitor fuel cell systems.

In this thesis, we will use a transformation of DIA for EIS data processing similar to *in vivo* monitoring of human respiration.[195] This allows a fast and stable characterization of fuel cells, which can be coupled with physical impedance models.[199]

2.4 Equivalent electric elements

EIS on laboratory cells are typically recorded in a wide frequency range and fitted to an EEC using CNLS fitting algorithms.[65,66,68,200] An EEC is not directly a physical model but an analog that mimics the system response.[201] In 1947, Randles developed the basic EEC for electrode processes where the impedance of the double layer is connected in parallel to

the Faradaic reaction.[190,202] Thereby, a capacitance, C_{dl}, is the electrical equivalent for the response of the electrochemical double layer and a resistance R_{ct} for the Faradaic reaction. A finite-length Warburg element W_{short} is placed in series, as illustrated in **Figure 2.10 A**, to account for diffusional processes (i.e. oxygen diffusion through the polymer).[203,204] The EEC was originally developed on electrochemical cells using liquid electrolytes[190] and was afterward applied to gas diffusion electrode setups with polymer membranes, as illustrated in **Figure 2.10 A**.[69,79,205]

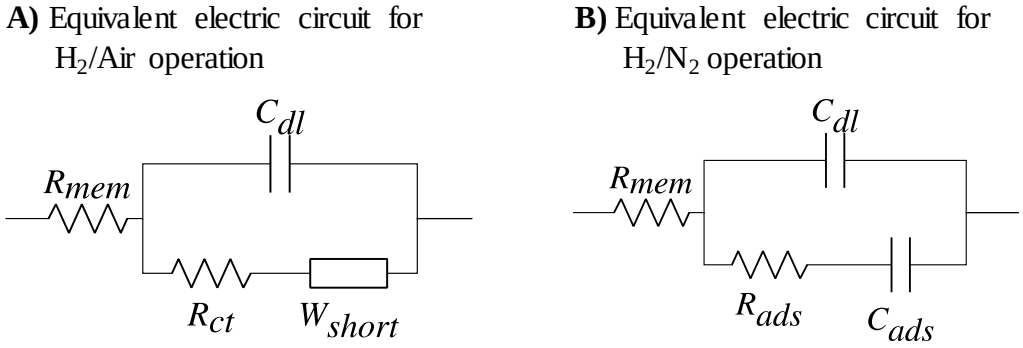

Figure 2.10. Equivalent electric circuits for **A)** fuel cell operation with hydrogen/air (bounded-Randles model) and **B)** in the absence of oxygen at the cathode.

To investigate the electrochemical characteristics in the absence of the ORR, EIS is recorded using nitrogen instead of air at the cathode. The R_{ct} and W_{short} in **Figure 2.10 A** can be neglected as there is no Faradaic reaction and no oxygen diffusion. Adsorption of $^{*}OH/O^{*}$ and H^{*} on platinum dominate the impedance response at different electrode potentials in the absence of oxygen.[206,207,208] For H_2/N_2 operation, a serial connection of resistance R_{ads} and capacitance C_{ads} are typically used as electrical equivalent to describe adsorption processes.[206,209,210] The corresponding EEC is illustrated in **Figure 2.10 B**.

This work uses EEC models in combination with DIA to obtain a physical understanding of the influence of operating parameters on the impedance of fuel cells. Reasons to not use the widely spread CNLS methodology for real-time monitoring of fuel cells are (1) measurement times in the range of minutes, (2) unstable mathematical algorithm, and (3) dependence on initial parameter sets.[204] The following chapter describes the EEC elements of **Figure 2.10**, namely the ohmic resistance (chapter 2.4.1), the charge transfer

resistance (chapter 2.4.2), the cell capacitance (chapter 2.4.3) and the diffusional impedance (chapter 2.4.4).

2.4.1 Ohmic Resistance: State Indicator for the Polymer Membrane

The ohmic resistance of PEMFCs is the currently most common parameter for FCEV impedance-monitoring as it correlates with the membrane humidification and is, therefore, an indicator for polymer hydration.[211] As many processes such as gas diffusion and ORR kinetics depend on the relative humidity,[96,212,213,214] the measurement of the ohmic resistance allows to unravel not only ohmic but also kinetic and diffusional losses.

A fuel cell consists of several layers (BPPs, GDLs, MPLs, catalyst layers, membrane), and thus, the ohmic resistance is the sum of the corresponding bulk and contact resistances.[115,125,189,215] The bulk resistance of the membrane thereby dominates the cell's total ohmic losses.[189,216] The membrane is a proton conductor, and its conductivity κ_{ion} depends mainly on the membrane water content λ_{mem} and temperature T_{cell}.[75,214,217] This is exemplarily shown for perfluorosulfonic acid type (e.g. Nafion™) membranes in **Eq. 6**.

$$\kappa_{ion}\ [\mathrm{S\ m^{-1}}] = (0.5139 \cdot \lambda_{mem} - 0.326) \cdot exp\left(1268 \cdot \left(\frac{1}{303.15} - \frac{1}{T_{cell}}\right)\right) \qquad \textbf{Eq. 6}$$

According to **Eq. 6**, the membrane proton conductivity rises linearly with water content.[75,95,217,218] As the membrane resistance is the inverse of κ_{ion}, it is more sensitive to low than high membrane water contents. To give an example, assuming a membrane thickness of 15 µm, the sensitivity of the resistance ($\partial\kappa_{ion}^{-1}/\partial\lambda_{mem}$) according to **Eq. 6** is 0.161 $\Omega\ cm^2\ \lambda_{mem}^{-1}$ for $\lambda_{mem} = 2.5$, while it is only 0.018 $\Omega\ cm^2\ \lambda_{mem}^{-1}$ for $\lambda_{mem} = 5.0$. The membrane resistance indicates dehydration, while the detection of wet operational states requires higher measuring equipment accuracy. Therefore, other procedures observe the standard deviation of the membrane resistance over time to identify the flooding of the electrodes.[183] This procedure relies on the assumption that the water droplet formation and its removal is a stochastic process during fuel cell operation.

The membrane water content depends on current density and the humidification of the reactant gases.[218] The HOR releases protons that move from anode to cathode. These protons drag water molecules from anode to cathode, which is typically referred to as

electroosmotic drag.[219] Water builds up at the cathode due to the ORR, which causes a concentration gradient across the membrane from cathode to anode. The correlated movement of water along this gradient is called back diffusion.[219] At high current densities, the electroosmotic drag outweighs the back diffusion causing dehydration of the membrane and catalyst layer of the anode.[219] A comprehensive introduction to water transport mechanisms in PEMFCs is given elsewhere.[218]

As the measurement of a full EIS and the CNLS fitting procedure are time intense and computationally intensive, the ohmic behavior of a fuel cell stack is typically evaluated by measuring the impedance at a single frequency (300 Hz, 1 kHz).[77,78] In the scope of this thesis, a method was developed to determine the ohmic resistance of a fuel cell that is (fairly) independent of the measurement frequency and evaluates the membrane losses during critical operational conditions.

2.4.2 Charge Transfer Resistance: From Electrodes to Fuel Cells

The charge transfer resistance in PEMFCs is often used to describe the performance of the cathode catalyst layer as it depends on oxygen supply, temperature and reactant gas humidification.[65,84,220] The detection of pinholes inside the membrane using the charge transfer resistance of the PEMFC in combination with the pressure difference between anode and cathode was recently published.[221] Most authors label the semicircle in the Nyquist plane in the range of ~5 to ~500 Hz as cathode charge transfer resistance. This is important to mention as the concept of R_{ct} was transferred from rotating disc electrode to PEMFC setups, whereas in PEMFCs, not only kinetic processes take place at such frequencies. R_{ct} was found to increase when (1) air stoichiometry decreases,[84,222,223] (2) temperature decreases,[65,220,222,224,225] and (3) relative humidity decreases.[214]

The cathode charge transfer resistance can be defined as the voltage loss correlated with the sluggish kinetics of the ORR in PEMFCs. This process is described by the Butler-Volmer equation and can be approximated using the Tafel assumption due to the low exchange current density of the ORR.[91] The activation loss of the cathode η_{ct} is a function of the universal gas constant, R, temperature, T_{cell}, transfer coefficient, α_c, Faraday constant, F, cell current density, j_{cell}, and exchange current density, $j_{0,ORR}$, as shown in **Eq. 7**.[91]

$$\eta_{ct} = \frac{R \cdot T_{cell}}{\alpha_c \cdot F} \cdot \ln\left(\frac{j_{cell}}{j_{0,ORR}}\right) \qquad \textbf{Eq. 7}$$

The exchange current density, $j_{0,ORR}$, increases with the partial pressure of oxygen and temperature, which is often used to explain the behavior of R_{ct}.[91] When performing an EIS measurement, the cell current, j_{cell}, is perturbated, and the voltage response ∂U is recorded, where the resulting impedance is $Z = \partial U/\partial j_{cell}$. Consequently, an EIS measurement does not quantify the overpotential η_{ct} in **Eq. 7** but its current dependent derivative as written in **Eq. 8**,

$$R_{ct} = \frac{\partial}{\partial j_{cell}}\left(\frac{2.303 \cdot R \cdot T_{cell}}{\alpha_c \cdot F} \cdot \log\left(\frac{j_{cell}}{j_{0,ORR}}\right)\right) = \frac{b}{j_{cell}} \qquad \textbf{Eq. 8}$$

with $b = 2.303RT_{cell}/(\alpha_c F)$. According to **Eq. 8**, the cathodic charge transfer resistance, R_{ct}, does not depend on the exchange current density of the ORR $j_{0,ORR}$, which implies that the dependences on oxygen partial pressure and temperature as experimentally observed for PEMFCs, do not originate from $j_{0,ORR}$.[73] There are two theories to describe the behavior of R_{ct}. First, the cathodic transfer coefficient α_c is a function of the operational conditions[226,227] such as temperature T_{cell} and relative humidity RH as $\alpha_c = (0.001552 \cdot RH + 0.000139) \cdot T_{cell}$.[214,228] The decreased ORR kinetics at low RH[96,229,230] occur due to surface restructuring of the ionomer as the hydrophobic ionomer components get in contact with platinum[231] and due to the decreased proton activity coefficient.[229] The impact of RH on ORR kinetics is especially pronounced between an RH of 0% and 60%.[96] The effect of electrode potential and temperature on R_{ct} is further investigated elsewhere.[232] The impact of air stoichiometry on R_{ct} cannot be explained when assuming that the loop between ~5 Hz and ~500 Hz is purely kinetic (**Eq. 8**), which needs to be considered when using the terminology charge transfer resistance in PEMFCs. Second, diffusion of oxygen within the cathode catalyst layer impacts the resistance of the catalyst layer in addition to the kinetic processes.[233] This phenomenon is described by a process model of Kulikovsky *et al.* for low current densities (~0.2 A cm^{-2}) , which nicely illustrates the overlap of diffusional and kinetic processes within the charge transfer resistance depending on the oxygen diffusion coefficient.[233]

Assuming the Warburg impedance in **Figure 2.10 A** (page 27) to be negligible (i.e. at low current densities), one obtains the total cell resistance as the sum of the membrane and charge transfer resistances. This total resistance is represented at low frequencies when the imaginary part of the impedance becomes zero. The fuel cell resistance measured by EIS is typically larger than the slope in DC polarization curves.[234] EIS measurements below 10 mHz show the presence of an inductive loop that seemingly approaches the fuel cell resistance from these polarization measurements.[234] The origin of this inductive loop remains unclear to date.[191] Possible causes are slow adsorption processes on the cathode catalyst and platinum dissolution.[235,236] For the interpretation of the charge transfer resistance, the occurrence of inductive loops at low frequencies is important as they seemingly increase R_{ct}.[191]

Within this thesis, a measurement methodology is developed to determine R_{ct} at high frequencies during FCEV operation in the dependence of normal and critical operational states. To build robust impedance-based control strategies the above-mentioned mechanisms must be considered.

2.4.3 Cell Capacitance: The Underrated State Indicator

To date, most studies focus on monitoring the resistive response of PEMFCs as this contains information on membrane hydration,[211] Tafel characteristics,[73] and adsorption processes.[205] The capacitive response during system malfunctions is often neglected.[84,85,222] However, the capacitance of a PEMFC contains information on electrode degradation and its state of operation.[80] A low capacitance combined with large resistances was an indicator for poor operating states (see **Figure 2.9** on page 26).[80] Additionally, it is closely related to the electrochemically active surface of a PEMFC.[233,237]

By definition, an electrical capacitance is the energy-storing capability of a capacitor, which are in the case of fuel cells the electrochemical double and catalyst layers.[174] The cell capacitance, C_{cell}, consists of double layer, C_{dl}, and adsorption, C_{ads}, capacitances as indicated in **Figure 2.11**. First, C_{dl} is the charge stored across the electrode-electrolyte interface due to charge separation of the ionic and electronic phase, which is independent on electrode potential. Second, C_{ads} is the charge stored due to the reversible adsorption and desorption of $H^*/^*OH/O^*$ species on the catalyst surface. Hydrogen underpotential

deposition (HUPD) occurs at electrode potentials between ~0 V and ~0.4 V (vs. reversible hydrogen electrode), while $^{*}OH/O^{*}$ adsorption takes place between ~0.7 V and ~1.2 V.[206,207,208,238] The electrode potential influences adsorption processes and, therefore, the associated capacitance, shown by the example of the HUPD in **Figure 2.11**. It is important to mention, that EIS does not measure the overall capacitance but the differential capacitance of the specimen.

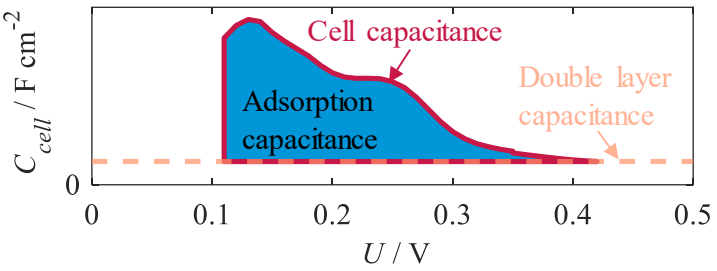

Figure 2.11. Differential cell capacitance, C_{cell}, of a fuel cell in dependence on cell voltage, U, indicating the contributions of double layer and adsorption processes. Reproduced with permission from Lochner *et al*.[126]

In this thesis, the cell capacitance during normal and critical operational states was analyzed (see chapter 4.3). As the electrode potentials shift severely during fuel cell malfunctions, as described in chapter 2.2, the potential dependence of the adsorption processes will be of special interest. Please be aware that we defined a fuel cell as the combination of MEA and BPPs as described in chapter 2.1.3. The cell capacitance, therefore, might also incorporate effects originating from the GDL or BPPs.

2.4.4 Diffusional Impedance

The diffusion of oxygen through the GDL and inside the catalyst layer causes a certain voltage loss and therefore impacts the impedance of the fuel cell.[192,239] Additionally, the diffusion through the Nafion™ film covering the Pt/C agglomerates is a major performance loss.[76] The oxygen mass transport related overpotentials decrease when increasing the humidification.[212] As diffusion has lower time constants than kinetic processes, it is represented by the low-frequency arc in the EIS. To describe the oxygen diffusion through a polymer film covering a platinum particle, we can use the finite-length Warburg

impedance, Z_W, in the EEC as illustrated in **Figure 2.10 A** (page 27) and mathematically formulated in **Eq. 9**.[76,192]

$$Z_W = \frac{j_{0,ORR} l_t \tanh\left(\sqrt{\frac{i\omega l_b^2}{D_b}}\right)}{4Fc_{ref}\sqrt{\mathrm{i}\omega D_b}} \qquad \textbf{Eq. 9}$$

In **Eq. 9**, the symbols are the exchange current density, $j_{0,ORR}$, catalyst layer thickness, l_t, GDL thickness, l_b, oxygen diffusion coefficient in GDL, D_b, and oxygen concentration in the flow field channel, c_{ref}. The relation of the Warburg coefficient and the charge transfer resistance is an indicator for the apparent reaction rate coefficient, which can be exactly calculated when the diffusion constant is known.[173,205,226]

Oxygen diffusion through the GDL impacts impedance,[213] which is especially relevant for electrochemical systems using porous electrodes due to increased double layer capacitances, C_{dl}.[192] The diffusion through the GDL can still be described by a Warburg-like impedance, but it needs to include effects of the double layer as written in **Eq. 10**.[192]

$$Z_{GDL} = \frac{Z_W}{1 + \frac{\mathrm{i}\omega C_{dl} l_t b}{j}} \qquad \textbf{Eq. 10}$$

with cell current density, j, double layer capacitance, C_{dl}, and Tafel slope, b. The importance of oxygen diffusion within the channels of the BPPs was also emphasized by Schneider *et al*.[240] Thereby, the air stoichiometry λ_{air} has a major impact on the diffusional impedance in the channel R_{ch} as formulated in **Eq. 11**.[191]

$$R_{ch} = -\frac{b}{(\lambda_{air} - 1)\ln\left(1 - \frac{1}{\lambda_{air}}\right)\cdot j} - \frac{b}{j} \qquad \textbf{Eq. 11}$$

The diffusional impedance plays a secondary role within this thesis as it is dominant at low frequencies that require increased measurement times, which is not convenient for real-time monitoring methods. Nonetheless, for data evaluation, the mechanisms described above are still vital and can also interfere with the charge transfer resistance.

3 Experimental Setup and Parameters

This chapter outlines the experimental methods and operating conditions to analyze the impedance of PEMFCs and to evaluate their behavior in normal and critical operations. Local effects due to inhomogeneous electrochemical profiles were analyzed on automotive size PEMFCs using current density distribution (CDD) measurements. In addition, we describe how adsorption and double-layer capacitances were extracted from voltammetric measurements.

3.1 Experimental Setup

The experiments in this thesis were performed on test rigs using lab and automotive size fuel cells. The design and the materials of the MEA are described in chapter 3.1.1, and the associated cell setups in chapter 3.1.2. The configuration of the test benches is explained in chapter 3.1.3.

3.1.1 Membrane Electrode Assembly

Various MEAs were characterized in this work, consisting of the gasket, CCM and a GDL. **Figure 3.1** shows the structure of an automotive size MEA. The gasket fixes the CCM and serves as a seal between the anode, cathode, and cooling compartments. The CCMs were provided by Johnson Matthey Fuel Cells and consisted of a reinforced polymer membrane with a thickness of 15 µm. The catalyst was based on carbon-supported platinum at the anode and cathode.

The GDLs were provided by SGL Carbon SE and consisted of a macro-porous and a microporous layer. The macro-porous layer was based on a carbon-fiber structure, which was coated with ~5 wt.% PTFE. The microporous layer was carbon-based (no fibers) mixed

with various PTFE contents (> 10 wt.% PTFE). Different combinations of GDLs were used at the anode and cathode to optimize the water balance of the PEMFC. The combinations are listed in **Table 3.1**. The GDL types had various thicknesses, with 29 BC being 235 µm and 22 BB being 220 µm thick. Contrary to the procedures typically described in the literature, the GDLs were not hot-pressed to the CCM during MEA fabrication.[241,242]

Many characteristic quantities of a PEMFC are related to its active area, which is defined in this work as the geometric area of the cathode catalyst layer, as shown in **Figure 3.1**. The laboratory cells had an active area of 43.56 cm^2. The cells for vehicle operation had areas greater than 250 cm^2. The combinations of MEAs and GDLs as manufactured in the scope of this work are listed in **Table 3.1**. The labels on the very left in **Table 3.1** will be used throughout this thesis to identify the type of MEA.

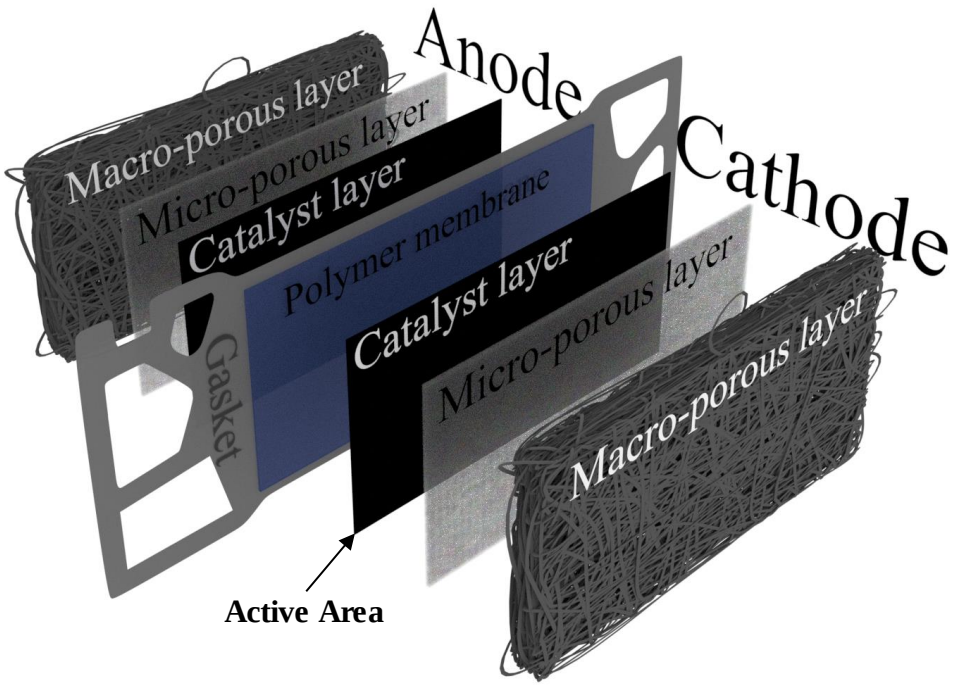

Figure 3.1. The membrane electrode assembly of an automotive size cell.

Table 3.1. Membrane electrode assembly (MEA) configurations assigned to identifiers (MEA ID) as used in chapter 4. The gas diffusion layer (GDL) nomenclature corresponds to the name under which they were sold by SGL Carbon SE.

MEA ID	Active Area [cm²]	GDL Cathode	GDL Anode
MEA #1	43.56	29 BC	29 BC
MEA #2	43.56	22 BB	22 BB
MEA #3	263.0	29 BC	29 BC
MEA #4	285.0	22 BB	29 BC
MEA #5	287.8	22 BB	29 BC

3.1.2 Cell Setup

For each MEA type with a specific active area, there was an associated cell setup, provided by Tandem Technologies Ltd. The cells were consistently operated in counter-flow regime (for a detailed description, see [243]).

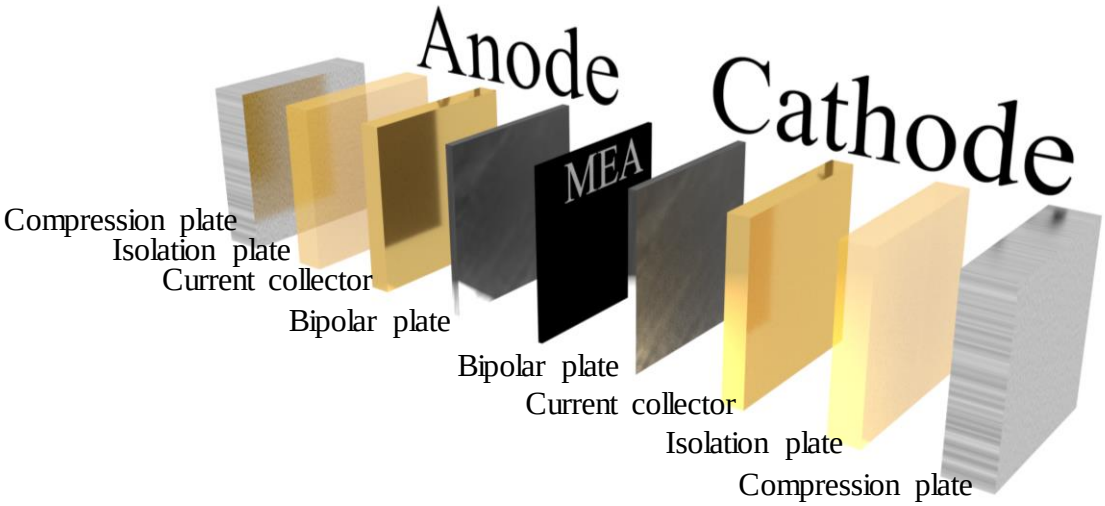

Figure 3.2. Setup of the laboratory fuel cell, including graphitic bipolar plates. Abbreviation: Membrane electrode assembly (MEA).

A sketch of the lab size cell is shown in **Figure 3.2**. The GDLs at anode and cathode formed the outermost layer of the MEA (see section 3.1.1), which was electrically contacted by the graphitic BPPs. The BPPs had a thickness of ~5 mm to reduce the in-plane resistance and ensure a homogeneous potential distribution within the MEA. Holes were drilled in the side of the BPPs to measure the cell voltage. The current collectors linked the BPPs to the electrical load using copper wires. To reduce the contact resistance, the copper-based current collectors were coated with gold. The cell was sandwiched between two compression plates that ensured a specified pressure on the MEA. The clamping pressure was applied according to the producer specifications on GDL compression. Isolation plates were inserted between the compression plates and current collectors to electrically insulate the latter. A 14-channel serpentine flow field with optimized channel depths was milled into the BPPs, which was used for reactant supply and product removal. The sealing of the 43.56 cm^2 cell was ensured using a PTFE film. This type of setup (SU) will be labeled as SU #i according to **Table 3.2**.

Table 3.2. Assignment of identification numbers (IDs) to different cell setups. Abbreviations: Bipolar plate (BPP), current scan device (CSD), the membrane electrode assembly (MEA).

Setup ID	BPP material	Flow field channels	CSD
SU #i	Graphite	Serpentine	No
SU #ii	Stainless Steel	Straight	Yes
SU #iii	Stainless Steel	Straight	No

The setup for the automotive fuel cells is illustrated in **Figure 3.3** and contained metallic BPPs, provided by DANA (Reinz-Dichtungs GmbH). The plates were made from stainless steel, including a carbon coating on top of the land areas to decrease the contact resistance between GDL and BPP and to improve the corrosion stability.[244] The BPPs consisted of two monopolar plates that were welded together. The flow field for the anode or cathode was stamped into each of the monopolar plates. To regulate the temperature of the cell, the space between the two plates was flooded with de-ionized water. The water temperature was controlled by the test rig, as will be described later in chapter 3.1.3. If the CDD was

measured during fuel cell operation, a current scan device (CSD) was placed between the BPP and the current collector of the cathode as indicated as a green layer in **Figure 3.3**. The CDD measurement is described in chapter 3.2.3.

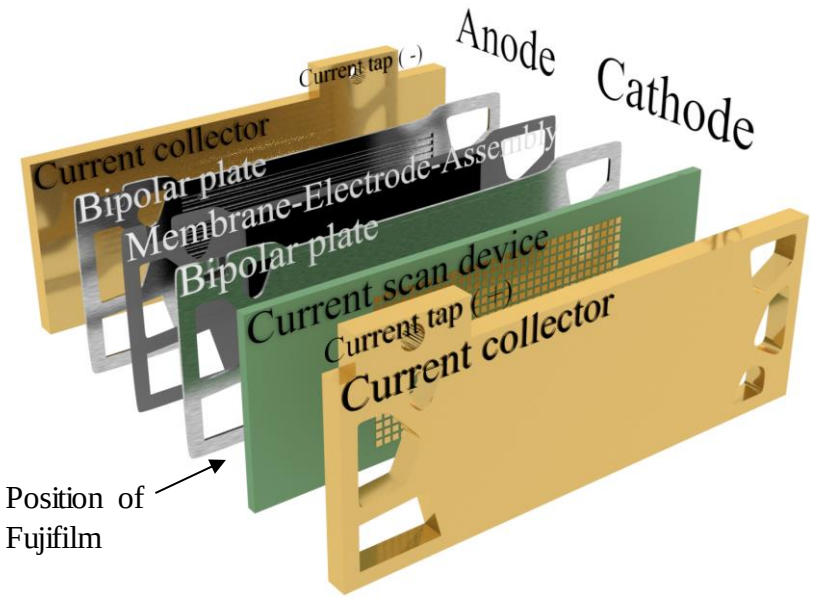

Figure 3.3. Cell setup of the automotive size fuel cell, including a current scan device for current density distribution measurements.

Figure 3.4 A shows the cathode facing side of a BPP. A straight gas flow channel configuration was realized at anode and cathode, whereby the direction of the airflow is indicated in **Figure 3.4 A**. The air enters the gas distribution zone from the air manifold. The gas distribution zones (see **Figure 3.4 A**) at the air inflow and outflow are designed to gain a homogeneous gas distribution among the flow channels within the cell's active area. Beaded gaskets were used for gas sealing as indicated with the blue line in **Figure 3.4 A**. In contrast to the laboratory cell, where the MEA compression is set by a defined path, a force is specified to compress the automotive size cell. To guarantee a homogeneous contact between the layers of the automotive size fuel cell setup in **Figure 3.3**, pressure distribution maps were recorded using a prescale film provided by Fujifilm (type LLLW).[245] This film was placed between the BPP of the cathode and the CSD (**Figure 3.3**). The test setup, including Fujifilm, was compressed and relaxed to analyze the pressure distribution. An example of the resulting measurement is given in **Figure 3.4 B**.

The solid red lines surrounding the image indicate that the highest contact pressures were at the gas sealing of the active area and manifolds. **Figure 3.4 B** shows that the pressure distribution within the active area was homogeneous at ~0.5 MPa. The measurements in this thesis were performed on three different cell assemblies, which differed in the active area, BPP material, and CSD, as indicated in **Table 3.2**.

A) Bipolar plate functional areas

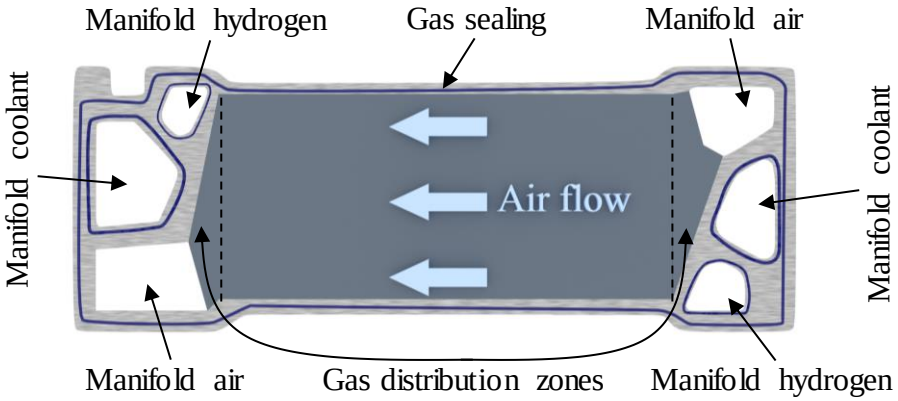

B) Contact pressure distribution

Figure 3.4. A) Functional areas of the bipolar plate for automotive fuel cells. **B**) Contact pressure distribution measured between the current scan device and the bipolar plate of the cathode according to **Figure 3.3**.

3.1.3 Test Rig Configuration

The cell setup as described in section 3.1.2 is placed into a test rig to control the operational parameters such as electrical current, gas supply, cell temperature, gas pressures, etc. The test rig was provided by Horiba FuelCon GmbH and is illustrated in **Figure 3.5**. In this illustration, an automotive size fuel cell is installed as an example, although the setup for the laboratory cells was identical. The operational functions are divided into four functional

groups, namely gas supply, power sink, coolant supply, and electrical characterization (potentiostat).

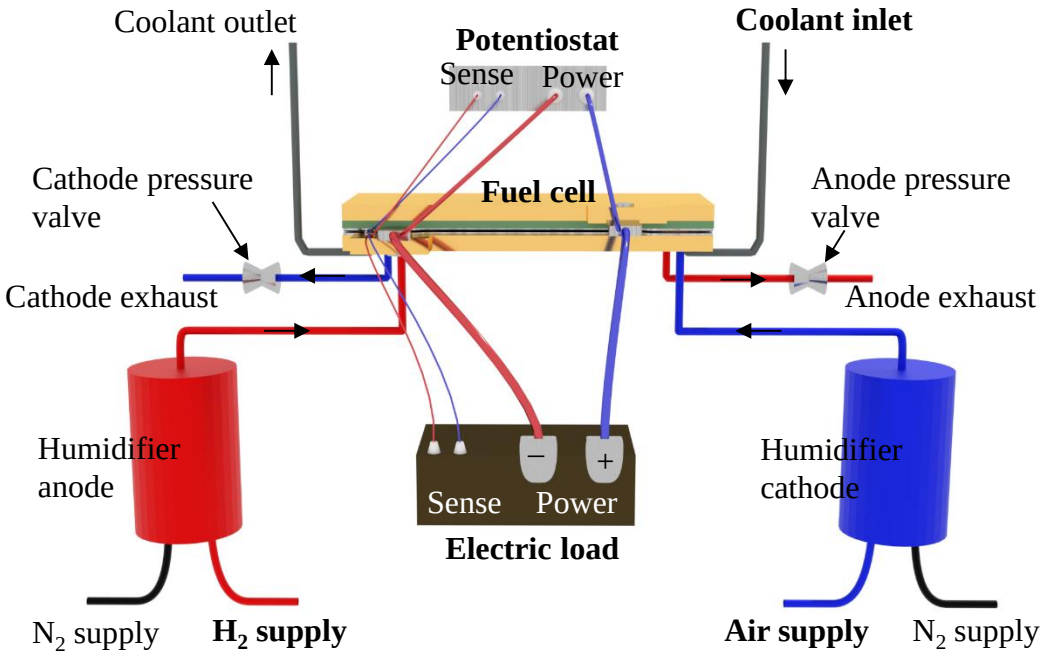

Figure 3.5. Sketch of the test rig setup for electrochemical fuel cell testing. For clarity, anode components (humidifier, gas tubes, power, and sense cables) are colored red, while cathode components are blue.

The anode was supplied with hydrogen (purity 99.999%) or nitrogen, or a mixture of both gases provided by Linde Gas. Filtered air and nitrogen could be fed to the cathode. To control the water content at the anode and cathode inlet, the gases were passed through humidifiers. To control the gas humidification, a water reservoir inside the humidifier was heated to the desired temperature. The temperature ramp to cool down the water reservoir was in the order of ~1 K min^{-1}, which indicates that this setup was built for stationary fuel cell operation. The gas pressures were adjusted at the outlets. Consequently, the gas inlet pressure resulted from a combination of gas volume flow and gas outlet pressure. The reaction products, such as water, were discharged through the cathode and anode exhaust. The cell temperature of the automotive size cells was adjusted with the coolant circuit using de-ionized water, which was pumped through the coolant manifolds of the BPP. The locations of the coolant manifolds are indicated in **Figure 3.4 A**. The coolant in the lab size

test items was pumped through channels in the current collectors. The coolant volume flow for the automotive size cells was 1.5 l_n min^{-1}.

An electrical load (see **Figure 3.5**) was used to control the current drawn from the test item. The load was connected to the cell in a four-terminal sensing configuration. The sense cables to measure the cell voltage were connected to the BPPs and the power cables to the current collectors. The power cables for automotive size cell experiments were designed for up to 1000 A while up to 200 A were possible for the 43.56 cm^2 cell tests. A potentiostat (IM6ex) provided by Zahner-Elektrik[246] was used for voltammetric and impedance-based characterization techniques. As the IM6ex was only capable of applying current amplitudes up to ± 2 A, a 4-quadrant power potentiostat (PP241, Zahner-Elektrik) was inserted between the potentiostat and the fuel cell (not illustrated in **Figure 3.5**), allowing AC amplitudes of up to ± 40 A. The voltage and current lines of the potentiostat were connected in a four-terminal sensing configuration.

3.2 Characterization Techniques

Cyclic voltammograms (CVs[f]), EIS and CDD maps were recorded using the potentiostat and a CSD. This section describes the implementation and data evaluation of those characterization techniques.

3.2.1 Cyclic Voltammetry and Parasitic Currents

Cyclic voltammetry (CV[f]) is a tool that characterizes (1) the capacitive behavior of an electrode and (2) adsorption processes. First, the separation of the electric phase (electrode) and the ionic phase (polymer) causes a capacitive behavior of the fuel cell called double layer capacitance. By nature, the capacitance is independent of electrode potential. Second, the adsorption and desorption of species on the catalyst surface cause electric currents across the electrode-electrolyte interface. These processes are typically dependent on electrode potential and will be labeled as pseudo-capacitance. For a CV measurement, the

[f] The abbreviation CV stands for cyclic voltammetry and cyclic voltammograms.

voltage is controlled as a triangular function of time and the current is evaluated as a function of voltage.

CVs were measured to determine the double layer capacitance, C_{dl}, the adsorption charges of the hydrogen underpotential deposition, Q_{HUPD}, and platinum oxidation, $Q_{Pt\text{-}OH}$. The CVs were recorded in the potential range between 0.09 V and 1.0 V with a sweep rate of 30 mV s^{-1}. An example of such a measurement is given in **Figure 3.6 A**. Before each CV measurement, five cleaning cycles were run at a sweep rate of 100 mV s^{-1} to remove adsorbates from the platinum surface.[247] The starting potential for the CV measurement was 0.4 V since no adsorption processes took place at this potential. The cell was operated with hydrogen at the anode and nitrogen at the cathode. In a CV measurement, no water is formed in the cathode catalyst layer, contrary to fuel cell operation. To adapt the conditions of the CV measurement to normal operation, the relative humidity of the gases was set to 100%. The operating parameters are listed in **Table 3.3**.

Table 3.3. Operational conditions to determine the fuel cell capacitance based on impedance spectroscopy and to record cyclic voltammograms.

Cell Temperature, °C	60
Anode gas relative humidity inlet, %	100
Cathode gas relative humidity inlet, %	100
Hydrogen volume flow per active area (anode), sccm cm^{-2}	7
Nitrogen volume flow per active area (cathode), sccm cm^{-2}	14.6
Anode gas outlet pressure, bar_{abs}	1.5
Cathode gas outlet pressure, bar_{abs}	1.05

There are two reasons why the CV, as shown in **Figure 3.6 A**, cannot be used directly for the determination of adsorption and double layer capacitances. First, the most negative currents occur in the CV between 0.08 V and 0.1 V. In this voltage range, the HER occurs, where protons at the cathode are reduced to gaseous hydrogen. The currents due to the formation and re-oxidation of molecular hydrogen are superimposed on the currents due to hydrogen adsorption. Second, the CV in **Figure 3.6 A** is not symmetrically positioned

around the horizontal line at 0 A, making it difficult to determine the double layer capacitance, C_{dl}. This is due to (1) short circuit currents flowing across the polymer membrane between the two electrodes and (2) hydrogen diffusing through the membrane to the cathode. The hydrogen gets oxidized at the cathode, and the protons are pumped back to the anode, causing a current across the external electric circuit. The sum of the short-circuit current and hydrogen crossover causes the parallel shift of the CV to larger currents and is referred to as the parasitic current in this work.

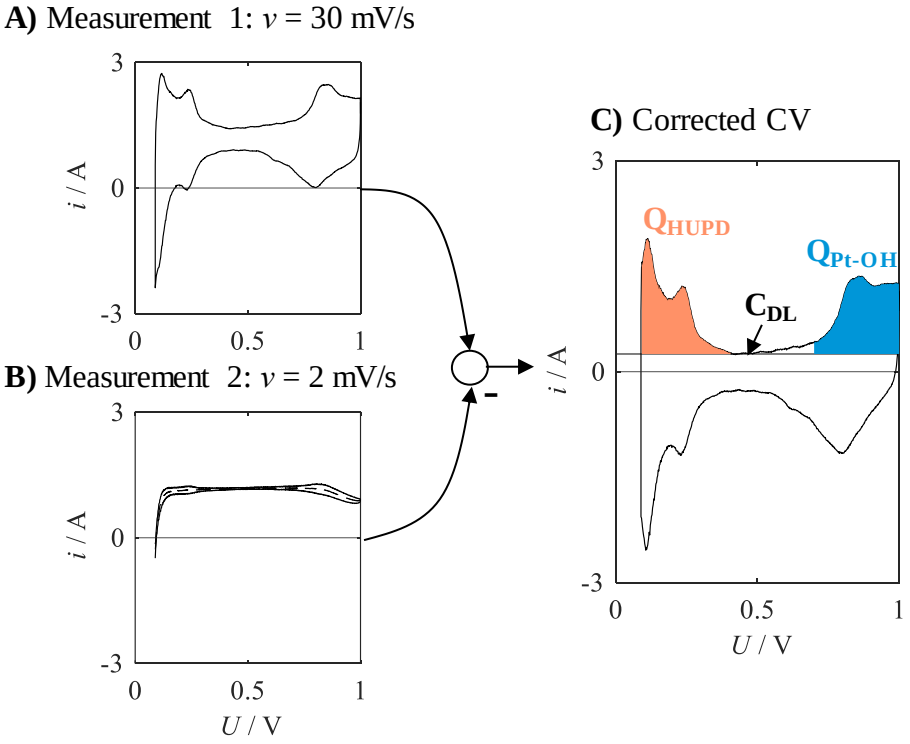

Figure 3.6. A) Cyclic voltammetric measurement using a potential sweep rate, υ, of 30 mV s^{-1} and **B)** measurement of parasitic and hydrogen evolution currents at 2 mV s^{-1} to calculate **C)** the cyclic voltammogram correct by parasitic and hydrogen evolution currents. From this diagram, we extracted the H^* and $^*OH$-adsorption charges, as well as the double layer capacitance.

To remove the effect of the HER and parasitic currents, CVs were measured at a sweep rate of 2 mV s^{-1}.[248] At such a low sweep rate, the currents due to adsorption processes and double layer effects are small, but the interfering effects of parasitic currents and hydrogen evolution are preserved. An example measurement is shown in **Figure 3.6 B**. From the CV at υ = 2 mV s^{-1}, the mean value of the current during the anodic and cathodic sweeps was

calculated (dashed line). This average current was subtracted from the CV which was measured at 30 mV s^{-1} in **Figure 3.6 A**. The resulting CV is shown in **Figure 3.6 C**. Finally, Q_{HUPD} could be calculated by integrating the CV in the range of the anodic sweep from 0.09 V to 0.4 V and dividing the result by the sweep rate. $Q_{Pt\text{-}OH}$ was determined in the range of 0.70 V to 1.0 V. The integrals of Q_{HUPD} and $Q_{Pt\text{-}OH}$ are colored in **Figure 3.6 C** as orange and blue areas. The double layer capacitance was determined using the averaged current between 0.4 V and 0.5 V, which was divided by the sweep rate.

3.2.2 Electrochemical Impedance Spectroscopy

In this work, electrochemical impedance measurement was evaluated as the methodology for real-time monitoring of fuel cells. To record an EIS, the fuel cell is probed at various frequencies, whereby solely sinusoidal oscillations were used here. For the measurement of stationary operating points, the EIS data were recorded between 300 mHz and 1 kHz with ten frequencies per decade, which took ~280 s.[205,249] Since the measurement time increases as the frequency decreases, EIS data for real-time monitoring was recorded between 120 Hz and 300 Hz at a total of five frequencies. The identification of the optimal frequencies is a part of chapter 4.1. The excitation signal for an impedance measurement can be voltage or current driven. In normal operation of the PEMFC, a galvanostatic excitation signal with amplitudes between 7 mA cm^{-2} and 35 mA cm^{-2}, depending on the operating point, was chosen. As the real-time EIS was intended to characterize dynamic operation the modulation amplitude was constant at 18 mA cm^{-2} independent on operating parameters. A potentiostatic AC excitation was not possible in normal operation, since in this case the DC component would also have to be potentiostatically. If the cell is operated potentiostatic, the cell voltage is kept constant, which makes impedance measurements impossible. This is an artifact of the parallel connection of the electrical load of the test stand and potentiostat used here, as previously illustrated in **Figure 3.5**. If measurements with low oxygen partial pressures were carried out, potentiostatic measurements were possible, whereby a voltage amplitude of 20 mV was selected. A summary of the EIS parameters is given in **Table 3.4**.

The stationary EIS data were validated in terms of linearity and causality using the Kramers-Kronig check.[250] CNLS fitting of the impedance data was done using the EIS

Data Analysis 1.3 software.[251] For real-time impedance investigations, no Kramers-Kronig checks were performed since the frequency range was too limited.

Table 3.4. Parameters for stationary and real-time electrochemical impedance spectroscopy measurements.

Stationary measurements	
Frequency range, Hz	0.3 – 1000
Measurement frequencies per decade	10
Galvanostatic mode	
Current amplitude for j_{cell} > 0.5 A cm^{-2}, A cm^{-2}	0.035
Current amplitude for j_{cell} < 0.5 A cm^{-2}, A cm^{-2}	0.0070
Potentiostatic mode	
Voltage amplitude, V	0.020
Real-time impedance measurements (RTIM)	
Frequency range, Hz	120 – 300
Amount of measurement frequencies	5
Current amplitude, A cm^{-2}	0.018

3.2.3 Current Density Distribution

The CDD along the air volume flow was recorded for automotive size MEAs using a CSD provided by S++ Simulation Services. A detailed description of the S++ functionality is given elsewhere.[252] The position of the CSD is between the BPP and the current collector at the cathode, as shown earlier in **Figure 3.3**. Graphite foils were placed on both sides of the CSD to achieve a homogeneous contact pressure distribution. The CSD as shown in **Figure 3.7 A** consisted of 32 segments in the y-direction and 18 segments in the x-direction, and the total area was 300 cm². Since the active area of the MEAs was smaller (~280 cm²), the edge segments of the CSD were neglected in the data analysis.

Figure 3.7 A shows the three cell components MEA, BPP, and CSD, with the measurement of local current densities, *j*, indicated as an example. The x-axis in **Figure 3.7 A** represents

the direction perpendicular to the flow-field channels, with the y-axis parallel to them. The current density is relatively homogeneously distributed in the x-direction and decreases from the air inlet (Air_{in}) to the air outlet (Air_{out}). The data shown in **Figure 3.7 A** were taken from the literature[126] and are only used to illustrate the measurement principle. In this work, we use a two-dimensional representation of the CDD. The local currents from **Figure 3.7 A** are shown as a CDD map in **Figure 3.7 B**. Air inlet and hydrogen inlet ($H_{2,in}$) are indicated corresponding to **Figure 3.7 A**. The color bar in **Figure 3.7 B** assigns the color in the distribution map to the corresponding current indicating ~1 A cm^{-2} close to the air inflow and ~0 A cm^{-2} at the hydrogen inflow.

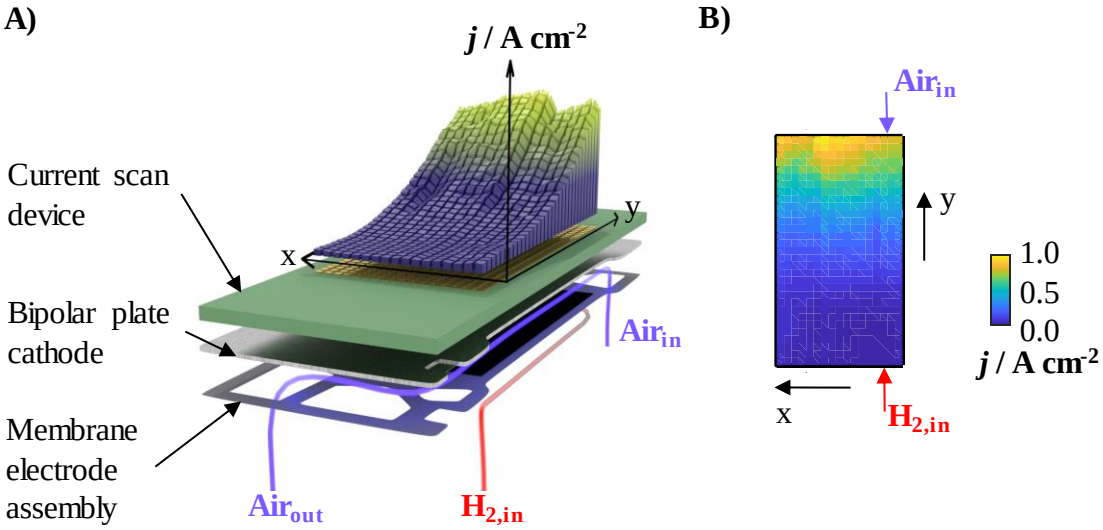

Figure 3.7. A) Current density distribution setup including the recorded data on top of current scan device for an automotive size cell (air inflow Air_{in}, air outflow Air_{out}). **B)** Two-dimensional current density distribution map corresponding to A) as an example for the way of representation used in this work. Reprinted with permission from ref. [126].

The CSD was meant to measure the CDD within the cathode catalyst layer. Between the CSD and the catalyst layer were the BPP and the GDL, as illustrated in **Figure 3.1** and **Figure 3.3**. These layers have an in-plane electrical conductivity that leads to differences between the CDD measured at the CSD and the cathode catalyst layer. This difference can be eliminated using a numerical model that includes the electrical conductivities of the

layers between CCM and CSD. In this work, the numerical approach similar to Haase *et al.*[253] and Herden *et al.*[254] based on a finite-volume framework[255] was applied.

3.3 Test Protocols

This section describes the operation of the fuel cells and is divided into the protocols for a startup (3.3.1), sensitivity analyses (3.3.2), and provoked PEMFC malfunctions (3.3.3).

3.3.1 Startup Procedure and Catalyst Activation

For comparability of the results, the cells were started with a uniform protocol before the characterizations. The startup can be divided into four phases and is shown in **Figure 3.8**. In the first step, the humidifiers are heated to set gas humidification of 80% (relative humidity). In addition, the cell temperature was set to 60 °C *via* the coolant circuit, and the gas lines were heated to ~70 °C. Heating the cell in the first step is essential to avoid condensation of water as soon as humidified gases flow through the PEMFC. In the second step, the cell was purged with nitrogen at the anode and cathode for 180 s to drive gaseous impurities out of the compartments. Preheating the gas humidifiers in the first step prevented the membrane from dehydration due to the nitrogen purge. Subsequently, the anode was supplied with hydrogen and the cathode with air, and after 60 s both gas pressures were raised to 2 bar_{abs}. In the third phase, the electrical current and hydrogen/air volume flows were successively increased up to a current density of 2.5 A cm^{-2}, while the gas stoichiometries were always kept above 1.6.

The startup procedure influences the CDD, depending on current ramps and stoichiometries. For this reason, the third step was optimized to achieve a homogeneous distribution of local currents at the highest current density of 2.5 A cm^{-2}. This optimization was done using an automotive size MEA (MEA #5, **Table 3.1**) in the setup SU #ii (see **Table 3.2**). In the last step, the current density was kept at 1 A cm^{-2} for 3600 s to activate the cell.[256] MEA activation (1) removes impurities introduced during the production process, (2) activates catalyst layers that do not participate in the reaction, (3) humidifies the polymer layers, and (4) optimizes mass transfer to the catalyst.[257]

The procedure as illustrated in **Figure 3.8** was run before each experimental investigation of automotive and lab size cells.

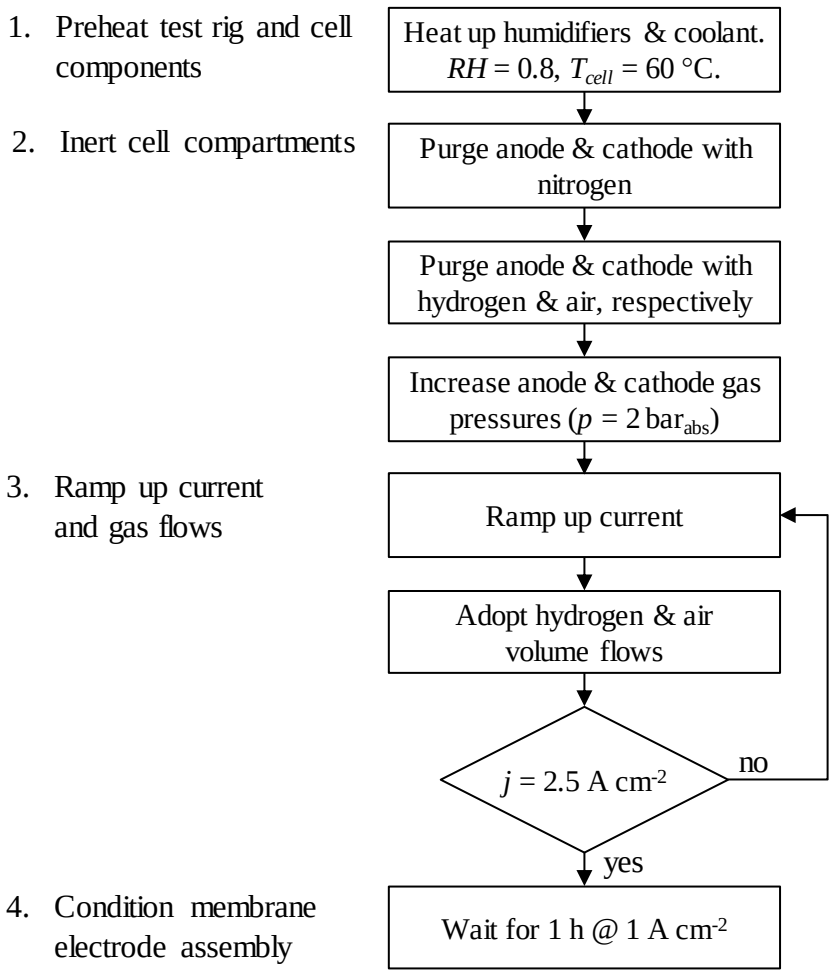

Figure 3.8. Startup procedure for fuel cell tests.

3.3.2 Sensitivity Analysis in an Automotive Parameter Map

To describe the behavior of the MEAs in normal operation, the sensitivity of the cell voltage and the EIS to different operating parameters was analyzed. The cell temperature T_{cell}, current density j, humidification of the gases RH, gas pressures p and the stoichiometries λ were varied. The tests were carried out both on the 43.56 cm² and on the automotive size cells. The range of operating parameters was adapted to the conditions occurring in vehicle operation.[258] The parameter variation for the automotive size cells was setup in such a way that four different current densities (0.5 A cm^{-2}, 1.0 A cm^{-2}, 1.5 A cm^{-2} and 2.0 A cm^{-2}) were applied at several combinations of gas humidification and cell temperature (e.g.

RH = 0.55 and T_{cell} = 65°C). At each current density, the gas pressures of hydrogen p_{H2} and air p_{Air} as well as their stoichiometries (λ_{H2}, λ_{Air}) were varied. During the variation of one operating parameter, the other parameters were kept constant, and these constant values are listed in **Table 3.5**.

Table 3.5. Operational parameter range for sensitivity analysis of the automotive and lab size fuel cells.

	Operational parameter	Unit	Constant Value	Variation Range
Automotive size cell	Hydrogen Stoichiometry	-	1.75	1.2 – 1.75
	Air Stoichiometry	-	2.2	1.4 – 2.4
	Hydrogen pressure @ outlet	bar_{abs}	2.0	1.8 – 2.1
	Air pressure @ outlet	bar_{abs}	1.8	1.7 – 2.0
Lab size cell	Hydrogen Stoichiometry	-	4.0	1.2 – 4.0
	Air Stoichiometry	-	4.0	1.2 – 4.0
	Hydrogen pressure @ outlet	bar_{abs}	1.8	1.7 – 2.3
	Air pressure @ outlet	bar_{abs}	2.3	1.7 – 2.3

The range of each operating parameter for the laboratory and automotive size cells are shown on the right in **Table 3.5**. To give an example, during the air stoichiometry variation of the automotive size cell, air stoichiometries between 1.4 and 2.4 were approached for a holding time of 10 min each. The remaining operating parameters during this were λ_{H2} = 1.75, p_{H2} = 2.0, and p_{Air} = 1.8. This variation was performed at various current densities, cell temperatures, and gas humidification, as shown in **Figure 3.9 A**.

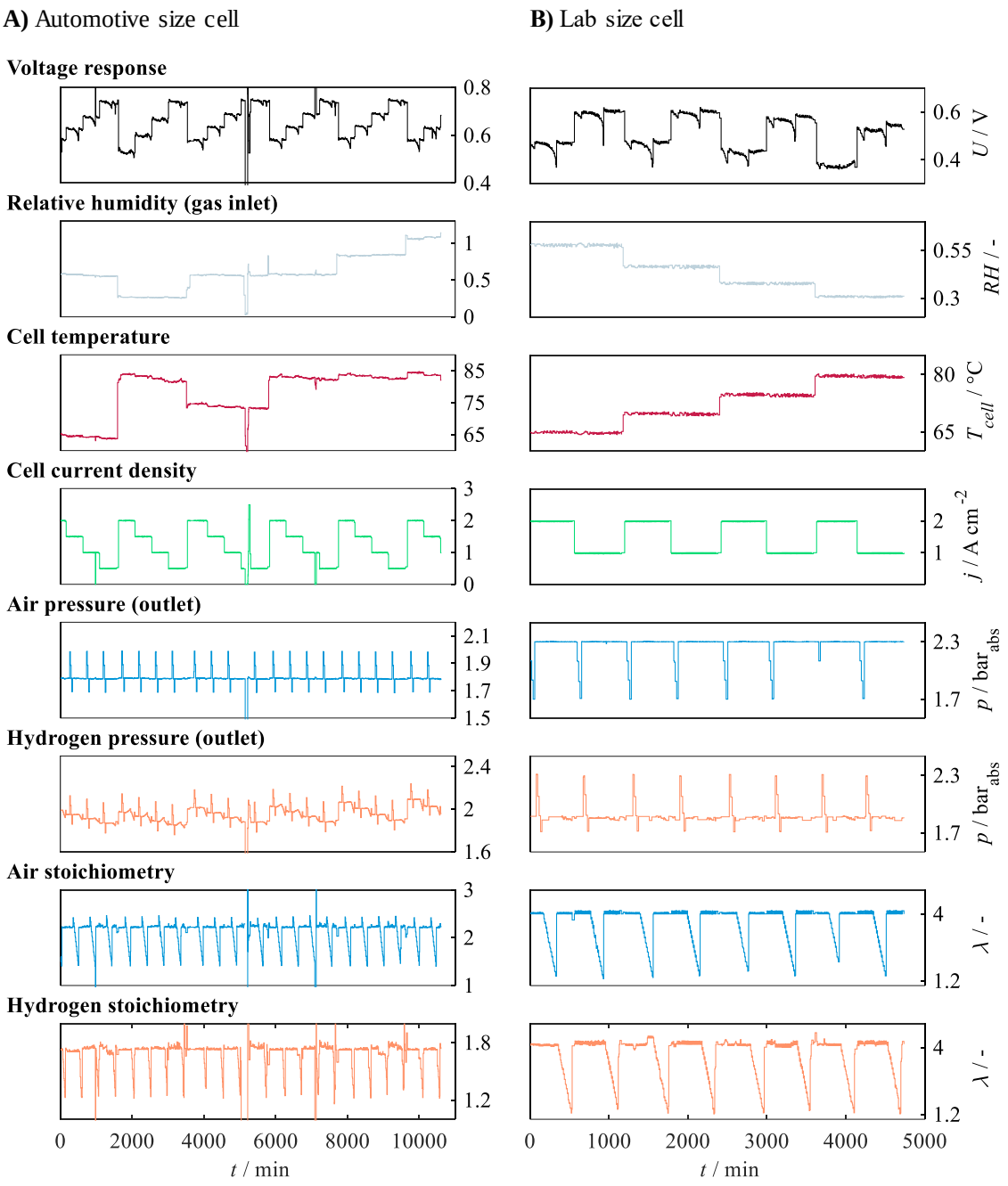

Figure 3.9. Sensitivity analysis of **A)** the automotive size cell using MEA #4 in **Table 3.1** and SU #iii in **Table 3.2** and **B)** the lab size cell using MEA #1 in **Table 3.1** and SU #i in **Table 3.2**.

The holding time of 10 min resulted from a 5 min waiting time to stabilize the cell voltage and the ~5 min to measure an EIS in the range of 300 mHz to 1 kHz. A total of 598 impedance spectra were recorded for the automotive size cell at various operating points.

The test procedure of the lab size cell was similar to the automotive size test protocols (see **Table 3.5** and **Figure 3.9 B**), but wider pressure and stoichiometry ranges were implemented. A total of 325 impedance spectra were recorded for the laboratory cell at various operating points. The EIS data were measured in stationary operation galvanostatically according to the parameters described in section 3.2.2.

3.3.3 Failure Analysis

One objective of this work was the detection of malfunctions in vehicle operation by means of impedance spectroscopy. Therefore, for the evaluation of a suitable measurement and evaluation methodology, hydrogen starvation, oxygen starvation and polymer dehydration were provoked on automotive size fuel cells. For the hydrogen starvation, an operating point with a current density of 0.55 A cm^{-2} was chosen because this current density was frequently encountered in vehicle operation. Since the hydrogen volume flow was reduced during the starvation experiment, the risk of water droplet formation inside the cell increased. To avoid this, the humidification was set to RH = 0.68. At the above operating conditions, the hydrogen stoichiometry was gradually decreased from 1.9 to 1.05 over a period of about 12 min. The corresponding operating parameters are listed in **Table 3.6**.

Table 3.6. Operational parameter range for failure analysis of the automotive size fuel cells.

	Limiting H_2 supply	Limiting air supply	Polymer dehydration
Current density / A cm^{-2}	0.55	0.55	0.7
Inlet gas humidification / -	0.68	0.68	0.11
Cell temperature / °C	65	65	85
Hydrogen stoichiometry / -	**1.9 to 1.05**	1.9	1.5
Air stoichiometry / -	1.6	**1.6 to 1.1**	**1.1 to 3.2**
Cathode outlet pressure / bar_{abs}	2.0	2.0	1.85
Anode outlet pressure / bar_{abs}	2.0	2.0	2.3

The conditions during the air starvation experiment were chosen according to the hydrogen starvation evaluation, whereby the air stoichiometry was lowered from 1.6 to 1.1 (see **Table 3.6**). To trigger the dehydration of the polymer, the humidification of the gases was lowered to $RH = 0.11$. In addition, to enhance the drying effect, the cell temperature was raised from 65 °C to 85 °C. Since this still did not cause enough dehydration, the polymer humidification was further reduced by ramping up the air stoichiometry from 1.1 to 3.2.

Since fuel cell operation is non-stationary during faulty conditions, recording steady-state EIS with a measurement time of several minutes was not practical. Therefore, the impedance behavior of the cells during the provoked fault cases was measured with the real-time impedance diagnosis, which will be presented in chapter 4.1. The corresponding EIS parameters have already been presented in **Table 3.6** under the category of real-time measurements.

4 Results and Discussion

One of the objectives of this thesis was to develop a physical impedance-based real-time methodology to monitor automotive size fuel cells in operation. In the first, part we introduce a measurement method that is most suitable for impedance monitoring of electrochemical systems. In chapters 4.2 and 4.3, the resistive and capacitive responses of automotive size PEMFCs are investigated. Afterward, an outlook on relevant degradation mechanisms during automotive operation is given (4.4). The last section (4.5) suggests a control strategy to extract relevant information on the PEMFC state of operation. An overview of the structure of this chapter is given in **Figure 4.1**.

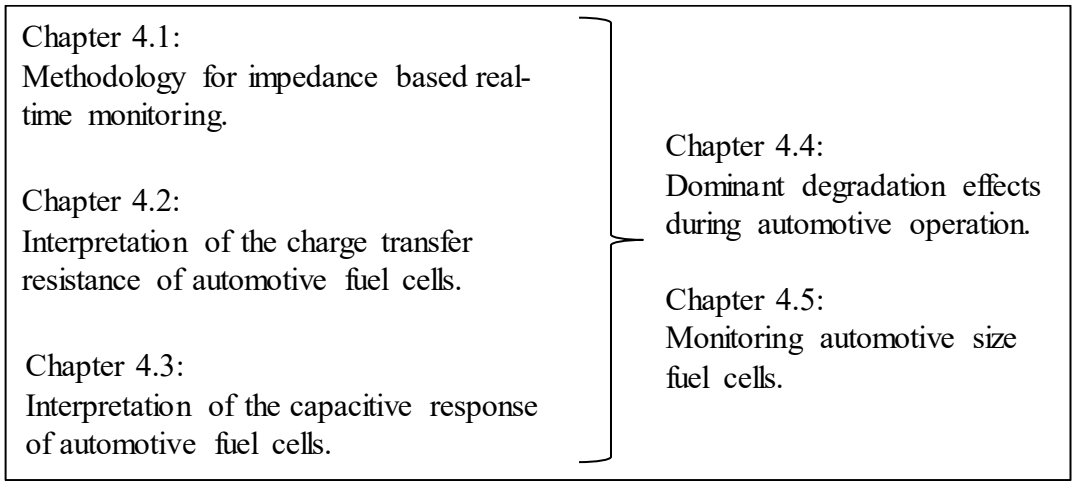

Figure 4.1. Structure of the Results and Discussion (chapter 4).

4.1 Real-time Impedance Analysis for Monitoring Automotive Fuel Cells

Parts of this chapter were published by the author of this thesis (among others) in the article 'Real-Time Impedance Analysis for the On-Road Monitoring of Automotive Fuel Cells'.[199]

A novel methodology to monitor automotive size PEMFCs is introduced in this chapter. In the following, this method will be called real-time impedance monitoring (RTIM) approach. First, aspects of PEMFC monitoring when using the cell voltage and impedance are described in chapter 4.1.1. Afterward, the RTIM approach based on DIA is developed. To verify the method, we compare the results to another impedance data processing technique in chapter 4.1.3. The sensitivity of the RTIM algorithm to PEMFC malfunctions is outlined in chapter 4.1.4.

4.1.1 Aspects of Fuel Cell Voltage and Impedance Monitoring

A sensitivity analysis of a 43.56 cm² PEMFC to various operating parameters was performed according to **Figure 3.9 B** on page 50. At each parameter set, an impedance spectrum between 300 mHz and 1 kHz was recorded. **Figure 4.2** illustrates every third recorded Nyquist plot (red), the cell voltage (orange) and the real part of the impedance, Z_{Re}, at 948 Hz (blue). The graph is presented to indicate the data basis to develop the RTIM method, so we will not go into detail on sensitivities here. A few general remarks on the comparison of the results with literature references are made in the following. (1) The HFR increases stepwise over time, corresponding to the four different relative humidities of the inflowing gases (0.58, 0.45, 0.36, 0.30).[69,78,211] (2) The impedance spectra consisted of two superimposed semicircles, with the semicircles at low frequencies sometimes greatly enlarged as seen in **Figure 4.2**. These increased impedances occurred at low air stoichiometries between 1.2 and 1.4.[222,223] (3) The cell voltage jumps between two plateaus at ~0.45 V and ~0.60 V corresponding to the current densities of 2 A cm^{-2} and 1 A cm^{-2}. The dips in cell voltages from these plateaus were mainly caused by the variation in air stoichiometry from 4 to 1.2.[223]

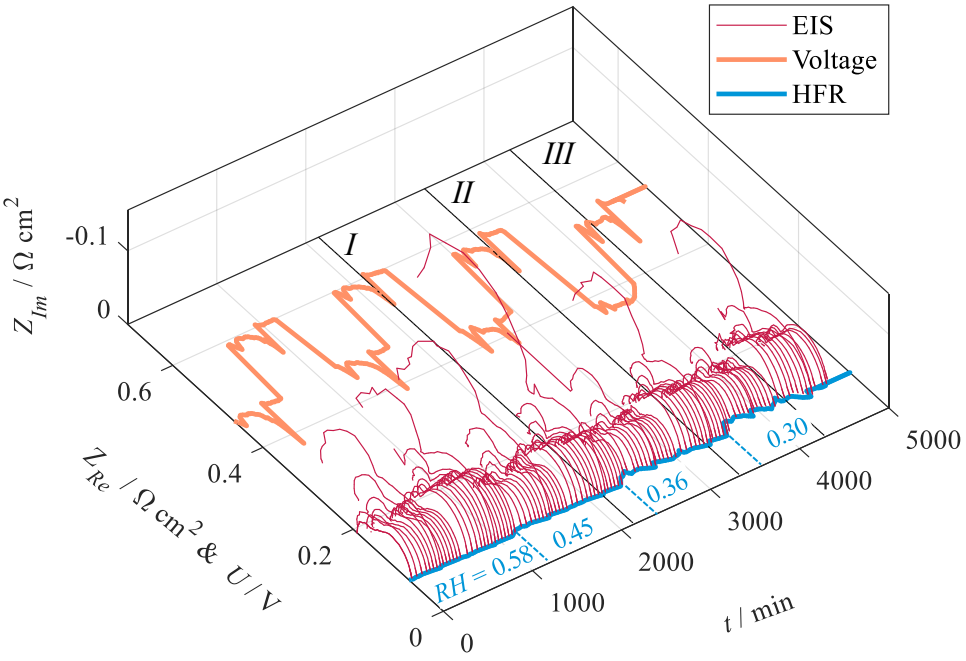

Figure 4.2. Voltage (orange), Nyquist plots (red) and high-frequency resistance (HFR, blue) during sensitivity analysis. Operational conditions according to **Figure 3.9 B**. Three points in time with similar voltages (0.53 V) are highlighted (*I*, *II*, *III*). The relative humidity of the inflowing gases is indicated using blue labels. The active area of the MEA was 43.56 cm² (MEA #1 in **Table 3.1**, SU #i in **Table 3.2**).

From the sensitivity analysis, three sets of operating parameters were extracted that showed an equal cell voltage of ~0.53 V. These operating points are labeled *I*, *II*, and *III* in **Figure 4.2** and were recorded at a current density of 1.0 A cm^{-2} and a hydrogen stoichiometry of 4.0. From the point *I* to *III*, the gas relative humidity *RH* decreases from 0.45 to 0.30, and the air stoichiometry λ_{Air} increases from 1.4 to 4.0. The impedance spectra at these operating points are shown in **Figure 4.3**. The simultaneous change of gas humidification and air stoichiometry affected the impedance of the PEMFC, while the cell voltage stayed constant. To gain further insights from the EIS measurements, the spectra were fitted with a bounded Randles circuit as shown in **Figure 2.10 A** (page 27) using a CNLS algorithm. The fits are plotted as solid lines in **Figure 4.3**.

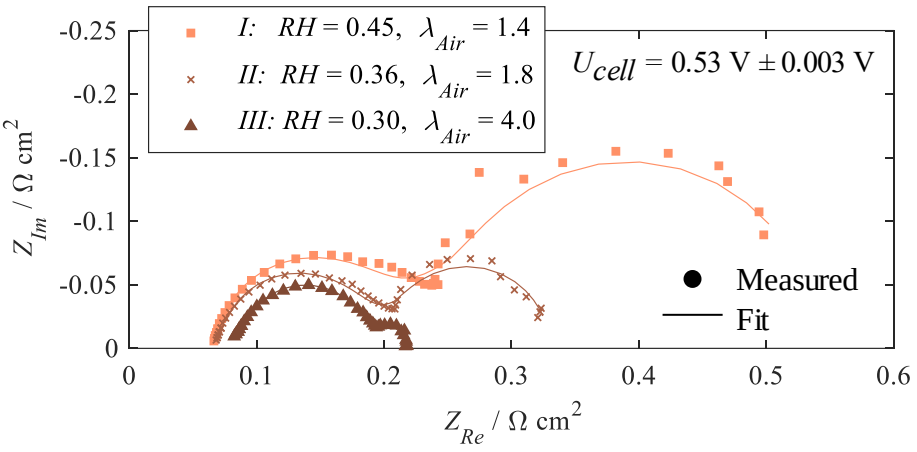

Figure 4.3. Electrochemical impedance spectra for a 43.56 cm² MEA extracted from **Figure 4.2** at three operating conditions (*I*, *II*, *III*). Data points indicate measured values, while the complex non-linear least-squares fits are displayed as lines according to the EEC in **Figure 2.10 A** on page 27.

The values for membrane resistance, R_{mem}, and charge transfer resistance, R_{ct}, are shown in **Figure 4.4 A**. The membrane resistance increases from the point *I* to *III* due to decreasing polymer humidification. As expected, the linear decrease in relative humidity *RH* (see **Figure 4.4 C**) leads to a non-linear increase in membrane resistance. In section 2.4.1, the relationship between polymer conductivity and humidification was described in more detail. The increase of the air stoichiometry promotes dehydration of the membrane and, therefore, additionally increases R_{mem}.[259,260] The charge transfer resistance in **Figure 4.4 A** decreases from the point *I* to *III*. In the literature, this behavior of R_{ct} has already been observed when increasing the air stoichiometry.[65,84,220] The cell voltage in **Figure 4.4 B** can be described by two effects. (1) Based on the trend of the membrane resistance, it can be concluded that the ohmic losses increase from the point *I* to *III*, causing a drop in cell voltage. (2) An increase in the oxygen partial pressure at the catalyst layer decreases the concentration overpotential and increases the cell voltage.[261] These two mechanisms cancel each other out at the operating points illustrated in **Figure 4.4**, keeping the cell voltage constant.

As shown in the example, membrane dehydration due to high air volume flows cannot be reliably detected using the cell voltage. Thus, fuel cell monitoring, which is solely based

on the voltage, can lead to misinterpretations. The impedance response in **Figure 4.4 A** reacted to the parameter variation, where the membrane resistance reflected humidification and the charge transfer resistance reflected the air stoichiometry.[69,211] This indicates that the impedance of PEMFCs contains valuable information regarding its state of operation.

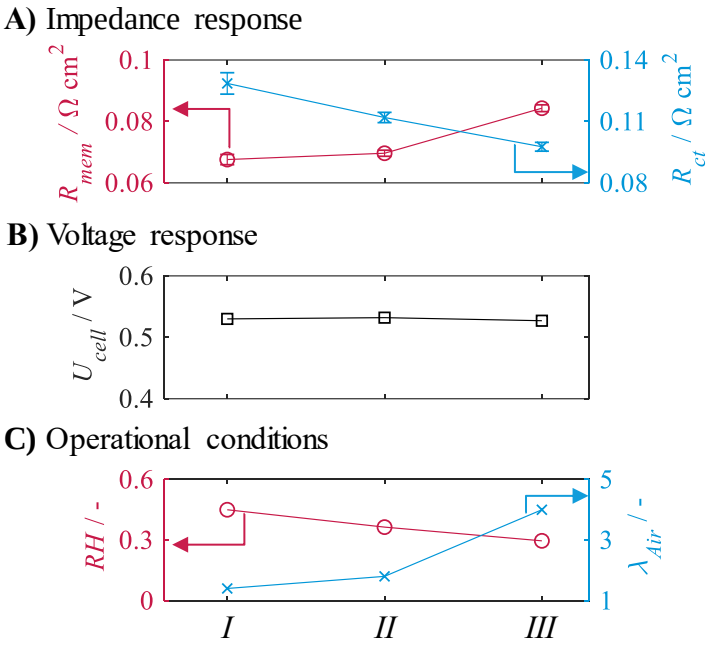

Figure 4.4. Impedance and voltage response to three operating conditions (*I*, *II*, *III* in **Figure 4.2**) at j_{cell} = 1.0 A cm^{-2} and λ_{H2} = 4.0. **A)** Membrane R_{mem} and charge transfer resistance, R_{ct}, based on impedance spectroscopy according to the Nyquist plots in **Figure 4.3**. **B)** Cell voltage, U_{cell}. **C)** Gas inlet humidification, *RH*, and air stoichiometry, λ_{Air}.

The measurement time to record one impedance spectrum during the sensitivity analysis in **Figure 4.2** is ~280 s, which is not practical for monitoring dynamic fuel cell operation in vehicles. To reduce the measurement time, one can measure the impedance at only one frequency. This frequency is usually at 300 Hz or 1 kHz to evaluate the hydration of the membrane.[77,78] It is assumed that the real part of the impedance, Z_{Re}, at this frequency corresponds to the membrane resistance, R_{mem}, or reflects its behavior. To assess the difference between Z_{Re}(300 Hz) and membrane resistance, an EIS was simulated based on a Randles circuit, which is illustrated in **Figure 4.5 A**. The values for R_{mem} (0.06 Ω cm²) and R_{ct} (0.1 Ω cm²) are in the range of the results of the sensitivity analysis in **Figure 4.4**.

Three different values between 0.005 F cm^{-2} and 0.03 F cm^{-2} were assumed for the double layer capacitance, C_{dl}. The corresponding Bode plots for the simulated EIS are shown in **Figure 4.5 B**.

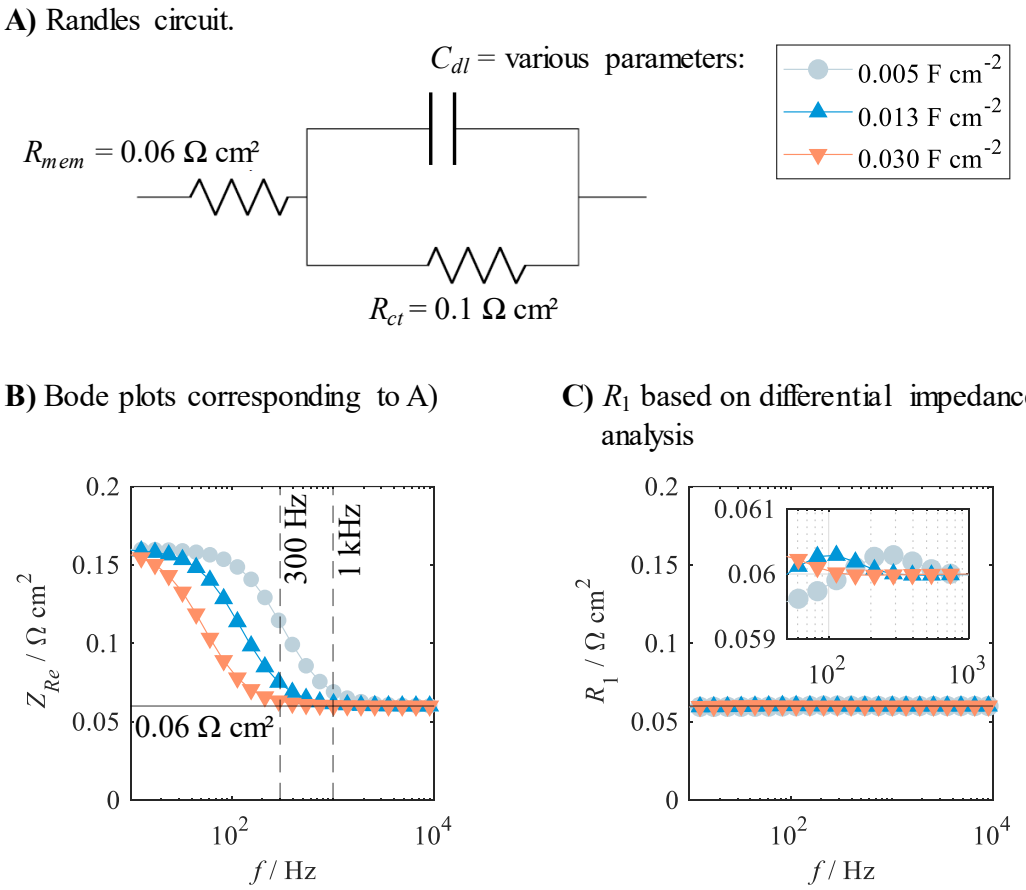

Figure 4.5. Identification of the membrane resistance based on impedance spectroscopy. **A)** Randles circuit. **B)** Simulated Bode plot, $Z_{Re}(f)$, of the Randles circuit in A) for three different double layer capacitances. **C)** $R_1(f)$ calculation based on **Eq. 4** (page 25) for three different double layer capacitances. Reprinted with permission from ref. [199].

At high frequencies (> 5 kHz), Z_{Re} corresponds to the membrane resistance of 0.06 Ω cm² for all three EISs. At low frequencies (≤ 10 Hz), Z_{Re} corresponds to the sum of membrane and charge transfer resistance (0.16 Ω cm²). The transition region between 10 Hz and 5 kHz depends on the double layer capacitance. The statement $Z_{Re}(f) = R_{mem}$ is valid for measurement frequencies larger than 200 Hz when C_{dl} = 0.03 F cm^{-2}. For the lower capacitance of 0.005 F cm^{-2}, this statement is valid only for f > 2 kHz. If one assumes that

Z_{Re}(300 Hz) = R_{mem} then the membrane resistance is overestimated with decreasing double layer capacitance. A collapse of the cell capacitance can be caused, for example, by the aging of the cell. Thus, as the cell ages, the risk of misinterpretation increases. One solution to this is to measure at higher frequencies of ~10 kHz. However, since inductive effects occur during fuel cell system operation, only measurement frequencies below 1 kHz are practical.[247]

In addition to the evaluation of a single frequency, we analyzed the Bode plots shown in **Figure 4.5 B** using DIA. For this purpose, the derivatives Z_{Re}, as well as Z_{Im}, must be formed over the frequency, *f*. The equations for this were presented earlier in chapter 2.3.3. Based on the derivatives, the parameters of the DIA can be determined as a function of frequency. These parameters are the resistances, R_1 and R_2, and the capacitance, *C*. The result for the resistance R_1 *versus* frequency, *f*, is illustrated in **Figure 4.5 C**. R_1 = 0.60 Ω cm^2 corresponds to the simulated membrane resistance in **Figure 4.5 A**. The differential impedance approach shows some advantages compared to the evaluation of a single frequency. (1) The R_1 resistance determined *via* DIA is less sensitive to the measurement frequency. In the inset of **Figure 4.5 C**, the R_1 resistance of 0.60 Ω cm^2 shows a deviation of up to ± 1.0%. This was caused by the use of discrete frequencies in the data evaluation. (2) In addition to R_1, the DIA determines the resistance R_2 and the capacitance, *C*, which increases the expressiveness of the impedance measurement. In the following, the implementation of DIA for real-time analysis of PEMFCs is considered in detail.

4.1.2 Real-time Impedance Monitoring Methodology

Figure 4.5 shows that the DIA approach represents a good approximation for the calculation of the membrane resistance over a wide frequency range. In this example, the measurement of a smaller frequency range, e.g. between 100 Hz and 500 Hz, is sufficient to evaluate the impedance signal. The theoretical background on DIA was previously given in chapter 2.3.3 on page 23. For the determination of the LOM parameters, one requires the impedance information consisting of angular frequency, ω, imaginary part, Z_{Im}, and real part, Z_{Re}, as well as their derivatives. The LOM is illustrated in **Figure 4.6 A**. **Figure 4.6 B** shows a Nyquist plot with the typical shape for a PEMFC.

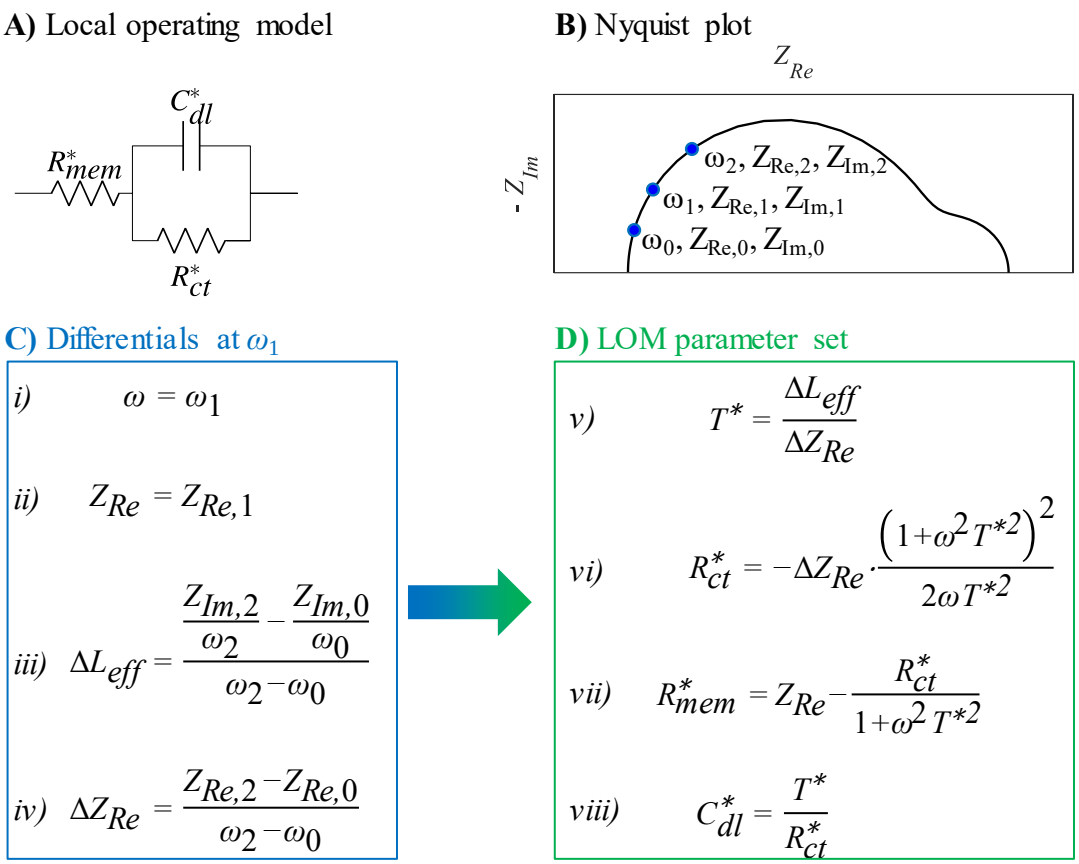

Figure 4.6. Determining the local operating model (LOM) parameters. **A)** Local operating model. **B)** Nyquist plot (black line) including three impedances at various frequencies (blue dots). **C)** Equations to calculate the derivatives of real and imaginary impedance. **D)** Extracting the LOM parameters based on the equations in C.

We now assume that we want to calculate the parameters of the LOM at the frequency ω_1 in **Figure 4.6 B**. To do this, the frequency ω_1 and the corresponding real part impedance, $Z_{Re,1}$, must be extracted as shown in equations *i)* and *ii)* in **Figure 4.6 C**. In addition, the derivatives of the effective inductance and the real part are required. To ensure an analytically simple calculation, these derivatives are presented in the linearized form in equations *iii)* and *iv)* in **Figure 4.6 C**. Two further impedance measurements, one at lower and one at a higher frequency than ω_1 are necessary. These data points are marked in **Figure 4.6 B** as ω_0 and ω_2, where $\omega_0 > \omega_1 > \omega_2$. Based on the imaginary parts of the impedance $Z_{Im,2}$ and $Z_{Im,0}$, the derivative of the effective inductance, ΔL_{eff}, can thus be determined. Similarly, the linearized derivative of the real part, ΔZ_{Re}, is formed. The four

values (ω, Z_{Re}, ΔL_{eff}, ΔZ_{Re}) shown in **Figure 4.6 C**, are directly calculated from the impedance data and serve as input quantities to determine the LOM parameters. First, the time constant T^* is calculated as shown in equation *v)* in **Figure 4.6 D**. Finally, the parameters for the charge transfer resistance, R^*_{ct}, the membrane resistance, R^*_{mem}, and the double layer capacitance, C^*_{dl}, are calculated according to the equations *vi)* to *viii)* in **Figure 4.6 D**. It is important to mention that the LOM parameters in **Figure 4.6 D** have now been calculated for the frequency ω_1 and that for the determination of this set of LOM parameters, impedances at three different frequencies were necessary.[194,196]

With the equation system presented in **Figure 4.6**, information about the PEMFC can be extracted based on three frequencies. Earlier (**Figure 4.5**), an impedance spectrum was simulated based on a Randles circuit. When analyzing this simulated spectra with DIA, the error in the membrane resistance is below 1%. This simulation is shown again in **Figure 4.7 A**, where the results for R_{ct} and C_{dl} are additionally illustrated.

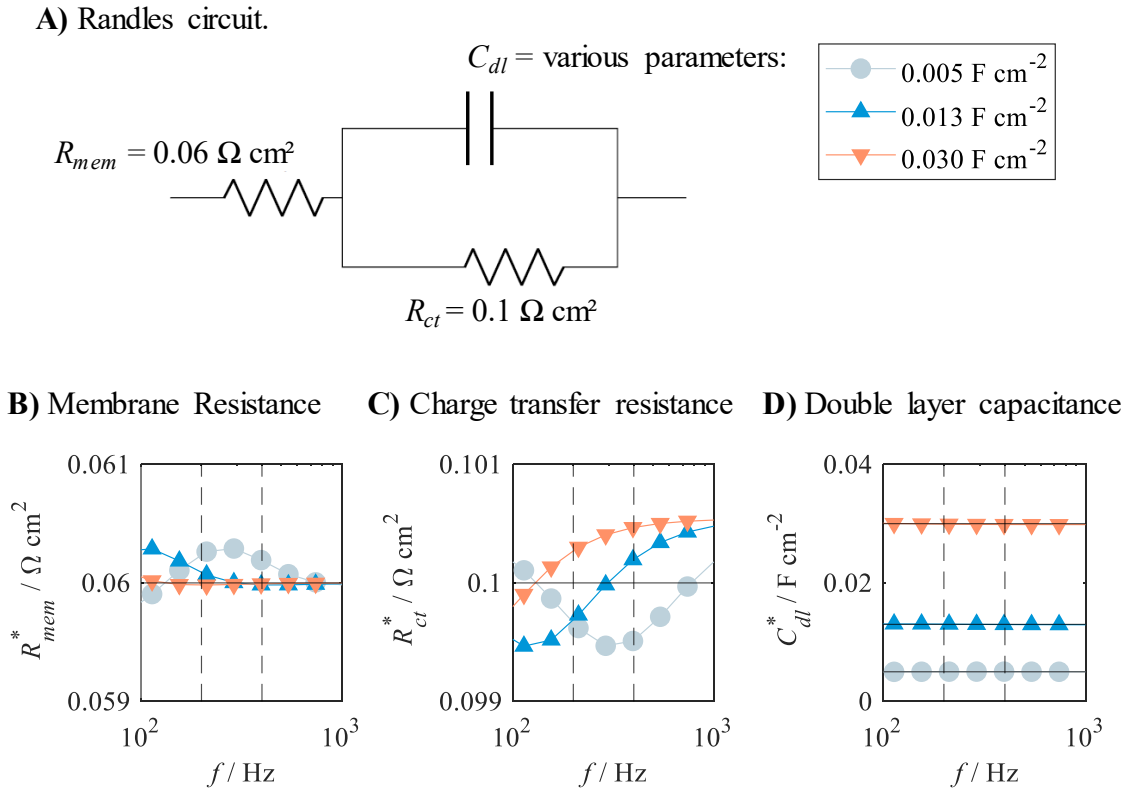

Figure 4.7. Evaluation of simulated impedance spectra based on a Randles circuit using differential impedance analysis (DIA) according to **Figure 4.6**. **A)** Randles circuit. Extraction of **B)** membrane resistance, **C)** charge transfer resistance, and **D)** double layer capacitance, based on DIA.

All three LOM parameters show deviations of less than ±1% from the simulated values between 100 Hz to 1kHz, whereby a frequency dependence is evident. For this reason, instead of performing the DIA as illustrated in **Figure 4.6** at only one frequency, we suggest including several frequencies. As an example, vertical lines at 200 Hz and 400 Hz are added to **Figure 4.7 B**, **C** and **D**. In this frequency range, there are three data points for each LOM parameter. It is suggested that an average of the three values be taken to increase the method's robustness towards variations in the LOM parameters (in this example, variations in capacitance).

We now work with the assumption that three LOM parameter sets achieve good accuracy in determining R_{mem}, R_{ct} and C_{dl}. Since three different measurement frequencies are required for each set, the impedance must be measured at a total of five frequencies. The question arises, which frequencies should be selected for monitoring PEMFCs. A few framework conditions must be considered here. (1) To obtain information about the kinetic behavior of the cathode, the measured impedance data must lie on the kinetic arc in the Nyquist plot, i.e. between ~20 Hz and ~300 Hz.[262] In addition, effects due to oxygen oscillation below 10 Hz to 50 Hz can superimpose the kinetic arc.[171,240] (2) To minimize inductive cross-impact from the fuel cell system, frequencies lower than 300 Hz are reasonable. (3) To keep the measurement time low, the measurement frequencies should be high. (4) In applications, the measurement frequency cannot be precisely adjusted. In addition, interferences can occur at some frequencies. The five impedance measurements should therefore be distributed over the kinetic arc as far as possible. To sum up, a frequency range between 100 Hz and 300 Hz is initially proposed to match real-word application and fundamental electrochemical requirements.

The approach in **Figure 4.6** is based on a linearization of the impedance derivatives. Therefore, it can be assumed that the five measurement frequencies should be as close as possible to each other to increase accuracy. This contradicts the conclusions related to real-world applications that suggest distributing the frequencies across the kinetic arc. The influence of the measurement frequency distribution on the accuracy of the DIA approach shall now be analyzed in more detail. To consider the influence of the distribution of impedances on the kinetic arc, an impedance spectrum was simulated based on a Randles circuit (as shown in **Figure 4.7 A**) with the parameters R_{mem} = 0.1 Ω cm², R_{ct} = 0.2 Ω cm², and C_{dl} = 0.02 F cm^{-2}. The simulated impedance spectrum is plotted in **Figure 4.8 A** to **C**.

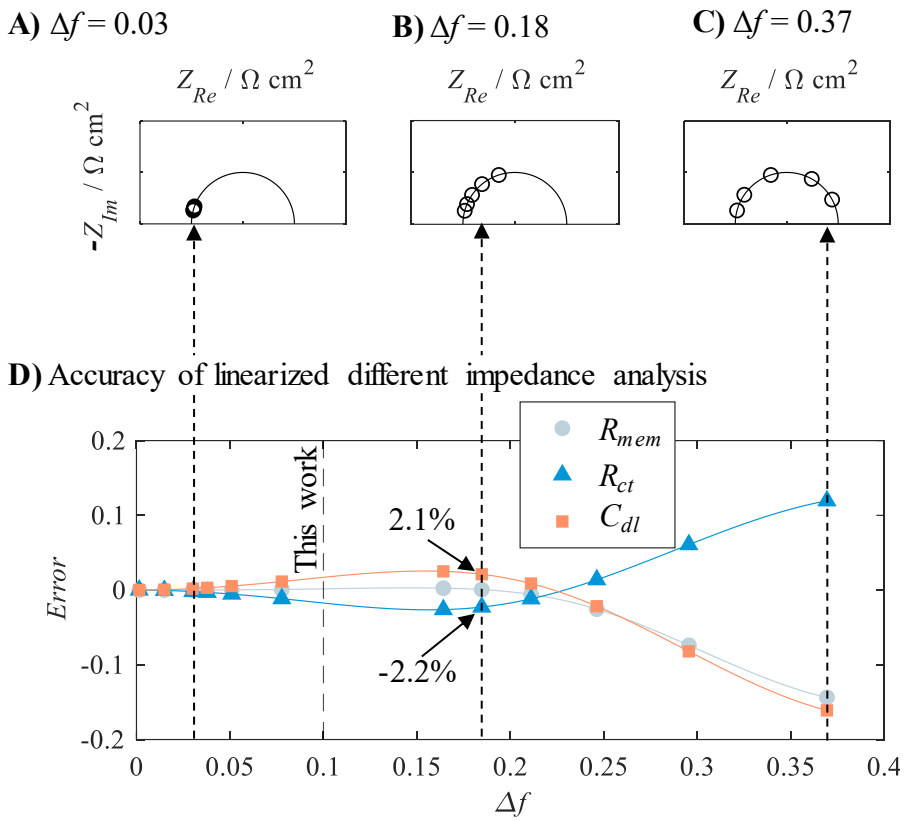

Figure 4.8. Accuracy of the linearized differential impedance approach using five evaluation frequencies. **A)** Nyquist plots (black line) with five impedance data points with a frequency distribution of Δf = 0.03. **B)** Δf = 0.18. **C)** Δf = 0.37. **D)** Error of the local operating model parameters *versus* frequency distribution. Membrane resistance: R_{mem}, charge transfer resistance: R_{ct}, double layer capacitance: C_{dl}.

Since frequencies are typically distributed in a logarithmic range, we define $\Delta f = \log_{10}(f_1/f_2)$, where $f_1 > f_2$. In **Figure 4.8**, five impedance values with different frequency distributions are plotted in each of the Nyquist plots, where the distribution is narrow in **Figure 4.8 A** (Δf = 0.03) and wide in **Figure 4.8 C** (Δf = 0.37). The example of Δf = 0.18 is used to explain the influence of frequency distribution on the error of the LOM parameter determination. The impedances in **Figure 4.8 B** allow to extract three LOM parameter sets for R^*_{mem}, R^*_{ct} and C^*_{dl}, according to **Figure 4.6**. To give an example, there are three values for R^*_{mem}, which are averaged and referred to as $R_{mem,calc}$. The difference between the simulated $R_{mem,sim}$ and $R_{mem,calc}$ is calculated as $Error = 1 - (R_{mem,calc}/R_{mem,sim})$ and illustrated in **Figure 4.8 D**. This is done similarly for R^*_{ct} and C^*_{dl}. **Figure 4.8 D** shows that for the frequency distribution Δf = 0.18, C_{dl} and R_{ct} have a deviation of ± 2.2%. If a

larger frequency distribution of 0.37 is chosen (**Figure 4.8 C**), the LOM parameters show an error of ± 16%. As expected, the linearization of the DIA is more accurate when the frequency distribution is small. It was concluded from the real-world requirements to use large distributions, and therefore it is suggested that $\Delta f \leq 0.10$, so the error of all LOM parameters remains below ± 2 %. The recommendation for the five measurement frequencies is 119 Hz, 150 Hz, 189 Hz, 238 Hz, and 287 Hz.

The linearized DIA, including averaging of one or more LOM parameter sets, is called the real-time impedance monitoring (RTIM) method. The approach is summarized in the following paragraph using **Figure 4.9**.

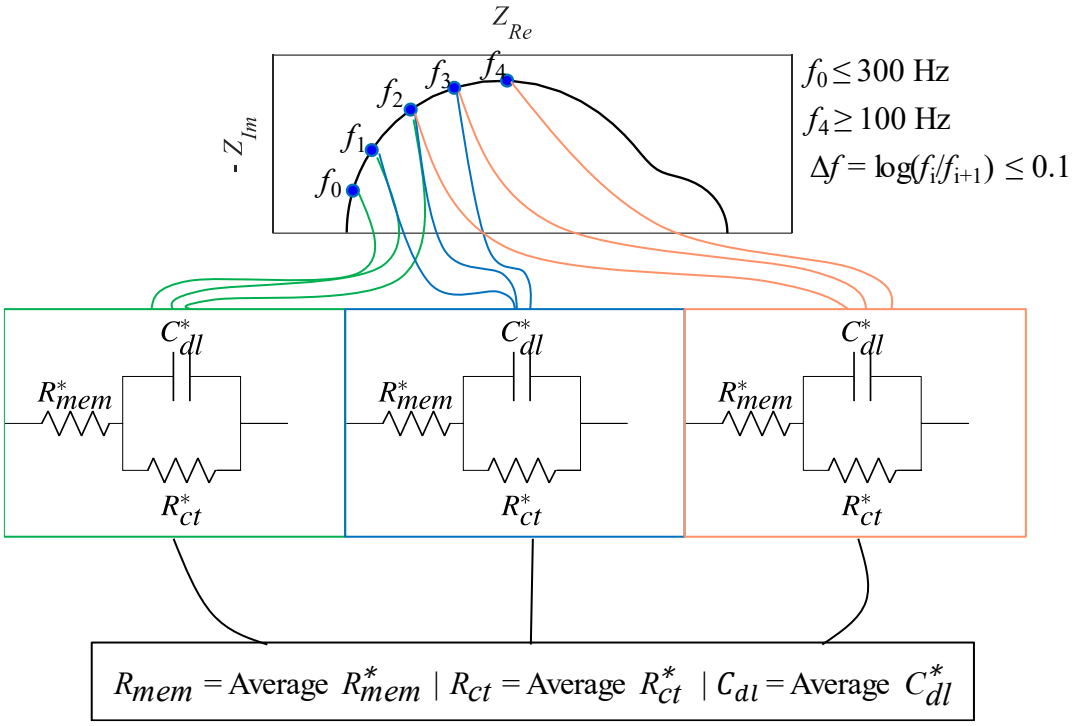

Figure 4.9. Real-time impedance monitoring (RTIM) methodology. **(top)** Nyquist plot including five impedance data points (blue) at different frequencies *f*. **(middle)** Local operating models to process the impedance data (for the detailed calculations in this step, see **Figure 4.6**). **(bottom)** Averaging the LOM parameters. Membrane resistance, R_{mem}, charge transfer resistance, R_{ct}, double layer capacitance, C_{dl}.

The left semicircle in the Nyquist plot in **Figure 4.9** represents the kinetic arc of the cathode. Within this arc, five measurement points are indicated as blue dots, corresponding to different measurement frequencies. The highest measurement frequency (f_0) should be smaller than 300 Hz, and the lowest measurement frequency (f_4) should be larger than

100 Hz. The distance between the frequencies must not be more than $\Delta f = 0.1$, which translates to a minimum of ten frequencies per decade. From the five impedances, three different sets can be extracted, which correspond to the lines with the colors green, blue and orange in **Figure 4.9**. With each of these parameter sets, the LOM parameters (R^*_{mem}, R^*_{ct}, C^*_{dl}.) are now calculated based on **Figure 4.6**. Subsequently, the values, e.g., of R^*_{mem} are averaged to obtain the final membrane resistance, R_{mem}. The analytical nature of the algorithm allows rapid data processing.

4.1.3 Method Validation

This section validates the RTIM methodology described in section 4.1.2. First, impedance measurements on a PEMFC (43.56 cm²) are compared using the RTIM and CNLS fitting methodologies. Second, a sensitivity analysis is performed on an automotive size PEMFC, and the behavior of the RTIM parameters is compared with the expectations from the literature.

The sensitivity of cell voltage and impedance to various operating parameters were measured on a laboratory cell, as shown earlier in **Figure 4.2** (page 55). These impedance spectra were fitted with a bounded Randles circuit (see **Figure 2.10** on page 27), extracting membrane resistance, R_{mem}, charge transfer resistance, R_{ct}, and double layer capacitance, C_{dl}.[205] The results over the entire course of the experiment are shown as blue lines in **Figure 4.10 A** to **C**. For the same impedance spectra, R_{mem}, R_{ct} and C_{dl} were also extracted using the RTIM method, but for this evaluation, only the frequencies 150 Hz, 189 Hz, 238 Hz and 300 Hz were included, which corresponds to the established criteria in **Figure 4.9** ($f_{min} \leq 300$ Hz, $f_{max} \geq 100$ Hz, $\Delta f \leq 0.1$). These results are shown in **Figure 4.10 A** to **C** as orange lines, along with the CNLS results. The membrane resistance increased with time for both the RTIM and CNLS results, which is a consequence of the reduction in gas humidification (see **Figure 3.9 B** on page 50).

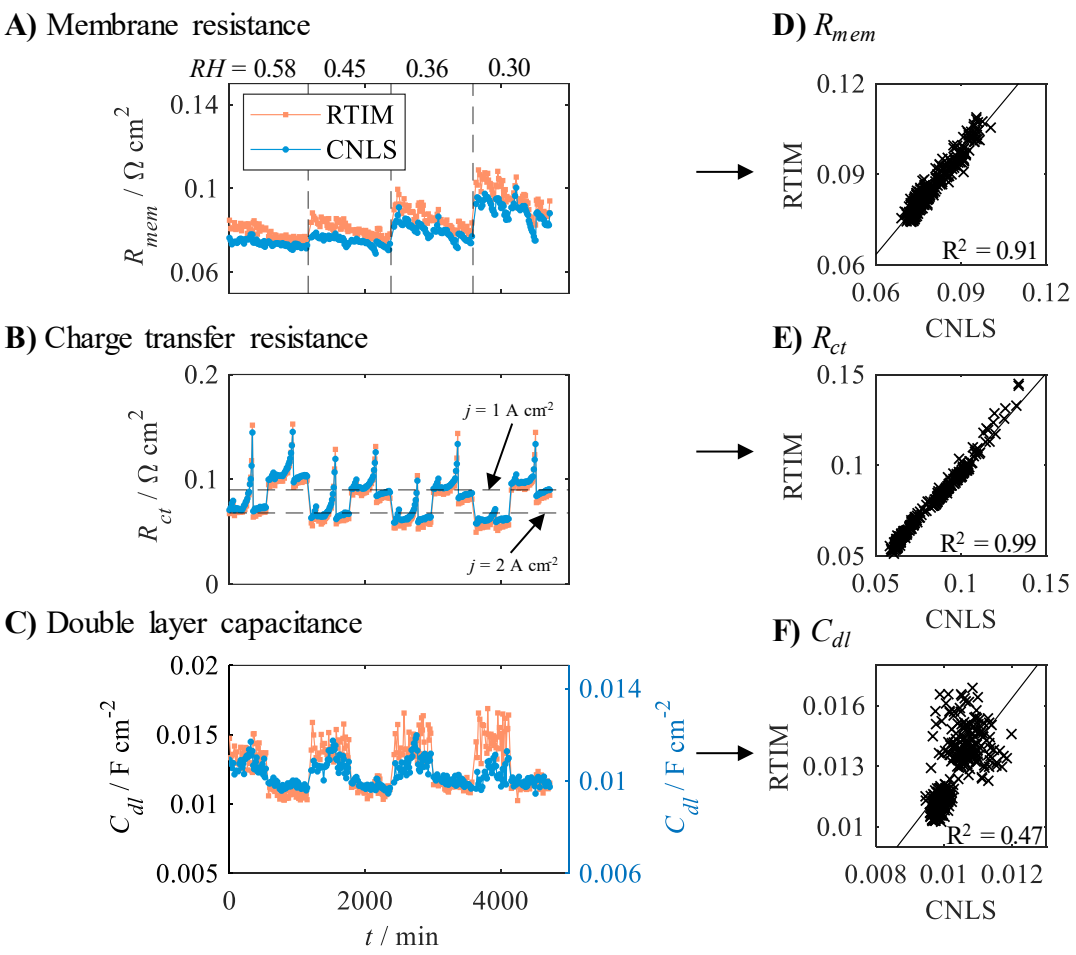

Figure 4.10. Comparison of the real-time impedance monitoring (RTIM) approach to complex non-linear least-squares fitting (CNLS) using a lab size single cell (MEA #1 in **Table 3.1**, SU #i in **Table 3.2**). Temporal developments of **A)** membrane resistance, R_{mem}, **B)** charge transfer resistance, R_{ct}, and **C)** double layer capacitance, C_{dl}. Comparison of RTIM to CNLS for **D)** R_{mem}, **E)** R_{ct}, and **F)** C_{dl}. Reprinted with permission from ref. [199].

The relative humidity, *RH*, is indicated by vertical lines in **Figure 4.10 A** and correlate with the stepwise increase in membrane resistance. Qualitatively, the trends of R_{mem} are similar for both methods. To make a quantitative statement, the membrane resistance based on the RTIM methodology is plotted against the CNLS results in **Figure 4.10 D**. The agreement between the two approaches is $R^2 = 0.91$ (agreement based on the root mean square method). The RTIM determined values for R_{mem} ~10% larger than the CNLS fitting algorithm. It is suspected that this is an artifact of the different frequency ranges in the

RTIM and CNLS evaluations. When using a frequency range of 1 kHz to 2 kHz for the RTIM, the agreement between both methods for R_{mem} was $R^2 = 1.0$.

The charge transfer resistance, R_{ct}, over the course of the experiment are shown in **Figure 4.10 B**. Again, the plots of CNLS and RTIM are in good qualitative agreement. Two plateaus can be seen, which are marked with horizontal lines. These plateaus correspond to the variations in current densities, j, between 1 A cm^{-2} and 2 A cm^{-2} (experimental in **Figure 3.9 B** on page 50). As R_{ct} is proportional to j^{-1}, the course in **Figure 4.10 B** is plausible. The agreement of CNLS and RTIM assuming a linear correlation is $R^2 = 0.99$, as indicated in **Figure 4.10 E**. As already described for the evaluation of R_{mem}, the root mean square error for R_{ct} depends on the included frequency range in the RTIM analysis. In contrast to R_{mem}, however, for R_{ct} the error increases when the RTIM evaluation frequencies are larger. This is plausible since information about the kinetics are expected to be in the range 50 Hz to 500 Hz. As such, determining R_{ct} at 1 kHz to 2 kHz results in lower accuracy.

Figure 4.10 C shows the double layer capacitance, C_{dl}, with the CNLS fitting results corresponding to the right Y-axis. The C_{dl} values based on the RTIM and CNLS fitting methodology do not always agree here, which is also evident from a low value of $R^2 = 0.47$ in **Figure 4.10 F**. When calculating C_{dl} based on the RTIM approach in the range between 1 kHz and 2 kHz, the values fit better to the CNLS results with $R^2 = 0.71$. The capacitance in porous PEMFC electrodes is dependent on frequency[263] and therefore, typically a constant phase elements is used instead of a capacitance for CNLS fitting.[208,264] This explains the poor correlation in **Figure 4.10 F**.

It can be concluded that the RTIM method provides comparable values to CNLS fitting algorithms for the resistances R_{mem} and R_{ct}. The agreement of the capacitance is poor, as the C_{dl} values depend for both RTIM and CNLS methodology on the considered frequency range. For future work, it is recommended to use a constant phase element instead of a capacitor in the EEC and compare the CNLS fitting results with secondary DIA. The secondary DIA allows the determination of the constant phase element behavior and again enables the real-time capability of the measurement.[194]

The previous design and validation of the RTIM methodology were done using cells with an active area of 43.56 cm^2. The goal of this work is to evaluate the monitoring of

automotive size PEMFCs using EIS, so the sensitivity analysis of a cell with 285 cm² is considered in more detail below. The operating parameters were presented in **Figure 3.9 A** on page 50. The parameters for gas humidification, stoichiometries, gas pressures, current density and cell temperature were varied. In the following, it will be analyzed to what extent the impedance reflects the expected behavior from the literature. **Figure 4.11 A** shows the variation in membrane resistance during the sensitivity analysis over a period of ~170 h.

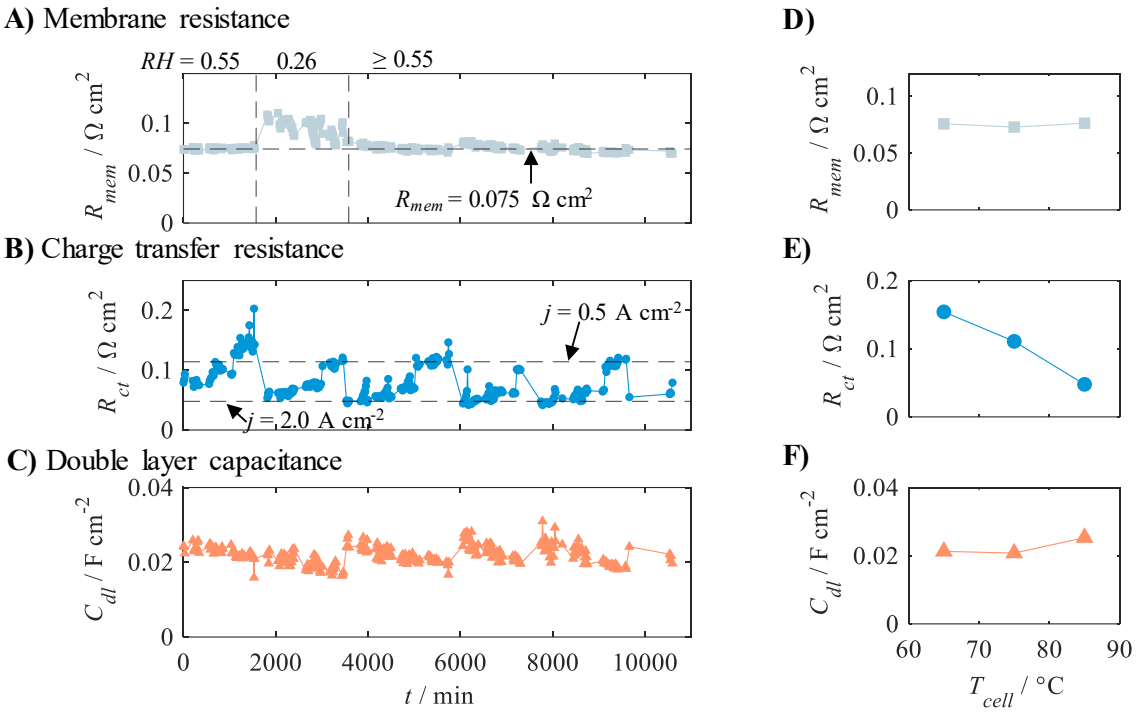

Figure 4.11. Sensitivity analysis of the real-time impedance monitoring approach for an automotive size single cell (MEA #4 in **Table 3.1**, SU #iii in **Table 3.2**). Temporal developments of **A)** membrane resistance, R_{mem}, **B)** charge transfer resistance, R_{ct}, and **C)** double layer capacitance, C_{dl}. Dependence on the temperature at 0.5 A cm^{-2} and 0.55% *RH* for **D)** R_{mem}, **E)** R_{ct}, and **F)** C_{dl}.

R_{mem} was ~0.075 Ω cm^2 for most of the time, indicated by a horizontal line in **Figure 4.11 A**. Between ~1500 h and ~3500 h, R_{mem} increases to larger values, corresponding to the period with the lowest gas humidification of *RH* = 0.26. This behavior is plausible, as described in section 2.4.1 on page 28, due to the linear relationship between membrane proton conductivity and water content. **Figure 4.11 D** shows the membrane resistance as a function of cell temperature at a current density of 0.5 A cm^{-2}. In general,

the membrane resistance shows low sensitivity to both temperature and current density, as expected from the literature.[68] **Figure 4.11 B** illustrates the charge transfer resistance over time with several plateaus due to the different current densities as already observed in the laboratory cell experiments. Two plateaus corresponding to the R_{ct} values at 0.5 A cm^{-2} and 2.0 A cm^{-2} are shown with horizontal lines, whereby this sensitivity can be described by the Tafel behavior of the oxygen reduction reaction.[73] The charge transfer resistance decreases with increasing temperature in the range of 65 °C to 85 °C (**Figure 4.11 E**), which has been observed several times.[220,265] The temporal course of the double layer capacitance is illustrated in **Figure 4.11 C**, showing a rather constant value of C_{dl} =22 ± 2.4 mF cm^{-2}. There are only a few publications dealing with the dependence of the double layer capacitance, C_{dl} on PEMFC operating parameters. Often it is assumed and measured to be constant,[264,266] which is confirmed by **Figure 4.11 C**. The impact of temperature on C_{dl} as indicated in **Figure 4.11 F** is small.

In summary, the RTIM methodology is a valid tool to characterize PEMFCs during operation as it (1) gives similar results to the state-of-the-art methods such as CNLS fitting and (2) the sensitivity on operational parameters agrees with literature findings.

4.1.4 Operational Failure Detection

The behavior of the RTIM methodology at various PEMFC operational malfunctions was analyzed in **Figure 4.12**. The corresponding experimental procedures can be found in chapter 3.3.3 (page 51). Three different failure cases were simulated. Meanwhile, the EIS was measured using the RTIM method as previously introduced in **Figure 4.9**. In the first attempts, impedance spectra in the range from 300 mHz to 10 kHz were recorded to be able to use CNLS fitting methods. The measurement time of ~280 s was too long due to the dynamic characteristics of faults in fuel cell operation. This highlights the need for real-time methods, such as the RTIM approach, for fuel cell monitoring.

Figure 4.12 A shows the behavior of the cell voltage and the RTIM elements when limiting the air supply. The cell voltage dropped from 0.73 V to 0.65 V when lowering the air stoichiometry, λ_{Air}, from 1.6 to 1.15. Below λ_{Air} = 1.3, the voltage became unstable. The membrane resistance, R_{mem}, was not affected during the measurement, while the charge transfer resistance, R_{ct}, increased with decreasing air supply.[83,222,267] The double layer capacitance, C_{dl}, was constant at 18.8 mF cm^{-2} ± 1 mF cm^{-2} throughout the experiment.

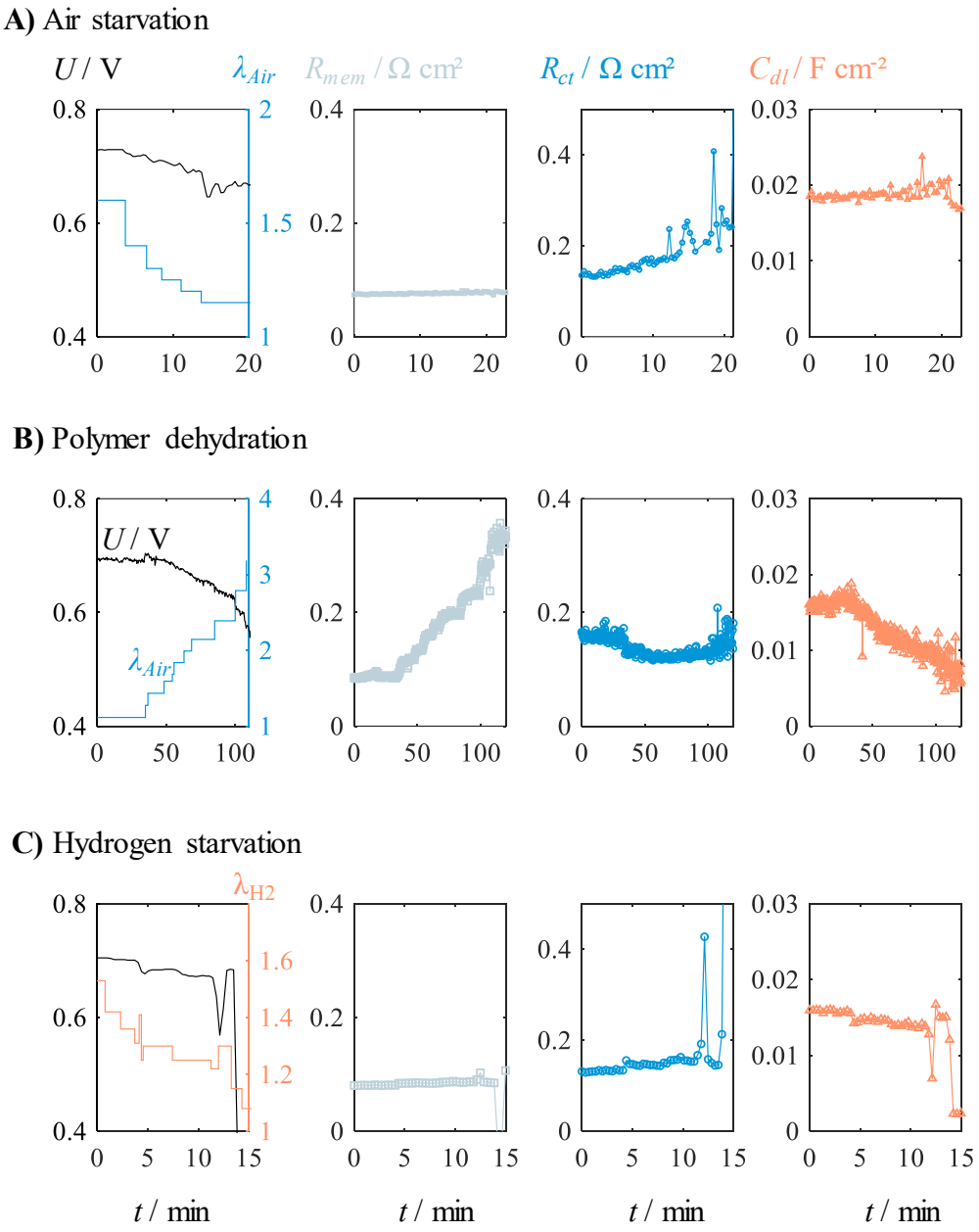

Figure 4.12. Real-time impedance monitoring of an automotive size fuel cell during **A)** air starvation, **B)** polymer dehydration, and **C)** hydrogen starvation. The experimental procedure is described in chapter 3.3.3 (page 51). MEA materials: MEA #4 in **Table 3.1**. Cell setup: SU #ii in **Table 3.2**. Reprinted with permission from ref. [199].

To dehydrate the polymer of the PEMFC, the air volume flow was increased from stoichiometry of 1.3 to 3.2 at an inlet gas humidification of 11%. For a more detailed description of the test parameters see **Table 3.6** on page 51 (column Polymer dehydration).

The results of this experiment are illustrated in **Figure 4.12 B**. The membrane resistance increased with the airflow and exceeded 0.35 Ω cm². In normal operation (see **Figure 4.11 A**), the membrane resistance was relatively constant at 0.075 Ω cm² ± 0.002 mΩ cm². The charge transfer resistance initially decreased when increasing the air supply, similar to its behavior in **Figure 4.12 A**.[83,222,267] As soon as the membrane resistance exceeded 0.2 Ω cm², the charge transfer resistance began to rise. It is hypothesized that the polymer's dehydration leads to an increased diffusion resistance for oxygen in the catalyst layer. Therefore, the oxygen partial pressure at the catalyst layer drops when increasing the airflow. The double layer capacitance dropped from 16 mF cm^{-2} to 6 mF cm^{-2}.

Further investigations are necessary to explain this behavior. Even though a physical explanation is missing, similar experimental results were found in the literature.[268] Another malfunction is the hydrogen starvation, which was triggered by limiting its stoichiometry from 1.53 to 1.08 (see **Figure 4.12 C**). The membrane resistance stayed constant during this event (0.085 Ω cm² ± 0.004 Ω cm²). Importantly, the charge transfer resistance increased when lowering the hydrogen supply. If R_{ct} should serve as an air starvation indicator one needs to carefully investigate how to exclude hydrogen starvation events. The double layer capacitance dropped during this experiment. This characteristic might enable a distinction between air and hydrogen starvation since the double layer capacitance only dropped during hydrogen starvation and stayed constant during air starvation. So far, there is no physical explanation available as the double layer capacitance is influenced by many parameters in PEMFC systems. A hypothesis of why local hydrogen starvation results in a decrease in cell capacitance will be proposed in chapter 4.3.4.

The EEC parameters measured in normal operation (**Figure 4.11**) and during PEMFC failures (**Figure 4.12**) are compared in **Figure 4.13**. The parameter limits during normal operation for C_{dl} were 0.0174 F cm^{-2} to 0.0259 F cm^{-2}, for R_{mem} 0.0697 Ω cm² to 0.110 Ω cm², and for R_{ct} 0.0477 Ω cm² to 0.154 Ω cm². When limiting the air supply, the charge transfer resistance increased up to 0.283 Ω cm² and is thereby clearly larger than R_{ct} values during normal operation. Hydrogen starvation showed a similar increase in R_{ct}, but the simultaneous drop in C_{dl} to 0.0120 F cm^{-2} allows a clear distinction to cathodic events. A drop in C_{dl} was also triggered in dry supply gas operation (**Figure 4.12 B**). Due to the rise in R_{mem} up to 0.280 Ω cm² and the constant R_{ct} (137.9 mΩ cm² ± 17.1 mΩ cm²) clear

identification of polymer dehydration is possible. The findings agree with the general statement by Kurzweil *et al.* that high capacitances in combination with low resistances mark optimal operating states.[80] It is important to mention that each data point in **Figure 4.13** relies on the RTIM methodology using four measurement frequencies between 120 Hz and 238 Hz. The method presented in this chapter thus offers the possibility of a real-time diagnosis of various faults in PEMFC operation.

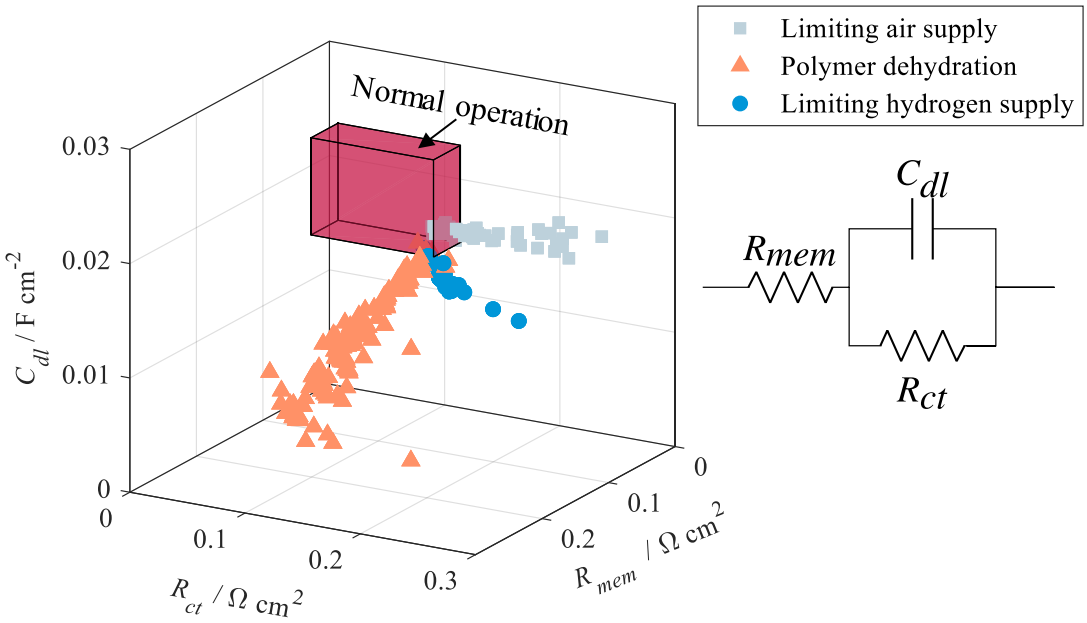

Figure 4.13. Operational failure identification using real-time impedance monitoring. The behavior of the equivalent electric circuit elements (membrane resistance, R_{mem}, charge transfer resistance, R_{ct}, double layer capacitance, C_{dl}) during various PEMFC malfunctions (limiting air supply, increasing air supply, limiting hydrogen supply) according to **Figure 4.11** and **Figure 4.12**. Reprinted with permission from ref. [199].

4.1.5 Chapter Summary

This section described the methodology to monitor automotive size fuel cells, including the EIS measurement and the EIS data analysis algorithm. The presented approach allows identifying PEMFC failures in the range of 50 ms to 100 ms by accurately determining membrane and charge transfer resistance and the cell capacitance. The RTIM methodology has a similar accuracy compared to that of CNLS fitting algorithms and allowed the separation of operational failures like polymer dehydration, air and hydrogen starvation.

4.2 Charge Transfer Resistance during Fuel Cell Operation

Compared to membrane resistance and double layer capacitance, the charge transfer resistance, R_{ct}, of a PEMFC is sensitive to many operating parameters, including temperature, current density, humidification, air supply, and hydrogen supply.[65,84,220,264] The usefulness of R_{ct} is primarily its dependence on oxygen concentration since this can hardly be measured at individual cells within a stack by other means. However, the sensitivity to several operating parameters complicates the evaluation of R_{ct}, which will be considered in more detail in this section. We divide the chapter into the different parts influencing R_{ct}, current density including temperature (chapter 4.2.1) and air supply (chapter 4.2.2). Practical aspects of real-time monitoring of PEMFCs using R_{ct} are explained in chapter 4.2.3.

4.2.1 Impact of Current and Temperature

The influence of temperature and current density on the charge transfer resistance has been considered in the literature both experimentally[65,220] and theoretically.[72,214,228] Impedance spectra in the range of 300 mHz and 1 kHz at current densities between 0.5 A cm^{-2} and 2.0 A cm^{-2} for three different temperatures (65 °C, 75 °C, 85 °C) are illustrated in **Figure 4.14 A** to **D**. The remaining operating parameters were kept constant. Details on cell setup consisting of an MEA with an active area of 285 cm^2 can be found in **Table 3.1** (MEA #4) and **Table 3.2** (SU #ii). As expected, the total cell resistance decreased with increasing current as the charge transfer resistance is inversely related to the current density j, as $R_{ct} \sim b \cdot j^{-1}$, where b is the Tafel slope.[73] The spectra were fitted with a bounded-Randles circuit (see **Figure 2.10 A** on page 27). Since the mass transport arc at low frequencies is not determined with the RTIM method of chapter 4.1, the fits in **Figure 4.14** are illustrated without the Warburg element - even though the fit itself was performed, including the Warburg element. The plot shows that the charge transfer resistance decreases with increasing temperature at any current density, consistent with the trend observed in the literature.[65,220]

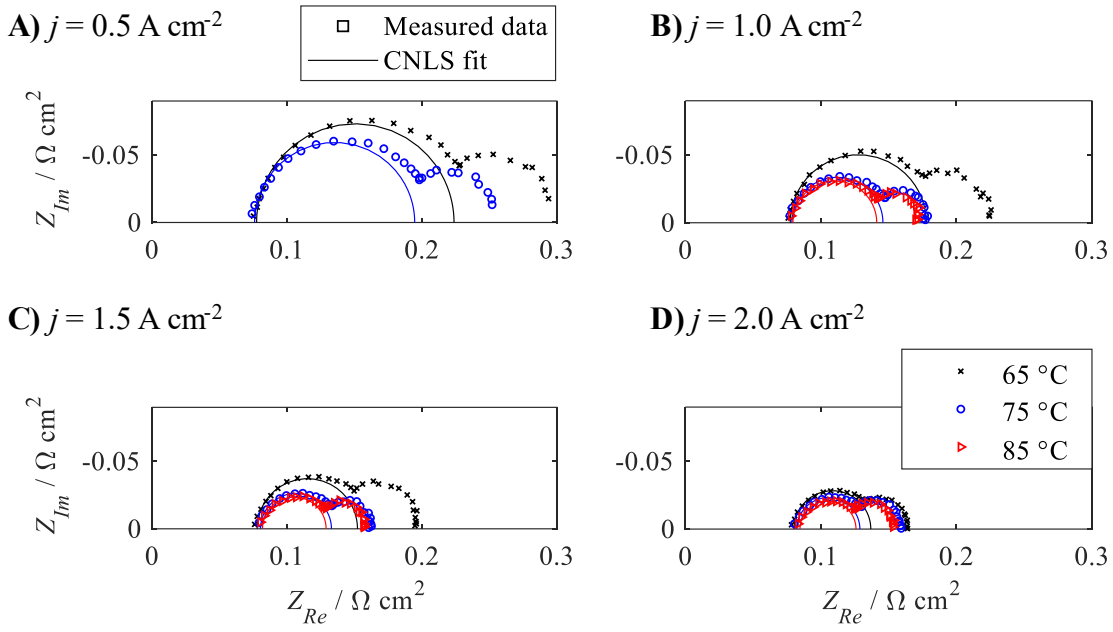

Figure 4.14. Temperature dependence of the impedance of an automotive size PEMFC at different current densities j for **A)** 0.5 A cm^{-1}, **B)** 1.0 A cm^{-1}, **C)** 1.5 A cm^{-1} and **D)** 2.0 A cm^{-1}. The remaining operating parameters are RH = 50%, λ_{Air} = 2.2, λ_{H2} = 1.7, $p_{H2,out}$ = 1.8 bar$_{abs}$ and $p_{Air,out}$ = 2.1 bar$_{abs}$. Measured values are represented by data points, complex non-linear least-squares (CNLS) fitting results by lines.

The results for R_{ct} from the fits in **Figure 4.14** are illustrated in **Figure 4.15 A**, showing that R_{ct}^{-1} is larger at higher temperatures and current densities. The evaluation presented here focuses on the use of R_{ct} for real-time monitoring of PEMFCs. For this reason, the charge transfer resistance based on RTIM is presented in **Figure 4.15 B**. Compared to the CNLS fits, the trends of the DIA results appear more consistent, as the RTIM evaluation calculates the charge transfer resistance exclusively at high frequencies (> 100 Hz), and thus, the mass transport arc has less influence on R_{ct}.

The increase of R_{ct}^{-1} with temperature was not expected from theoretical consdierations, as $R_{ct}^{-1} \sim b^{-1} \sim T^{-1}$. To describe the temperature dependence of the ORR, Song *et al.* uses the equation $R_{ct,ORR} = RT_{cell}\alpha_0^{-1}n^{-1}F^{-1}$, where $\alpha_0 = 0.0017\frac{1}{\mathrm{K}}\cdot T_{cell}$.[228] According to this equation $R_{ct,ORR}$ is independent of temperature, indicating that the ORR kinetics cannot represent the measured data in **Figure 4.15**. Damjankovic published a similar approach,

which contains a temperature-independent β_H and a temperature-dependent β_H symmetry factor ($\beta = \beta_H + \beta_S T_{cell}$),[227] which, represents the measurement results from **Figure 4.15 B** well. However, the fits result in a negative value for β_H = -0.47, which is physically not reasonable. It is consequently not possible to describe the temperature dependence of the kinetic loop in **Figure 4.14** by temperature dependence of the transfer or symmetry factor.

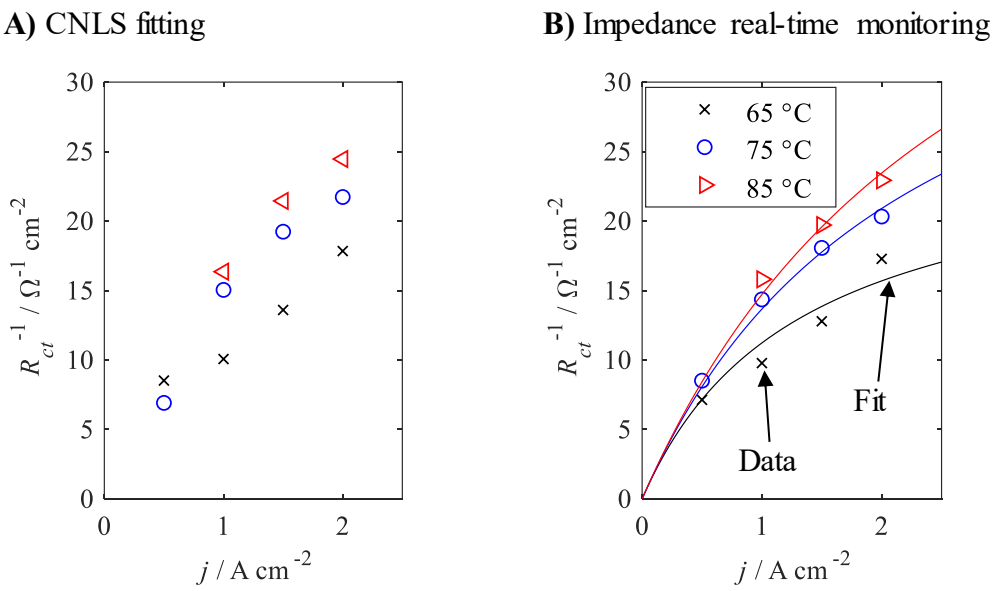

Figure 4.15. Charge transfer resistance, R_{ct}, in dependence on current density, j, at various cell temperatures **A)** using complex non-linear least-squares (CNLS) fitting and **B)** using the real-time impedance monitoring approach between 118 Hz and 286 Hz with five frequencies according to **Figure 4.6**. The fits (lines) in B) are according to **Eq. 12**. The corresponding Nyquist plots are shown in **Figure 4.14**.

Kulikovsky *et al.* show that the ionic conductivity of the polymer, as well as oxygen diffusion in the GDL and catalyst layers, significantly influence the total resistance of the cell even at low current densities.[72] For this reason, we introduce the current-independent resistance, R_{diff}, which summarizes diffusion processes with time constants similar to ORR kinetics. Thus, **Eq. 12** for the charge transfer resistance is obtained.[228]

$$R_{ct}\,[\Omega\ \mathrm{cm}^{-2}] = \frac{\mathrm{R}}{0.0017\mathrm{F}\cdot j} + R_{diff} \qquad \textbf{Eq. 12}$$

In **Eq. 12**, R is the ideal gas constant, and F is the Faraday constant. The formula was used to fit the values in **Figure 4.15 B** (presented as solid lines) and thus quantify R_{diff}. The diffusional resistance decreases with increasing temperature as shown in **Figure 4.16 A**. This trend is consistent with findings in the literature, as the diffusion constants of oxygen as well as the ionic conductivity of the catalyst layer increase with increasing temperature.[72] It cannot be excluded that R_{diff} at 65 °C is influenced by electrode flooding, which is why the graph in **Figure 4.16 A** is specific to the cells used here. With the empirical dependence of R_{diff} on T_{cell}, the measured R_{ct} values can be represented according to **Eq. 12** with an accuracy of $R^2 = 0.97$ (see **Figure 4.16 B**). Provided that the cell temperature is known, we can now analyze air stoichiometry's influence independently of current and temperature.

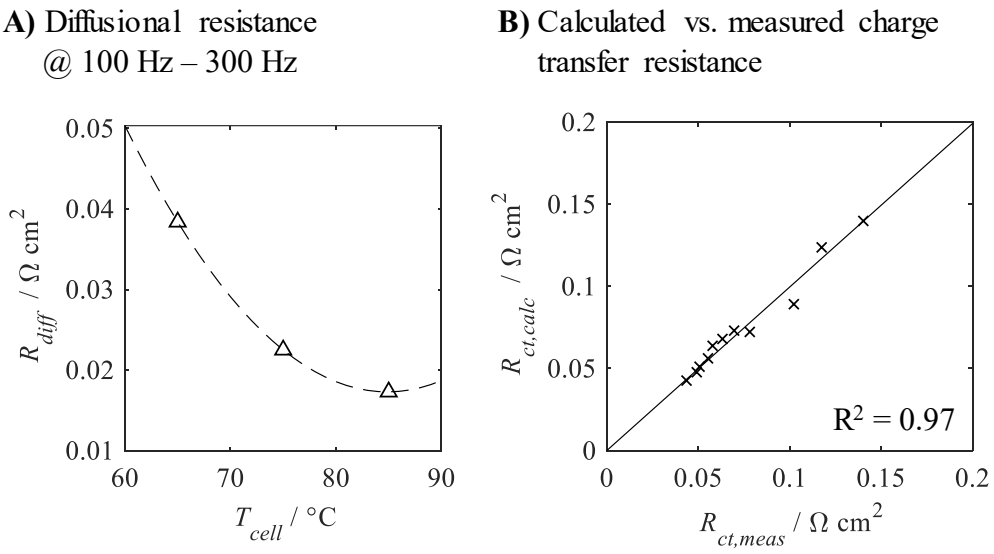

Figure 4.16. A) Temperature dependence of diffusional resistance, R_{diff}, determined by fitting the R_{ct}^{-1} vs. T_{cell} in **Figure 4.15 B** using **Eq. 12**. **B)** Charge transfer resistance based on **Eq. 12** ($R_{ct,calc}$) as a function of the measured value $R_{ct,meas}$.

4.2.2 Impact of Air Stoichiometry

In the literature, in addition to temperature and current density, air stoichiometry affects the behavior of the charge transfer resistance. In the previous analysis from **Figure 4.12**, it was noticed that hydrogen stoichiometry could also have an influence. For simplicity, we assume that humidification plays a minor role and designed an experiment in which the amounts of air and hydrogen are varied at different temperatures and current densities.

Humidification also varied but is not considered further here. To verify the stability of the formula in **Eq. 12** derived from an automotive size PEMFC, the measurements of a laboratory cell with an active area of 43.56 cm^2 are used here. **Figure 4.17** represents the experimental results where the current j was varied between 1 A cm^{-2} and 2 A cm^{-2} (**A**), the air/H_2 stoichiometries λ_{Air}, λ_{H2} between 1.2 and 4 (**B**), and the cell temperature T_{cell} between 65 °C and 85 °C (**C**). The impedance spectra were evaluated using the RTIM method described in detail in chapter 4.1 in the frequency range 118 Hz to 280 Hz. The corresponding value for R_{ct} is shown in **Figure 4.17 D**.

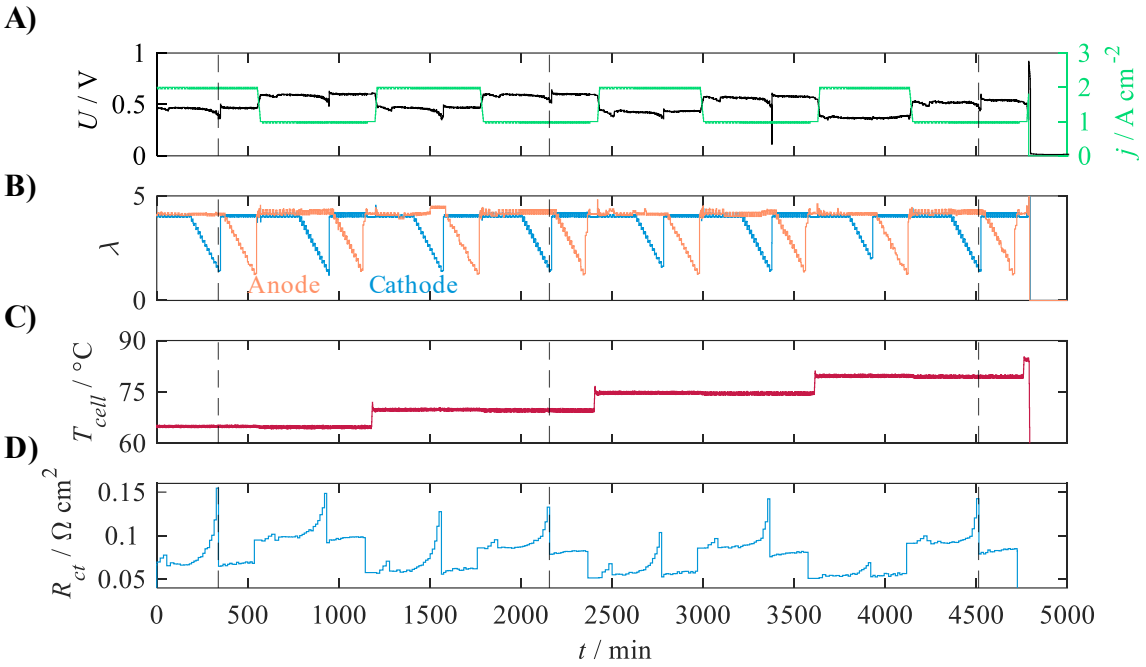

Figure 4.17. Air and hydrogen stoichiometry variations at several current densities and temperatures for a 43.56 cm² cell. Temporal developments of **A)** cell voltage, U, and current density, j, **B)** stoichiometries, λ, of hydrogen (orange) and air (blue), **C)** cell temperature, T_{cell}, and **D)** charge transfer resistance, R_{ct}, based on the real-time impedance monitoring approach of chapter 4.1. Vertical lines indicate selected times of low air supply.

The physical models available in the literature, as **Eq. 11** on page 33, underestimated the impact of λ_{air} on R_{ct}.[72] Since we assume that there is no other influence on R_{ct} except for the reactant supply, the difference between the calculated charge transfer resistance, $R_{ct,calc}$, (ignoring stoichiometry) from equation **Eq. 12** and the measured, $R_{ct,meas}$, are used as an

indicator for the λ_{Air}. This indicator x_{Rct} is calculated in the same way as a measurement error according to **Eq. 13**.

$$x_{Rct} = \frac{R_{ct,meas} - R_{ct,calc}}{R_{ct,meas}} \qquad \textbf{Eq. 13}$$

A second-degree polynomial was used to describe the dependence of R_{diff} on temperature in **Figure 4.16 A**, as $R_{diff}[\Omega\,\mathrm{cm}^2] = \left(5.34 \cdot 10^{-5} \cdot T_{cell}^2[°\mathrm{C}] - 0.00907 \cdot T_{cell} + 0.402\right)$. The indicator x_{Rct} is shown in **Figure 4.18 A** as a function of air stoichiometry. x_{Rct} decreases exponentially with increasing λ_{Air}, with a relatively large root mean square error of 8%. This deviation might occur as we neglect the impact of humidification on R_{ct}, which will be of interest for future research on that topic. Nevertheless, x_{Rct} allows the identification of low air starvations as its sensitivity increases with a lower air supply. The high values of the indicator at an air stoichiometry of four were caused by the variations in the hydrogen supply.

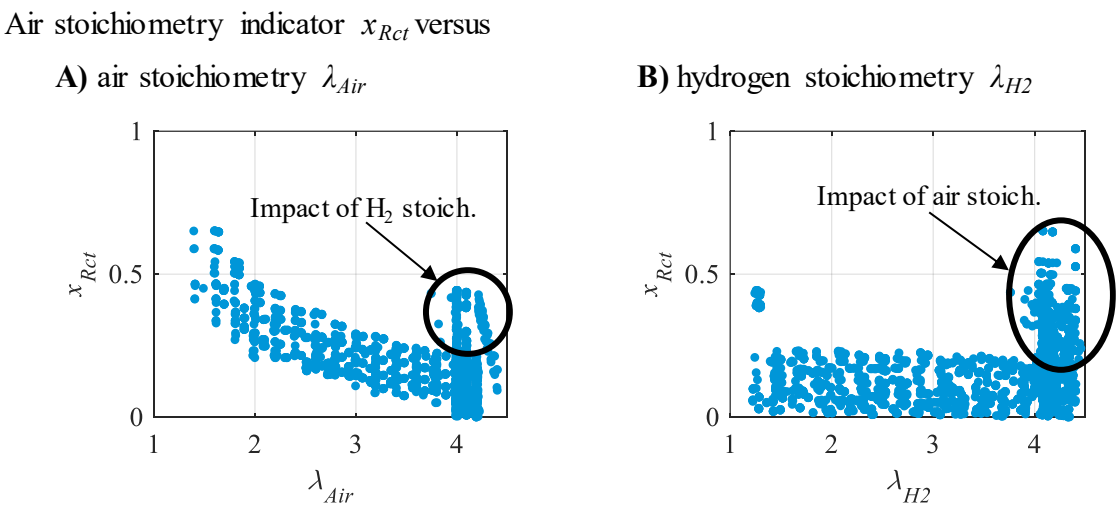

Figure 4.18. Impact of the air stoichiometry indicator x_{Rct} according to **Eq. 13** on **A)** air stoichiometry λ_{Air} and **B)** hydrogen stoichiometry λ_{H2}. Data were taken from **Figure 4.17**.

Figure 4.18 B shows that x_{Rct} is not very sensitive to the λ_{H2}, but when the stoichiometry reaches 1.2, some increased x_{Rct} values can be seen. Local starvation of hydrogen can reduce the available area for the ORR and, therefore, increases the charge transfer resistance at the cathode, as will be analyzed later in chapter 4.4.2. In the following

chapter (4.2.3), practical aspects of R_{ct} will be investigated, including a closer look at the distinction between hydrogen and air stoichiometry.

4.2.3 Practical Aspects of Charge Transfer Resistance Monitoring

Two issues arise in the practical application of R_{ct} to indicate the rate of air supply. (1) The amount of air affects the CDD along with the airflow. R_{ct} does not depend linearly on current density, as its values increase disproportionately at low current densities j ($R_{ct} \sim j^{-1}$). Thus, the charge transfer resistance can be increased when the CDD becomes inhomogeneous, which is a cross-influence on the determination of the air supply. (2) R_{ct} is also influenced by the hydrogen supply. This chapter describes the impact of such cross-influences.

In a fuel cell system, it is unlikely that the CDD of each cell will be measured during operation. To evaluate the air supply, an expected value for R_{ct} is calculated based on **Eq. 12** where the current density must be known. Since no spatially resolved measurements are available, it is obvious to use the average current density here, even if the local currents within the active area of the cell deviate from this. To assess the influence of local currents on the charge transfer resistance, CDDs were simulated using a probability density function for various standard deviations. The cell had 800 segments with different currents, assuming a two-dimensional inhomogeneity of the current density along with the airflow. One simulated CDD at 2.1 A cm^{-2} and a standard deviation of 0.9 is exemplarily illustrated in **Figure 4.19 A**.

In **Figure 4.19 B** the local values of R_{ct} are indicated, which correspond to the CDD in **Figure 4.19 A**. The average of those ($R_{ct,CDD}$) is plotted as a horizontal line (bluish) at 90 mΩ cm^2. In addition, a second (black) line is plotted, which calculates R_{ct} using the mean current density $R_{ct,mean}$ = 63 mΩ cm^2. The charge transfer resistance based on local currents is ~45% higher than $R_{ct,mean}$. Using the average current density across the fuel cell stack in FCEVs, might lead to falsely detect an air shortage due to poor current density distributions.

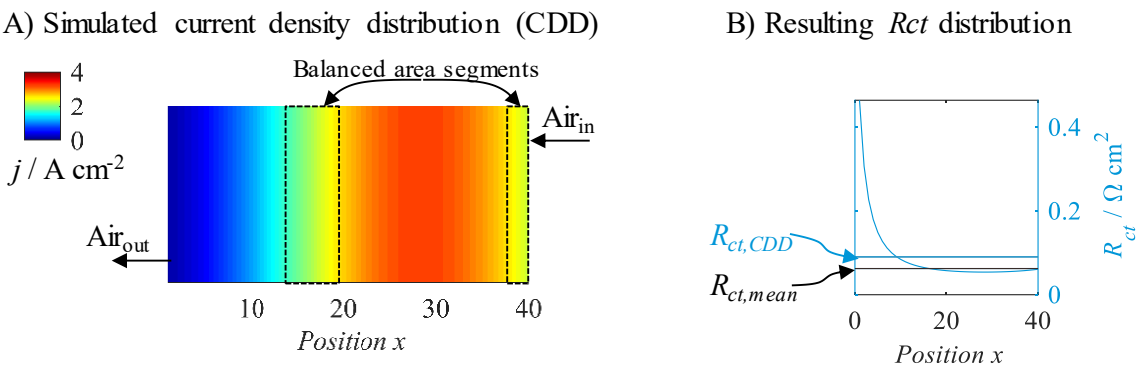

Figure 4.19. A) Simulated current density distribution along with the airflow from inlet Air_{in} to outlet Air_{out} at an average current density j of 2.1 A cm^{-2} and a standard deviation of 0.9. The balanced area for local currents within ± 25% of the average current is indicated as black squares. **B)** Calculated charge transfer resistance, R_{ct}, at the positions, x, according to the local currents in A) using **Eq. 12**. The horizontal lines indicate the average R_{ct} value based on local, $R_{ct,CDD}$, and mean current density, $R_{ct,mean}$.

To quantify the homogeneity of the CDD, we used the balanced area, A_{bal}, instead of the standard deviation. Here A_{bal} is the fraction of the area which has a current of ± 25% of the mean current. The area that corresponds to A_{bal} is indicated as black squares in **Figure 4.19** A and is 22.5% of the total area. **Eq. 12** is used to calculate both the resistance at the mean current density, $R_{ct,mean}$, and the value corrupted by the CDD, $R_{ct,CDD}$. The calculation of $R_{ct,mean}$ based on the average current density is straightforward. For $R_{ct,CDD}$, **Eq. 12** is solved for each segment individually, and then the average was calculated. The error caused by the CDD in the calculation of R_{ct} based on the average current density x_{CDD} is then calculated according to **Eq. 14**.

$$x_{CDD} = \frac{\left(R_{ct,CDD}\text{-}R_{ct,mean}\right)}{R_{ct,mean}} \qquad \textbf{Eq. 14}$$

Figure 4.20 shows the dependence of x_{CDD} on the balanced area at current densities between 0.1 A cm^{-2} and 2.1 A cm^{-2}. As expected, x_{CDD} is zero at a balanced area of 1 (current homogeneously distributed), and increases as the balanced area decreases. The increase is caused by the segments with low current densities where the charge transfer resistance increases disproportionately. The error x_{CDD} is also more pronounced when the

mean current density is lower. This is also due to the disproportionately increasing values of R_{ct} with decreasing current density.

In chapter 4.4.4, the balanced area measurements during operating parameter cycles will be shown. The minimum balanced area was ~0.36 and is plotted in **Figure 4.20** as a vertical line. The x_{CDD} errors are thus overestimated by a maximum of ~15% if the minimum current density during FCEV operation is 0.1 A cm^{-2}. For the detection of low air stoichiometries, according to **Figure 4.18** a deviation of R_{ct} from the ideal value starting at ~50% is crucial. This value is illustrated as a horizontal line in **Figure 4.20**. The error x_{CDD}, which results from the use of the average current density instead of local currents in **Eq. 12**, is thus negligible for the detection of air starvation while it is not negligible for the determination of the exact air stoichiometry.

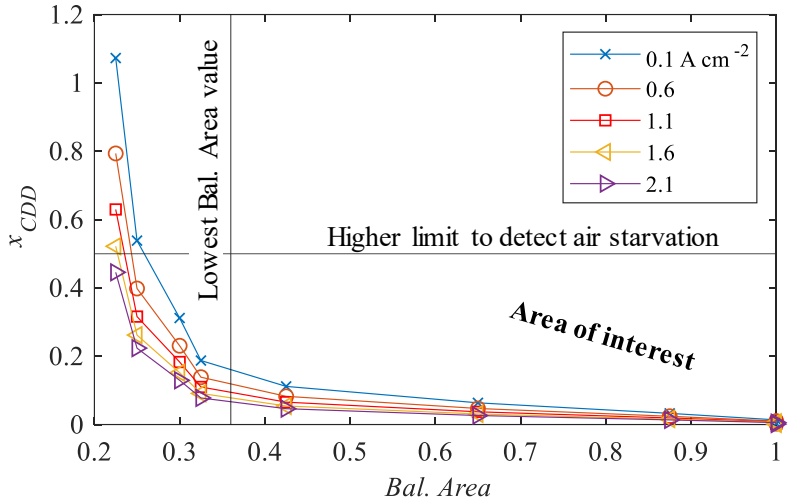

Figure 4.20. Impact of the current density distribution (CDD) on the error between mean and local current based R_{ct} calculation (x_{CDD}, **Eq. 14**) for various mean current densities, j_{mean}. Homogeneity of the CDD is indicated as a balanced area (*Bal. Area*). The horizontal line represents the limit from **Figure 4.18** A to detect low air stoichiometries. The vertical line represents the lowest balanced area value from a parameter variation according to **Figure 4.37**.

The distinction between different failure modes has already been described in chapter 4.1.4, whereas in **Figure 4.21**, the focus is on the distinction of reactant supply. In general, the cell capacitance decreases during hydrogen starvation while it does not occur during air starvation. Therefore, the combination of R_{ct} and C_{cell} allows the distinction between both

reactant supplies. In order not to repeat ourselves, we refer to chapter 4.1.4 for the corresponding description. The behavior of the cell capacitance, C_{cell}, will now be analyzed in more detail in the following chapter (4.3).

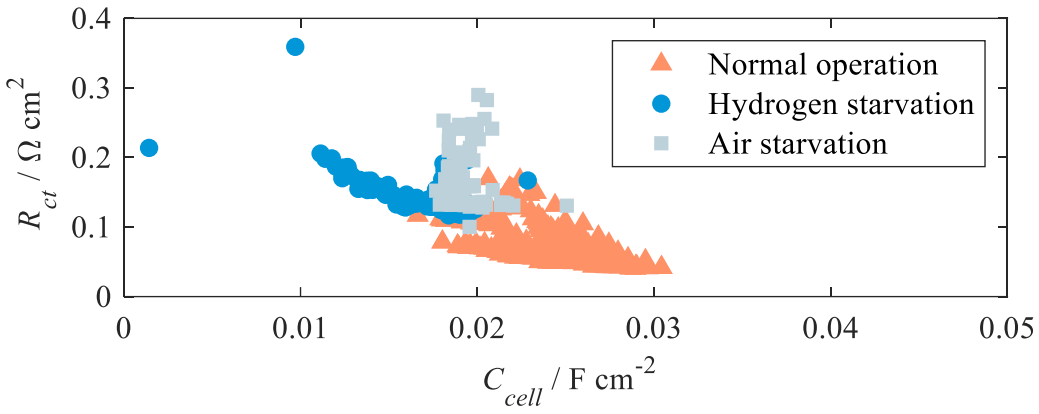

Figure 4.21. Separation of air and hydrogen starvation using electrochemical impedance spectroscopy. Charge transfer resistance, R_{ct}, plotted *versus* cell capacitance, C_{cell}, during normal operation and hydrogen and air starvation. Data correspond to the values already presented in **Figure 4.13**.

4.3 Analysis of the Capacitive Behavior of PEMFCs during Operation

Parts of this chapter were published by the author of this thesis (among others) in the article 'Analysis of the Capacitive Behavior of Polymer Electrolyte Membrane Fuel Cells during Operation'.[126]

The capacitance of a PEMFC is sensitive to operational parameters such as the inflow gas humidification and might identify critical fuel cell states, e.g. hydrogen starvation, as demonstrated in chapter 4.1. Impedance-based diagnostics of PEMFCs in automotive applications are getting more attention,[269,270,271,272] but the physical origin of their capacitive response remains unclear.

In H_2(anode)/N_2(cathode) atmosphere, CV is a common technique to determine the PEMFC capacitive behavior. If a cell is operated with oxygen at the cathode, the capacitance is usually determined by EIS[273,274,275] or current pulse injection.[276,277] Pohl *et al.*[207] showed that the capacitance of Pt(331) single crystals in an aqueous solution depends on the electrode potential and the electrolyte's oxygen content. For PEMFCs, similar studies are not yet available. To close this gap, we investigated the influence of the cell voltage and the oxygen partial pressure in the cathode gas supply on the capacitance of PEMFCs. The experiment was adapted to realistic operating parameters during vehicle operation.[258] The cell voltages were varied between 0.08 V and 1.00 V and the oxygen volume fraction between 0 vol.% and 21 vol.%. Impedance spectra were recorded during these operating points.

4.3.1 Oxygen-depleted Operation

In the following, we analyzed the impedance-based capacitance in stationary PEMFC operation. The experimental conditions were chosen analogous to the CV measurements in **Table 3.3**. Contrary to CV measurements, the cell was operated stationary when recording the EIS. **Figure 4.22 A** shows the Nyquist plots of a PEMFC with an active area of 43.56 cm^2 at different cell voltages U in an oxygen-free atmosphere. The measurement shown in **Figure 4.22** was also performed on another laboratory cell (MEA #1 in **Table 3.1**) and two automotive size cells (MEA #4 in **Table 3.1**), which are listed in **Table 4.1** on page 87. The impedance was smaller at voltages between 0.1 V and 0.4 V

than in the range between 0.4 V and 0.8 V. Since the capacitance is inversely proportional to the impedance, the capacitance was consequently larger at low voltages. The RTIM algorithm from **Figure 4.6** was applied to calculate the cell capacitance, C_{cell}, from the impedance measurements, which is shown in **Figure 4.22 B** as black lines. The capacitance increased as the measurement frequency f decreased. At voltages greater than 0.5 V, the cell capacitance was less than 0.05 F cm^{-2}, increasing towards lower voltages. A CV measurement is included in **Figure 4.22 B**, where the trends at low cell voltages match those of the EIS measurements. At voltages above 0.6 V, the plateau at ~0.25 F cm^{-2} in the CV was not evident in the EIS measurements.

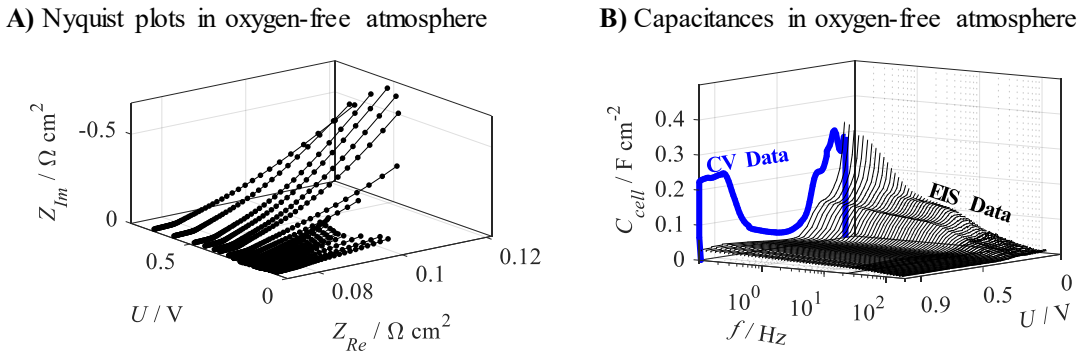

Figure 4.22. A) Nyquist plots of a 43.56 cm² fuel cell (MEA #1 in **Table 3.1**) with hydrogen at the anode and nitrogen at the cathode. **B)** Cell capacitance, C_{cell}, according to A) based on the real-time impedance monitoring approach presented in **Figure 4.6**.

The EIS recorded in oxygen-free atmosphere between 0.08 V and 1.50 V were fitted using a CNLS algorithm based on the EEC in **Figure 4.23 A**. A description of the physical background of the EEC can be found in chapter 2.4 on page 26. To improve the fitting results, we replaced the adsorption capacitance, C_{ads}, with a constant phase element Z_{ads} according to Ragoisha *et al.*,[278] where $Z_{ads} = C_{ads}^{*-1}(j\omega)^{-n}$. A detailed description of the constant phase element is given elsewhere.[174] As the value of C_{ads}^{*} is directly linked to the adsorption capacitance, C_{ads}, it was treated as such. We define the cell capacitance as $C_{cell} = C_{ads}^{*} + C_{dl}$. Since the HUPD has a high rate constant, C_{ads}^{*} is difficult to separate from C_{dl}.[206,207,278] In this study we assume the double layer capacitance to be independent on electrode potential and therefore, C_{ads} was calculated as $C_{ads} = C_{cell}$-C_{dl} by evaluating

C_{dl} as the average capacitance between 0.4 V and 0.5 V. Thus, C_{cell} is directly comparable with C_{ads} and is used in the following for data representation. This chapter focuses on extracting C_{cell} at various voltages. The EIS at 0.15 V in oxygen-free operation is extracted from **Figure 4.22 A** and illustrated in **Figure 4.23 B**, including the CNLS fit. The error of the fit was below 3%, according to the evaluation software.[251]

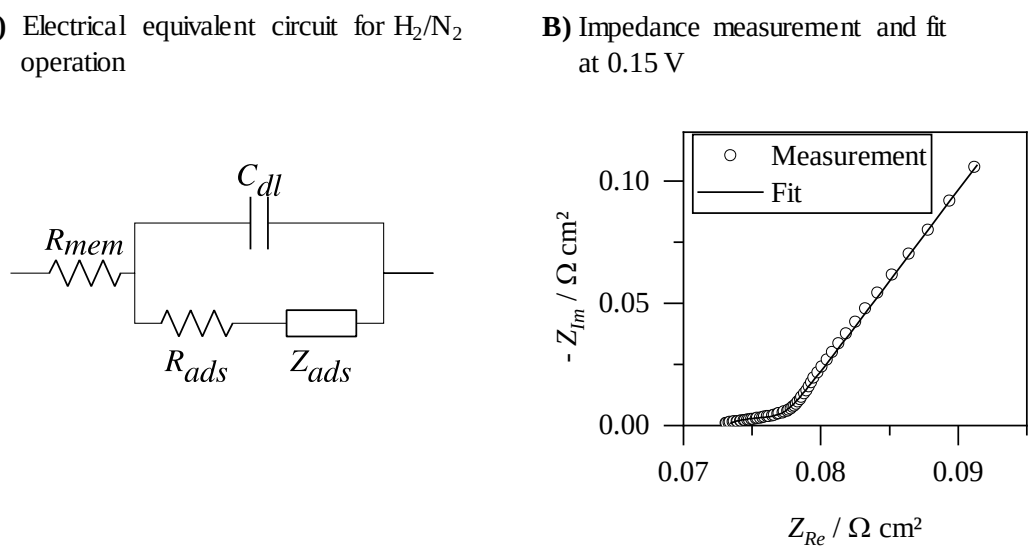

Figure 4.23. PEMFC impedance in an oxygen-free atmosphere. **A)** Equivalent electric circuit for CNLS fitting. **B)** EIS measurement data (dots) and complex non-linear least-squares fit (line) of the data recorded at 0.15 V. The measurements were performed using a lab size MEA (MEA #2 in **Table 3.1**, SU #i in **Table 3.2**). Reprinted with permission from ref. [126].

The cell capacitances between 0.090 V and 1.0 V extracted by CNLS fitting are illustrated in **Figure 4.24 A**. Two areas (0.09 V to 0.4 V and 0.7 V to 1.0 V) showed a voltage-dependent capacitance (marked blue and orange), while the double layer region shows a constant capacitance between 0.4 V and 0.5 V. By integrating C_{cell} over U at the respective voltages, the adsorption charges for HUPD Q_{HUPD} and *OH-film formation on platinum $Q_{Pt\text{-}OH}$ were determined. The blue and orange shaded areas in **Figure 4.24 A** represent the charges due to adsorption. Q_{HUPD} and $Q_{Pt\text{-}OH}$ were normalized to the active area of the cell and are listed in **Table 4.1**. The Q_{HUPD} charges based on the impedance measurements are in the range of 11.9 mC cm^{-2} to 40.2 mC cm^{-2} due to different catalyst loadings. For the analysis of the capacitive behavior of the cells, the determination of the

adsorption charge is sufficient, and, therefore, we do not convert these values to the electrochemically active surface as usual. $Q_{Pt\text{-}OH}$ based on EIS in **Table 4.1** is smaller than the charges due to HUPD. Test item #1 had the largest Pt-OH charge at 8.4 mC cm^{-2}. As described above, CV is another suitable tool to determine Q_{HUPD} and $Q_{Pt\text{-}OH}$. It is important to note that in this case, the potential is continuously swept. The CV of test item #2, according to **Table 4.1**, is illustrated in **Figure 4.24 B**.

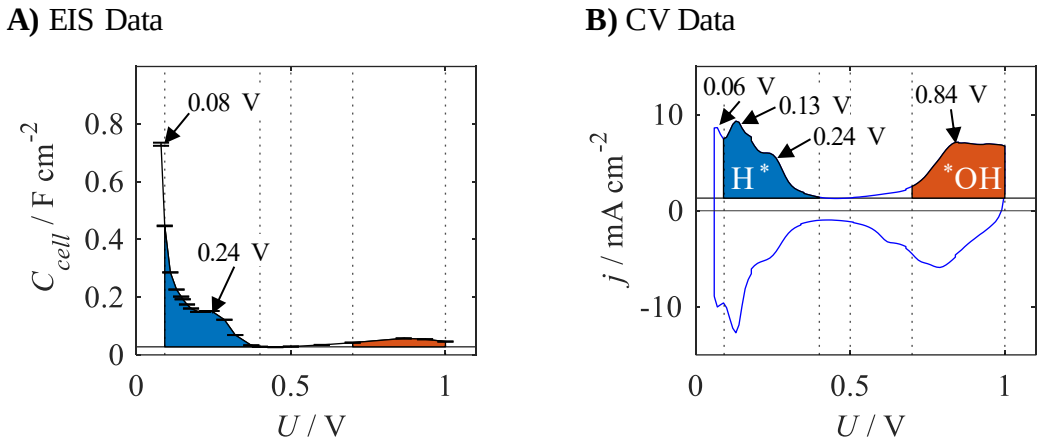

Figure 4.24. The capacitance of a fuel cell with an active area of 43.56 cm². **A)** Cell capacitance, C_{cell}, obtained from stationary EIS measurements at various potentials in oxygen-free atmosphere based on the equivalent electric circuit in **Figure 4.23 A**. **B)** Cyclic voltammogram of a lab size PEMFC (potential sweep rate 30 mV s^{-1}). The operating conditions are listed in **Table 3.3** on page 42. Reprinted with permission from ref. [126].

The symmetry of the peaks at 0.13 V and 0.24 V in the CV (**Figure 4.24 B**) is a sign of the fast and reversible adsorption and desorption of hydrogen. In contrast, the currents between 0.70 V and 1.0 V, which result from the *OH-layer formation on platinum, are not symmetrical.[279] Between 0.40 V and 0.50 V, no adsorption/desorption processes are visible in the diagram in **Figure 4.24 B**, which is why the double layer capacitance was evaluated at these voltages. The peak at 60 mV occurs due to the HER.[248,280] The area-specific charges of the HUPD and the *OH-formation based on CV measurements are listed in **Table 4.1** along with the EIS results.

Table 4.1. Differential charges of the HUPD Q_{HUPD} (left) and Pt-OH $Q_{Pt\text{-}OH}$ (right) measured using cyclic voltammetry (CV) and electrochemical impedance spectroscopy (EIS) in an oxygen-free atmosphere for four different cell setups. Test IDs #1 and #2 had an active area of 43.56 cm² (see MEA #1 in **Table 3.1**). Test IDs #3 and #4 had an active area of 285 cm² (see MEA #4 in **Table 3.1**).

Test item	Active Area [cm²]	Q_{HUPD} [mC cm^{-2}]		$Q_{Pt\text{-}OH}$ [mC cm^{-2}]	
		CV	EIS	CV	EIS
#1	43.56	40.3	34.7	48.9	8.4
#2	43.56	19.4	17.5	18.5	-
#3	285	36.3	32.1	46.6	5.8
#4	285	11.9	10.2	22.6	2.9

A comparison of the CV and the EIS based PEMFC analysis (see **Figure 4.24** and **Table 4.1**) is performed in the following. The EIS and CV results show larger Q_{HUPD} and $Q_{Pt\text{-}OH}$ values for test items #1 and #3 compared to those of #2 and #4. The HUPD charges are similar for both methods, whereas the Q_{HUPD} values determined by impedance measurements were about 12% smaller, as evident from **Table 4.1**. The peak at ~240 mV is visible in the EIS (**Figure 4.24 A**) and CV (**Figure 4.24 B**) data. However, the peak in the CV at 130 mV was not visible in the EIS measurement. It is assumed that the voltage amplitude of the EIS measurement of ± 20 mV triggers the HER. This takes place at 90 mV[280] and is therefore already visible in the impedance analysis below 110 mV. The HER caused an increase in current at voltages below 110 mV, leading to cell capacitances up to ~0.75 F cm^{-2}.

Like the Q_{HUPD} calculation, the charges based on *OH-layer formation $Q_{Pt\text{-}OH}$ were determined. According to **Table 4.1**, $Q_{Pt\text{-}OH}$ evaluated by EIS was about 85% smaller compared to the CV results. The irreversible platinum oxide formation led to smaller results in the stationary EIS measurements. At potentials higher than ~650 mV, oxygen passivates the platinum surface.[279] Thus, an oxide layer had already formed before the impedance was measured. The associated adsorption/desorption currents were not recorded as these processes are slow compared to the excitation frequencies of the EIS. The amplitude of

± 20 mV only slightly changed the catalyst surface, which led to reduced $Q_{Pt\text{-}OH}$ values. Similar effects were found in the literature.[207]

4.3.2 Operation under O_2-containing Atmosphere

EIS can measure adsorption and double layer impedances while the fuel cell is in operation, and thus the ORR takes place. The corresponding Nyquist plots between 0.08 V and 0.80 V are illustrated in **Figure 4.25 A**. The real part of the impedance, Z_{Re}, showed negative values at voltages below 0.3 V and frequencies below 1 Hz, which is a typical phenomenon when operating PEMFCs with low oxygen concentrations. The negative resistances are caused by voltage perturbations due to oxygen concentration oscillations.[240] The capacitances based on the RTIM algorithm (see **Figure 4.6** on page 60) are illustrated in **Figure 4.25 B**. In the voltage range of 0 V to 0.4 V, the capacitances in the EIS data are increased, whereby it seems to be suppressed compared to the CV measurement in oxygen-free atmosphere. Between 0.7 V and 1.0 V there is no capacitance peak in the EIS data, similar to the measurements in oxygen-free atmosphere in **Figure 4.22 B**.

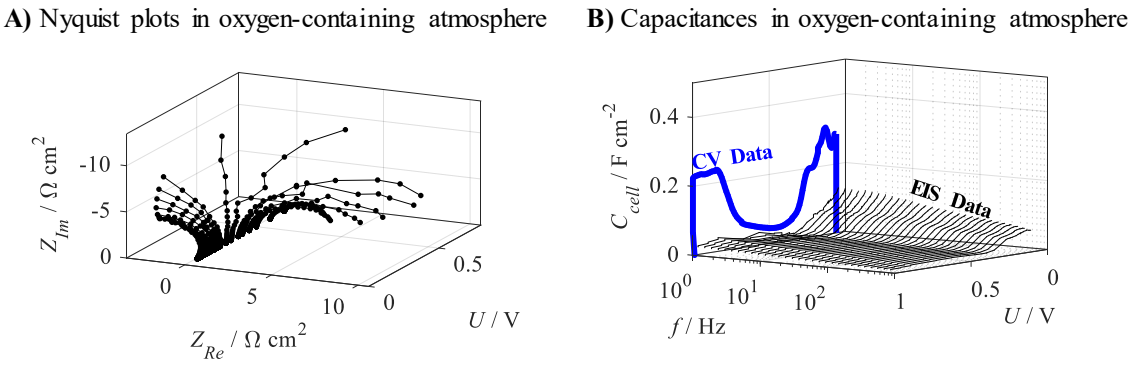

Figure 4.25. **A)** Nyquist plots of a 43.56 cm² fuel cell (MEA #1 in **Table 3.1**) with hydrogen at the anode and 7.5 vol.% oxygen at the cathode. **B)** Cell capacitance, C_{cell}, according to A) based on the real-time impedance monitoring approach presented in **Figure 4.6**.

The impedance of the ORR is described by a bounded Randles EEC, which is shown in **Figure 4.26 A**. A finite-length Warburg element, W_{short}, was used to describe diffusional losses.[205,281,282] The diameter of the semicircle at about 50 Hz is often described as kinetic or charge transfer resistance, R_{ct}, in PEMFCs.[65,220,224] A detailed description of R_{ct} can be

found in chapter 4.2. Since this chapter analyzes the capacitive behavior of the cell, R_{ct} and W_{short} were used to fit the impedance data but no further analysis will be presented. The EEC in **Figure 4.26 B** achieved an accuracy of ~5%[251] using CNLS fitting.

A) Electrical equivalent circuit for H_2/Air operation

B) Impedance measurement and fit at 0.37 V

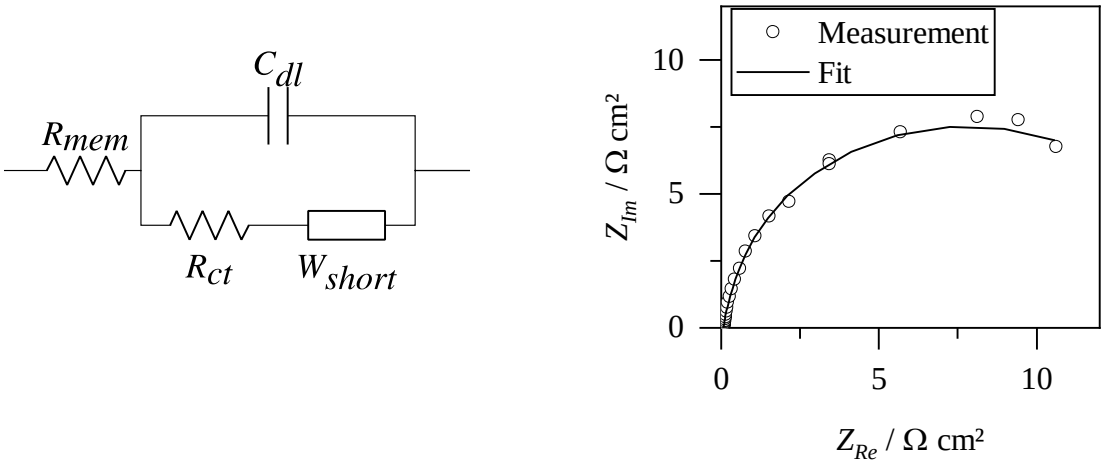

Figure 4.26. PEMFC impedance in oxygen-containing atmosphere. **A)** Bounded Randles equivalent electric circuit for CNLS fitting. **B)** EIS measurement data (dots) and fit (line) of the impedance data recorded at 0.37 V. The measurements were performed using a lab size MEA (MEA #2 in **Table 3.1**, SU #i in **Table 3.2**). Reprinted with permission from ref. [126].

Figure 4.27 A shows the dependence of the cell capacitance between 0.09 V and 1.50 V on oxygen partial pressure. It can be seen that the oxygen partial pressure has a marginal influence on $Q_{Pt\text{-}OH}$ (between 0.6 and 1.5 V). This effect has already been described in the literature.[206] Therefore, in the following, we consider the sensitivity of Q_{HUPD} to the oxygen content. The EEC diagrams for oxygen-free (**Figure 4.23 A**) and oxygen-saturated (**Figure 4.26 A**) operation differ. Since the EECs for the oxygen-free and oxygen-containing operation were different, this could result in an unwanted bias when comparing capacitances. To avoid such an unwanted bias, the capacitances were not only determined by CNLS fitting but also by the RTIM approach as already presented in **Figure 4.22 B** and **Figure 4.25 B**. The cell capacitances, C_{cell}, for different oxygen contents in the air inflow are illustrated in **Figure 4.27 A** as a function of voltage. The higher the volumetric share of oxygen at the cathode air inlet, the lower Q_{HUPD} got. The DIA showed the same trend

over the whole frequency range between 0.3 Hz and 500 Hz, which is illustrated by the example of the calculations at 1 Hz in **Figure 4.27 B**.

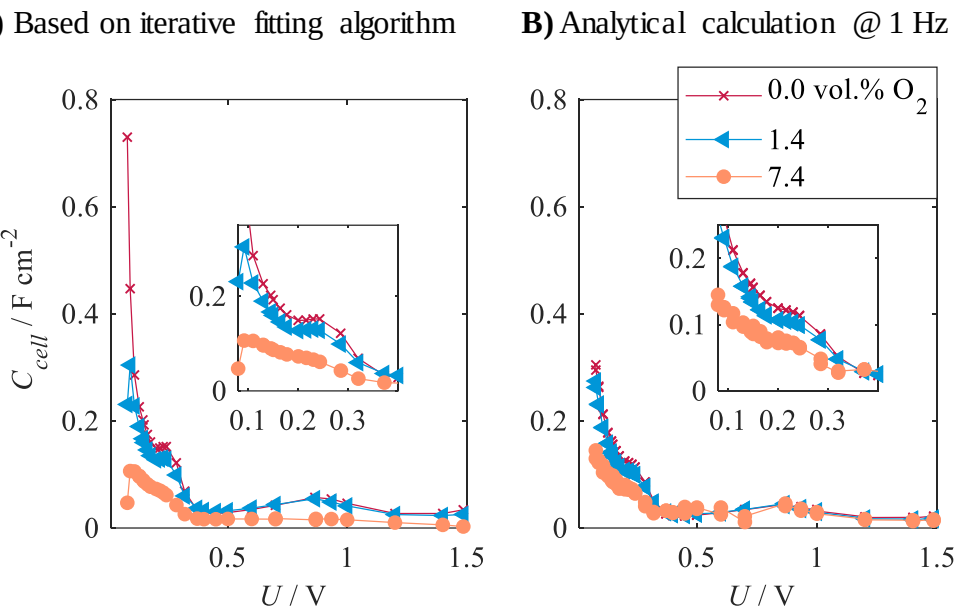

Figure 4.27. Differential cell capacitances, C_{cell}, based on impedance measurements as a function of cell voltage on a lab size MEA (MEA #2 in **Table 3.1**, SU #i in **Table 3.2**). **A)** Data evaluation using complex non-linear least-squares fitting. **B)** C_{cell} based on real-time impedance monitoring approach at 1 Hz (approach presented in **Figure 4.6** on page 60). Reprinted with permission from ref. [126].

It is essential to mention that the peak potentials of the C_{cell} in **Figure 4.27** do not depend on oxygen content. This implies that the HUPD is still responsible for the occurrence of the adsorption charge, but the quantity of the charge becomes smaller. In rotating disc electrode measurements on single crystals, the Q_{HUPD} was only slightly depressed in oxygen saturated operation,[207,206] whereas in normal PEMFC operation, Q_{HUPD} is about zero. Since a major difference between the rotating disc electrode and PEMFC setup is the active area, it was assumed that local effects caused the different results. This will be discussed in the following chapter.

4.3.3 Local Oxygen Starvation

This chapter compares the CDD (experimental see 3.2.3) of PEMFCs with their capacitances at different oxygen partial pressures on the cathode. The Q_{HUPD} results in

oxygen-free operation were larger than the Q_{HUPD} results with oxygen, according to **Figure 4.27**. Therefore, we normalized all Q_{HUPD} values to the corresponding value in oxygen-free operation and referred to this as q_{HUPD} in the following. The values used for the normalization can be found in **Table 4.1** on page 87 in the column Q_{HUPD} EIS. The Q_{HUPD} differences in H_2/N_2 operation occurred probably due to the varying catalyst loadings of the cells. As described in chapter 4.3.2, q_{HUPD} dropped with increasing oxygen volume flow and reached ~0 at volume fractions greater than ~15 vol.% as shown in **Figure 4.28 A** (blue dots). At higher oxygen contents, the cell capacitance was purely described by characteristics of the double layer. The q_{HUPD} values were fitted using an exponential decay (dotted line). Thus, the influence of oxygen on cell capacitance at voltages below 0.4 V in PEMFCs is at least qualitatively independent of cell size and materials. Quantitative differences might result from properties of the flow field, MEA materials, active area, ECSA, etc., which needs to be further evaluated.

Figure 4.28 B shows the measured CDD at an oxygen volume fraction of 6.9 vol.%. The current density close to the air inlet (Air_{in}) is ~1.1 A cm^{-2} and drops to 0.007 A cm^{-2} due to the decreasing partial pressure of oxygen towards the air outlet. In the experiment, the cell was operated potentiostatically with certain oxygen contents between 0 vol.% and ~21 vol.%. Thus, there was no direct influence on the ratio of oxygen volume flow and electric current (air stoichiometry). This ratio significantly influences the gradient of the oxygen partial pressure from cathode inlet to outlet. The larger the air volume flow, the more homogeneous the CDD is due to the greater availability of oxygen at the cathode outlet.[283] The low currents in **Figure 4.28 B** close to the cathode can thus be explained by a low oxygen partial pressure in those locations.

If, on the contrary, the cell is operated oxygen-free (**Figure 4.28 D**), the measured currents over the entire active area are negative - i.e., the other way round as during the ORR in PEMFC operation. The measured currents are called parasitic currents because they are caused by hydrogen crossover and electrical short circuits across the polymer membrane.[91,284,285] They also occur in normal PEMFC operation, but since the current densities of the ORR are usually much higher than the parasitic currents, the latter are hardly noticeable in PEMFC operation. A more detailed description of the theoretical background can be found in chapter 2.2.3. The average current density in oxygen-free

operation was -3.6 mA cm^{-2} (**Figure 4.28 D**), which is a typical value for hydrogen crossover in PEMFCs.[285]

The cell was additionally operated with 2.3 vol.% oxygen to characterize the range between "100%" negative and "100%" positive currents. In this case, two separate regions formed within the active area (**Figure 4.28 C**). The currents in the area near the air inflow (Air_{in}) were positive because the ORR is active here. In the area near the air outflow, the oxygen is already so depleted that hydrogen crossover and short circuits are dominant here and thus negative currents dominate. The proportion of negative currents within the active area as a function of the oxygen volume fraction is indicated in **Figure 4.28 A** (black squares); this curve is like that of q_{HUPD}.

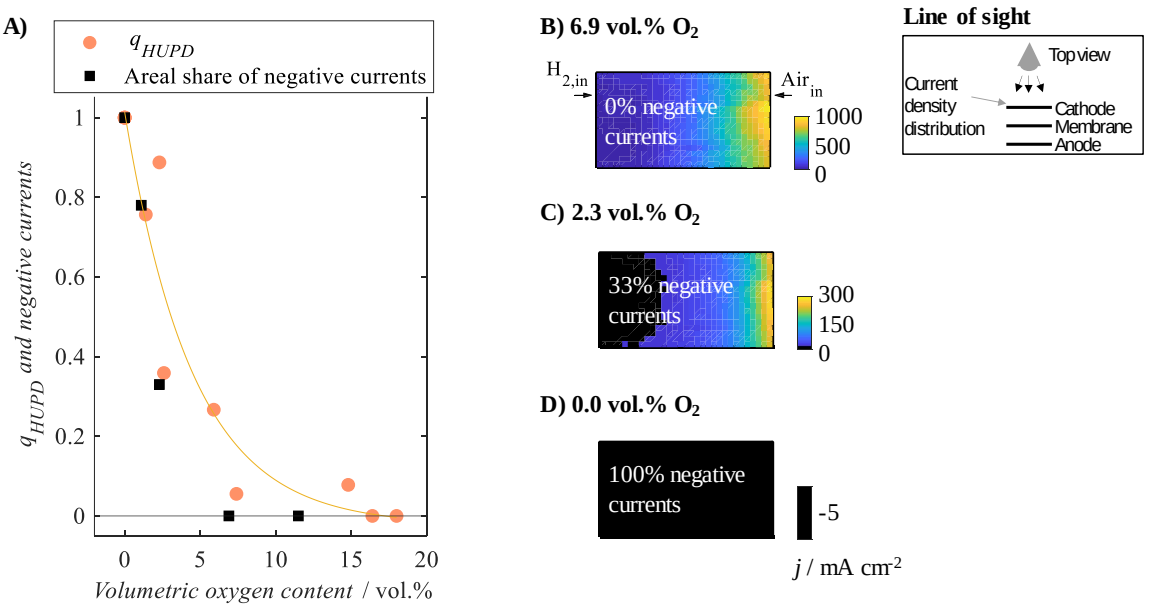

Figure 4.28. A) Normalized adsorption charge q_{HUPD} and share of negative current within the active area *versus* volumetric oxygen volume content at the cathode fitted with exponential decay. **B)** Current density distribution map at 0.24 V and oxygen content of 6.9 vol.% at the cathode. **C)** 2.3 vol.%, and **D)** 0.0 vol.%. Reprinted with permission from ref. [126].

In the following, the relationship between CDD and the HUPD adsorption charge is analyzed in more detail. During oxygen-free operation (0 vol.% O_2, **Figure 4.28 D**) the cell reached the maximum adsorption charge while the currents are negative over the entire area. The HUPD reaction takes place between 0.09 V and 0.40 V, according to **Eq. 15**.[286]

$$H^+ \leftrightarrow H^* \qquad \textbf{Eq. 15}$$

In that case, the differential adsorption capacitance, $C_{ads} = dq/d\Phi$, reaches its maximum because the charge of the catalyst surface q varies with the excitation voltage of the EIS measurement Φ. This adsorption reaction takes place within the entire active area. In contrast, while the ORR was active, the impedance-based adsorption charge was zero. In this case, the following reaction takes place:[287]

$$O_2 \rightarrow {}^*OOH \rightarrow {}^*O \rightarrow {}^*OH \leftrightarrow H_2O \qquad \textbf{Eq. 16}$$

While in the HUPD, the adsorption/desorption of H^+ causes q_{HUPD}, here it is *OH-ions that react with H^+ to water. The thermodynamic equilibrium is about 1.2 V. We assume that due to the high overvoltage at cell voltages below 0.40 V, the *OH-adsorption is very fast and therefore cannot be detected by the EIS measurement up to 1 kHz. Thus, the adsorption capacitance, C_{ads}, is zero in areas where the ORR is active and reaches maximum values in areas where the HUPD takes place. The quasi-exponential decrease of the q_{HUPD} with increasing oxygen volume fraction thus describes the reduction of the areas in which the ORR is active if the cell voltage is between 0.09 V and 0.40 V.

4.3.4 Practical Aspects of PEMFC Capacitance Monitoring

This chapter describes the behavior of the cell capacitance, C_{cell}, in different operating states of PEMFCs, distinguished between normal operation and air and hydrogen undersupply. We will restrict this part exclusively to the capacitive response of the cell. As described in chapter 4.3.3, the fuel cell capacitance is influenced by adsorption and double layer effects. Since resistors are ignored here, the EEC of the cathode results as a parallel connection of adsorption, $C_{c,ads}$, and double layer capacitance, $C_{c,dl}$.[205,206,207,263] In series to this, the anode is connected with the same behavior (see **Figure 4.29 A**). The corresponding equation to calculate C_{cell} is illustrated on the right. In automotive operation, the potential of the anode is at about zero volts[141,288] and therefore, the adsorption charge due to the HUPD leads to high $C_{a,ads}$ values analog to the mechanisms described in chapter 4.3.3. In that case, the pseudo-capacitance due to adsorption at the anode is larger than $C_{c,dl}$ ($C_{a,ads} >> C_{c,dl}$) , and, therefore, the anode can be neglected during normal PEMFC operation. Additionally, adsorption processes of the ORR are not detected by EIS below 1 kHz (see chapter 4.3.2) resulting to $C_{c,ads} = 0$. Hence, C_{cell} in normal PEMFC

operation is equal to the double layer capacitance of the cathode $C_{c,dl}$ as illustrated in **Figure 4.29 B**. This simplifies the analysis of the C_{cell} during normal operation since we can focus on understanding the dependence of the cathode double layer on operational conditions by neglecting other effects.

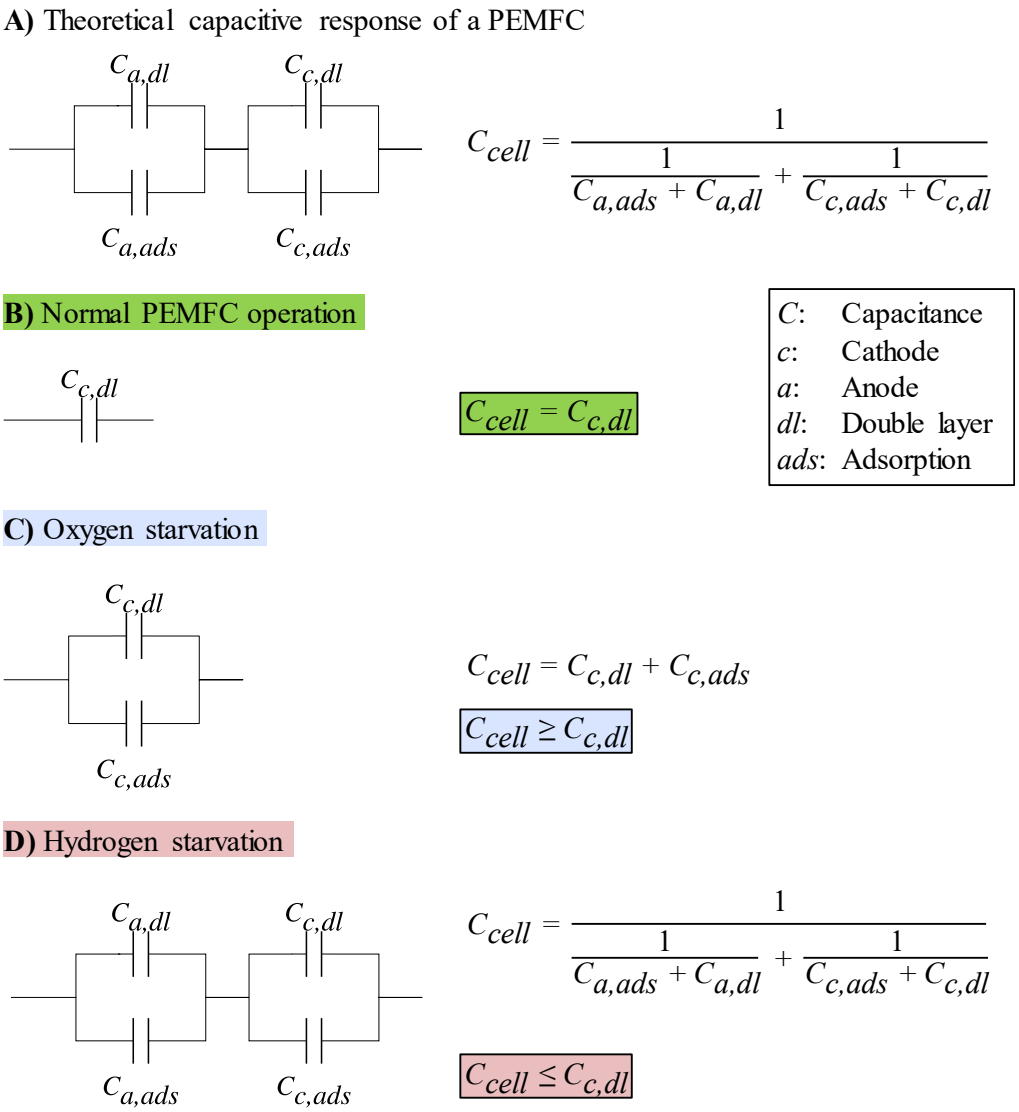

Figure 4.29. Relevant impedance-based capacitive response of PEMFCs **A)** in theory, **B)** during automotive PEMFC operation, **C)** during oxygen starvation of the cathode, and **D)** during hydrogen starvation at the anode. The subscripts are *a* for the anode, *c* for the cathode, *ads* for adsorption, and *dl* for the double layer.

$C_{c,dl}$ during normal operation is insensitive to current density and operational temperature. The sensitivity analysis in chapter 3.3.2 has shown that humidification of the cell

significantly influences its capacitance during normal operation. Similar results were presented by Sabawa *et al.*[275] It was hypothesized that swelling and shrinking of the membrane influences the contact between the electrical and ionic phase within the active area. Furthermore, the ion concentration within the polymer changes depending on its humidification. In **Figure 4.30**, the dependence of C_{cell} on R_{mem} was measured using an automotive size PEMFC. A linear relationship was found, which shows that the capacitance decreases with increasing internal resistance of the cell. This is due to the decrease in the effective active area and the ion concentration in the polymer. If the state of a PEMFC cell is to be understood using EIS, it is recommended to determine the relationship $C_{cell} = f(R_{mem})$ empirically for the respective cell type. Currently, there are no comprehensive physical models to describe this relationship. However, the EIS measurement allows the correction of C_{cell} using R_{mem}. Since the RTIM approach (see section 4.1) determines C_{cell} and R_{mem} simultaneously and in real-time, the humidification dependence of C_{cell} can be corrected without further measurements and modeling.

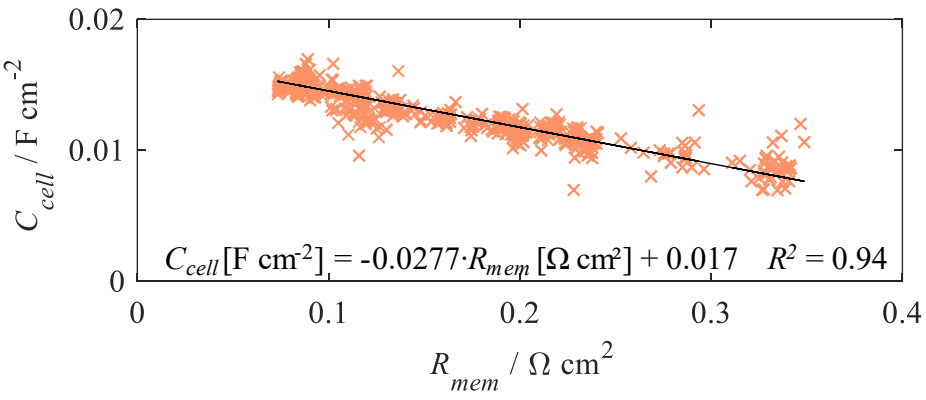

Figure 4.30. Cell capacitance, C_{cell}, *versus* membrane resistance, R_{mem}, during polymer dehydration of an automotive size single cell including a linear fit and the corresponding equation. The experimental details are given in **Table 3.6** on page 51 (polymer dehydration).

The effect of oxygen shortage on the cell capacitance was in detail described in chapter 4.3.2. While in normal operation, only double layer effects of the cathode were relevant, HUPD adsorption effects are now also relevant due to the dominant hydrogen

crossover in some locations on the active area. This results in the EEC in **Figure 4.29 C** leading to an increased overall capacitance during air starvation. Since the HUPD takes place between 0.090 V and 0.4 V the cell capacitance can only detect oxygen starvation if the cell voltage drops below 0.4 V. Since the charge transfer resistance is sensitive to the airflow rate, it is useful to use it also for the detection of oxygen starvation. The problem here is that the charge transfer resistance (or "left" semicircle in the Nyquist plot) depends on many operating parameters, and there are many different findings regarding its physical interpretation.[73,191,289] This was discussed in chapter 4.2.

In chapter 4.1.4, it was shown that the cell capacitance collapses during hydrogen starvation. During this depletion, the electrode potential of the anode increases from ~0 mV to ~400 mV.[57,288,290] The HUPD also takes place between 0 mV and 400 mV, and the associated pseudocapacitance collapses as soon as potentials above ~250 mV are reached (see CV in **Figure 4.24 B**). The anode was neglected in normal PEMFC operation because its adsorption capacitance was large compared to double layer capacitance. It is hypothesized that due to the increasing anode potential, this is no longer the case when hydrogen starvation occurs, and therefore, the full theoretical equivalent circuit diagram must be considered here. This leads to a reduction of C_{cell} compared to the normal operation of the PEMFC. In the sensitivity analyses and the fault case considerations, only the dehydration of the polymer and the hydrogen undersupply led to a drop of C_{cell} below the C_{dl} value extracted from CVs. If the influence of polymer humidification is corrected *via* membrane resistance as described before, real-time diagnosis of hydrogen starvation in the voltage range between 0 V and 1 V during PEMFC operation is thus possible.

The capacitive response of the PEMFC during normal operation is based purely on the double layer of the cathode, whereas adsorption capacitances of anode and cathode become additionally relevant during starvation. Therefore, if it is possible to calculate an expected value for $C_{c,dl}$ during vehicle operation, it is possible to diagnose different failure cases.

4.3.5 Chapter Summary

This chapter investigated the influence of operating conditions on the capacitive behavior of PEMFCs. In oxygen-free operation, EIS and CV measurements showed similar results for the HUPD adsorption charge. This adsorption charge is suppressed in oxygen-saturated operation, probably because *OH-adsorption is fast and cannot be detected with measuring

frequencies below 1 kHz. However, this artifact allows the detection of oxygen depletion during PEMFC operation if the cell voltage is below 0.4 V. Since the anode potential increases during hydrogen starvation, which leads to a collapse of the anodic adsorption capacitance, it can be detected by a collapse of the total cell capacitance. A summary of this phenomenon is given in **Figure 4.31**. For the exact identification of a failure, knowledge of the influence of membrane humidification is necessary. The capacitance of the cell reacts very specifically to a few failure scenarios and can also be monitored in real-time. Therefore, it is a suitable parameter for state-of-operation determination in automotive PEMFC stacks.

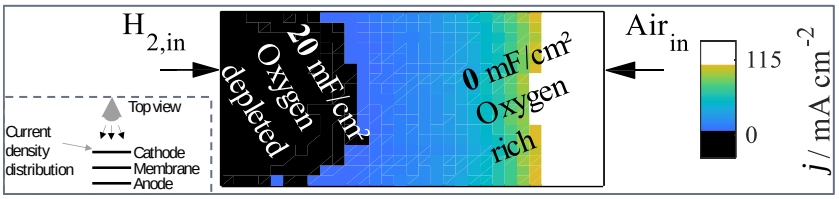

Figure 4.31. The adsorption capacitance of automotive fuel cells is very sensitive to the oxygen content at cell voltages below 0.40 V. This enables impedance-based real-time monitoring of local and global air starvation during vehicle operation. Reproduced with permission from ref. [126].

4.4 Local Degradation Effects under Automotive Operating Conditions

Parts of this chapter were published by the author of this thesis (among others) in the article 'Local degradation effects in automotive size membrane electrode assemblies under realistic operating conditions'.[258]

In the previous chapters, it was described how malfunctions of PEMFCs can be detected with impedance spectroscopy. The following section analyzes the influence of various operating parameters on cell performance and degradation mechanisms. For this purpose, automotive size single cells (288 cm², MEA #5 in **Table 3.1** on page 36) according to the setup SU #ii in **Table 3.2** were operated on a test bench under FCEV conditions, which were extracted from customer driving profiles. The cell temperature (up to 90 °C), gas pressures (up to 175 kPa_{abs}), current density (up to 2.0 A cm^{-2}) and cathode stoichiometry (down to 1.4) were varied. The ex-situ results and the performance degradation of the MEA were analyzed with respect to CDD measurements and the operating conditions. This chapter gives an outlook on the current status of fuel cell degradation during automotive operation, which could be improved with impedance-based real-time diagnostic tools.

4.4.1 Building a Realistic Drive Cycle

On-road data were analyzed to establish typical customer load profiles, which were translated into fuel cell system's operating parameters using a simulation tool. Conditions for a cell in the middle of the stack were extracted and seven specific parameter sets were identified. These sets have different (1) current densities j, (2) coolant temperatures T, (3) anode and cathode inlet gas humidification RH_{inlet}, (4) anode and cathode stoichiometries λ, and (5) anode and cathode outlet gas pressures p. The developed cycle is shown in **Figure 4.32**.

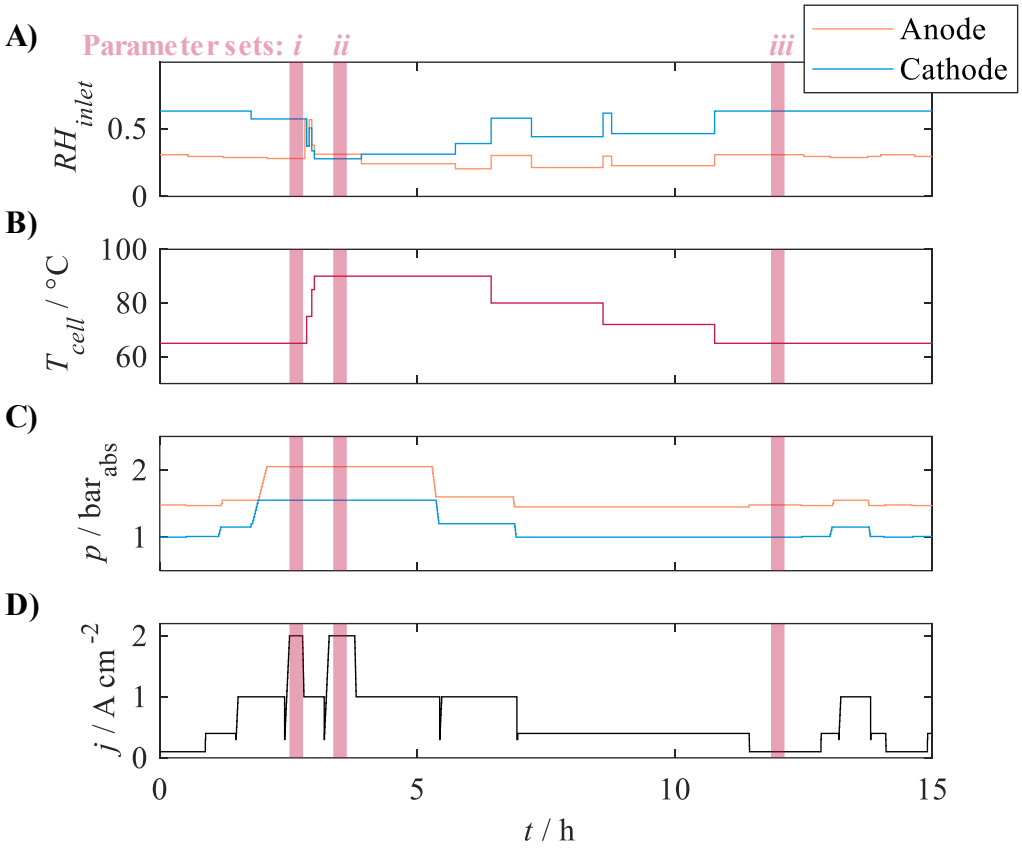

Figure 4.32. Operating parameters during one cycle of the testing protocol. **A)** Average relative humidity at the reactant inlets RH_{inlet}, **B)** cell temperature T_{cell}, **C)** gas pressures at the compartment outflows p, **D)** current density j. The labels *i*, *ii* and *iii* at the top indicate three operational parameter sets. Reprinted with permission from ref. [258].

The supply of air and hydrogen was controlled *via* the required stoichiometries. To avoid starvation effects, minimum volume flows of 1.0 l_n min^{-1} (H_2) and 2.5 l_n min^{-1} (Air) were specified. The stoichiometries were varied between 1.4 and 1.6 for air and between 1.25 and 1.38 for hydrogen. To reduce the damage caused by external influences such as test rig malfunctions, 0.3 V was specified as the lower cell voltage limit. When this limit was met for more than one second, the cell voltage was set to 0.75 V by potentiostatic means.

The time evolution of current and cell voltage during the parameter cycles are shown in **Figure 4.33**. The test ran for a total of 300 h with 20 complete cycles. There were two test interruptions at ~110 h and ~180 h, both of which resulted in a slight improvement of the cell voltage. This is usually explained by recovery effects, whereby platinum oxides are

reduced at low electrode potentials of the cathode.[155] The two right graphs in **Figure 4.33** show the fifth cycle, where the lowest voltage is ~0.4 V, which corresponds to parameter set *ii* from **Figure 4.32**. The associated temperature is 90 °C, the current density is 2.0 A cm^{-2} and the H_2/air humidification is 30%. Thus, the set with the highest temperature, lowest cathode humidification, and highest current density showed the lowest voltage. From 150 h of operation on, the parameter sets *i* and *ii* with currents of 2.0 A cm^{-2} could not be operated anymore as the cell voltage was below 0.3 V at these conditions.

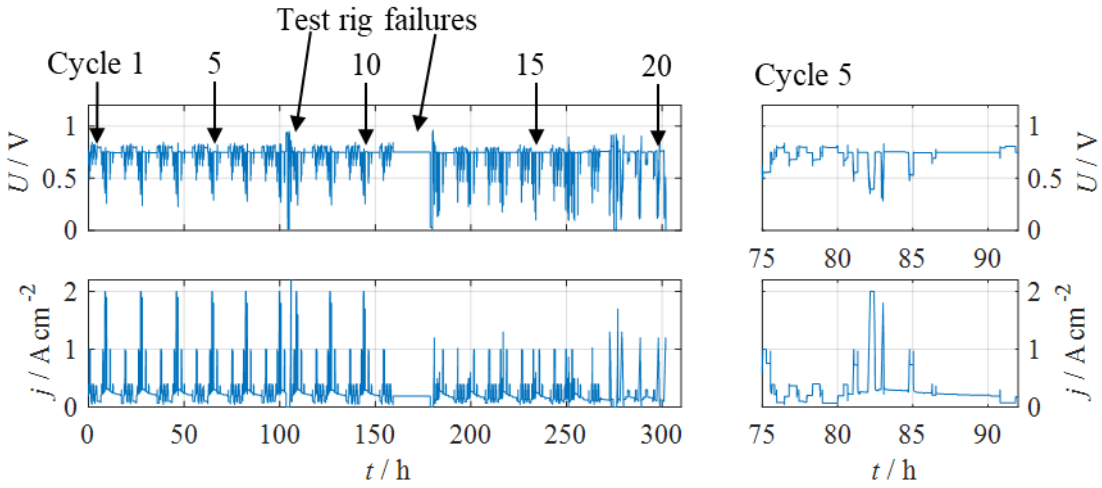

Figure 4.33. Cell voltage *U* (top left) and current density *j* (bottom left) during repetitive operation of the parameter cycle in **Figure 4.32**. Cycle 5 is exemplarily enlarged on the right.

4.4.2 Local Current Densities during Drive Cycles

CDDs in the flow direction were measured during the experiment, and it was noticed that they were more homogeneous at higher current densities. **Figure 4.34 A** shows the distribution at the parameter set *iii* defined in **Figure 4.32** after 10 h of operation. In this set, the current density is 0.1 A cm^{-2}. The currents near the hydrogen inflow ($H_{2,in}$) are larger than the average current and decrease towards the hydrogen outflow ($H_{2,out}$).

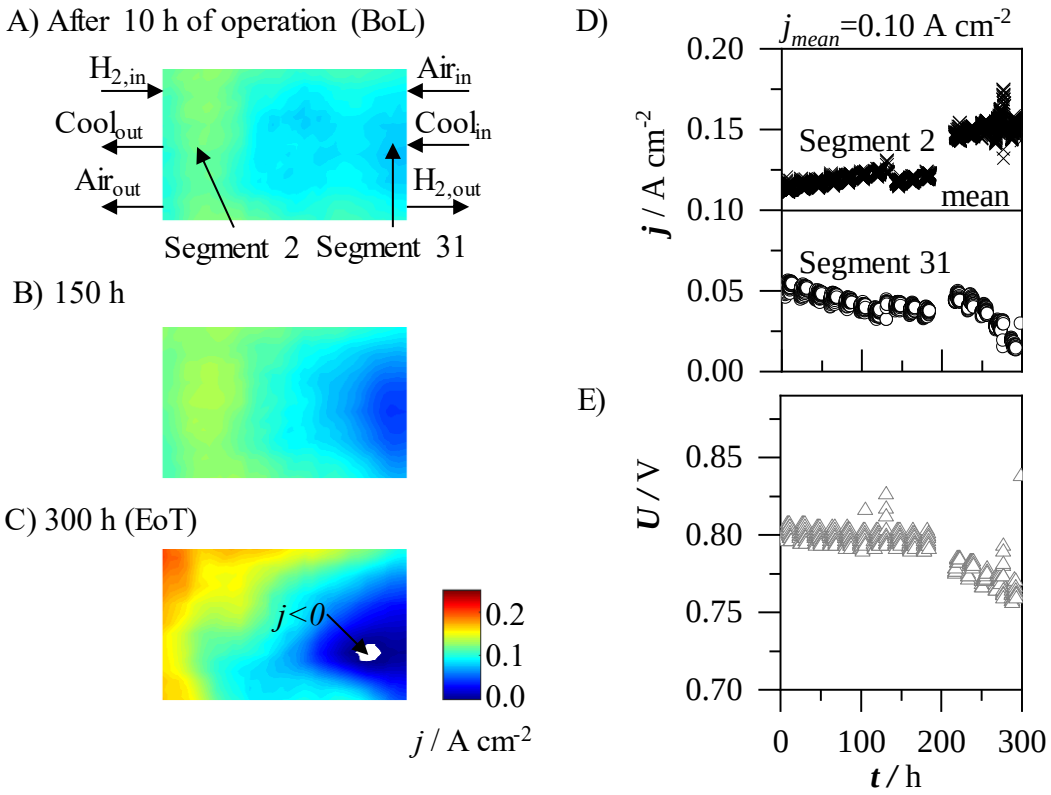

Figure 4.34. Current density distribution maps at an average current j_{mean} of 0.1 A cm^{-2} after **A)** 10 h of operation, **B)** 150 h, **C)** 300 h, and color bar, which applies for all maps. **D)** Temporal progress of the current densities of segments 2 and 31 as indicated in A). **E)** Cell voltage for j_{mean} = 0.1 A cm^{-2}. Reprinted with permission from ref. [258].

Since only selected CDD maps can be illustrated here, the currents of two segments throughout the experiment at j_{mean} = 0.1 A cm^{-2} have been plotted in **Figure 4.34 D**. Segment 2 is close to $H_{2,in}$ and segment 31 is close to $H_{2,out}$. During the test, the current of segment 2 increased continuously, while the currents near the hydrogen outflow collapse. After 150 h (**Figure 4.34 B**), a semicircular area around $H_{2,out}$ with an area of ~50 cm² had only 0.03 A cm^{-2}. It is worth noting that the cell voltage in **Figure 4.34 E** did not change noticeably within the first 150 h, whereas the current density already became more inhomogeneous. The voltage degradation in this period was 0.042 mV h^{-1}. Due to the test bench failure at 130 h, the current difference between segment 2 and 31 got somewhat smaller. In the CDD map after 300 h of operation (**Figure 4.34 C**), negative currents near $H_{2,out}$ occurred, which was observed only at current densities below 0.2 A cm^{-2} and in potentiostatic operation at 0.75 V. The voltage degradation between 200 h and 300 h was

0.25 mV h^{-1}, which is about 6 times larger than in the first 150 hours of operation. Also, the divergence of currents near $H_{2,in}$ and $H_{2,out}$ increased after 200 h. The cell voltage remained at positive values throughout the experiment (**Figure 4.33 E**), therefore degradation effects due to global hydrogen or oxygen starvation can be excluded. The behavior of the electrode potentials under fault conditions has been described in detail in section 2.2.

The profile of the CDD correlates with the partial pressure of hydrogen along the flow field. This is surprising since the exchange current density of the ORR is significantly lower than that of the HOR and for this reason the profile of the oxygen partial pressure dominates the local currents.[291] To ensure that the CDD is a consequence of the hydrogen partial pressure, the H_2 stoichiometry λ_{H2} was varied as shown in **Figure 4.35**. When adjusting the anode stoichiometry from 1.4 to 1.8, the voltage increases from 0.40 V to 0.48 V. In the CDD map at λ_{H2} = 1.4 (**Figure 4.35 A**), the current density follows the flow direction of hydrogen, where the current at $H_{2,out}$ is 0 A cm^{-2}. At λ_{H2} = 1.5, the area with small currents in **Figure 4.35 B** (colored blue) becomes smaller. When the H_2 stoichiometry is 1.8, the current density decreases along the airflow direction, which is the expected behavior due to the ORR's sluggish kinetics and the associated dependence on oxygen partial pressure. The sensitivity of the cell voltage to λ_{H2} cannot be explained by the HOR as the related overpotentials are typically small when operating with pure hydrogen.[96] We suspect local and not global hydrogen starvation in this experiment, as (1) the hydrogen stoichiometry is 1.4, (2) the cell voltage is greater than zero, and (3) the current densities in the starved areas are small. The theoretical background can be found in chapter 2.2.1. It is supposed that there is no hydrogen left in the blue-colored region in **Figure 4.35 A**, and, thus, the OER and COR take place at the cathode. The available active area for the ORR is, therefore, smaller at lower hydrogen volume flows, which increases the local current densities - as visible in **Figure 4.35 A** to **C** - and thus reduces the cell voltage.

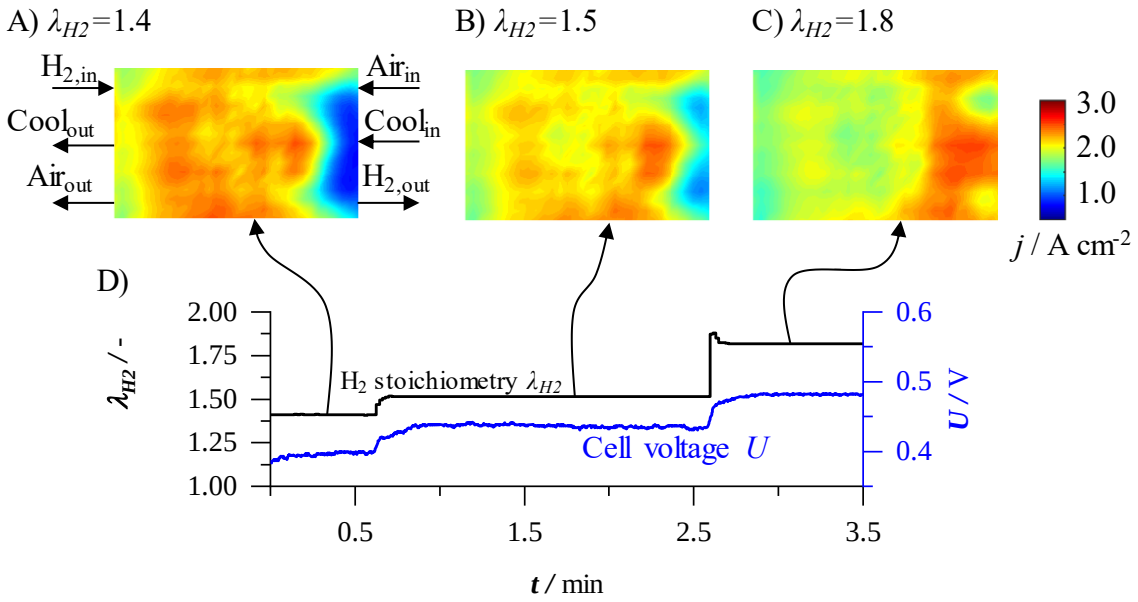

Figure 4.35. Current density distribution maps at j_{mean} = 2 A cm^{-2} for various anode stoichiometries λ_{H2}. **A)** λ_{H2} = 1.4, **B)** λ_{H2} = 1.5, and **C)** λ_{H2} = 1.8. **D)** Temporal progress of λ_{H2} and cell voltage U. Remaining operating parameters correspond to parameters set *i* in **Figure 4.32**. Reprinted with permission from ref. [258].

Humidification of the membrane may also influence the CDD in PEMFCs. For this reason, the average cell temperature was analyzed, which increased by 0.4 °C throughout the experiment. However, the temperature gradient remained constant at 1.5 K, which is why it is assumed that the membrane humidification had a small influence on the performance degradation.

4.4.3 Local Relative Humidity based on Simulations

Water droplets within the catalyst layer are often reported to be the cause of local hydrogen starvation.[57,106,149] To investigate this scenario, an isothermal computational fluid dynamic half-cell model of the anode was created, which was used to achieve a homogeneous mass flow distribution within the gas channels, as published by Enz *et al.*[292] The fluid zones were defined as the flow field, GDL, MPL and the electrodes assuming a homogeneous CDD. The mass balance was formed by the volumetric sink and source terms within the electrodes neglecting the condensation of water vapor. The geometrical and material properties of the components used in the experiment were considered. Coefficients for back-diffusion and electroosmotic drag were implemented based on experimental findings.

Figure 4.36 A shows the distribution of relative humidity within the anode catalyst layer based on numerical simulation at a current density of 0.1 A cm^{-2} (parameter set *iii* in **Figure 4.32**). The humidity increases from anode inlet to outlet and reaches a maximum value of ~163%, which makes the formation of liquid water likely. The MEA was disassembled at the end of the electrochemical test, and a photograph of the cathode catalyst layer was taken, which is illustrated in **Figure 4.36 B**. In a well-defined area around the hydrogen outflow ($H_{2,out}$) an increased occurrence of CCM cracks and MPL residues were found on the CCM. This area is marked with a yellow line in **Figure 4.36 B**. The shape and extent of the area is consistent with the areas of the computational fluid dynamic simulation where the relative humidity is greater than one. This supports the assumption that a local hydrogen starvation due to the condensation of water in the area of $H_{2,out}$ is the cause of the performance loss in **Figure 4.34 E**.

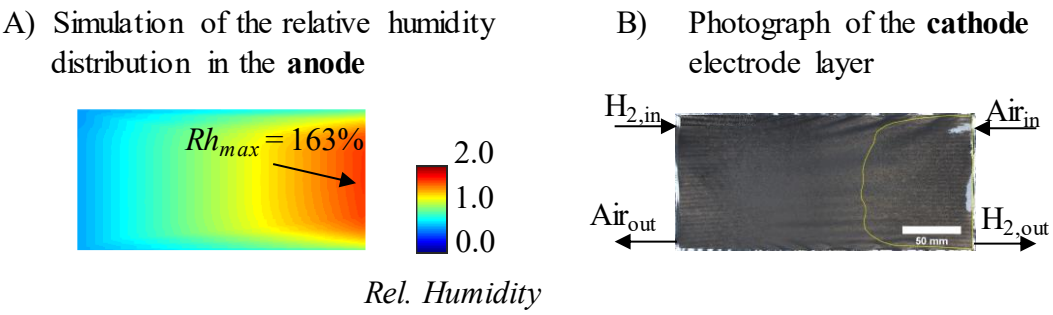

Figure 4.36. A) Computational fluid dynamic simulation of the relative humidity *RH* distribution inside the anode catalyst layer according to parameter set *iii* in **Figure 4.32**. **B)** Photograph of the cathode catalyst layer after 300 h of operation. The flow directions of H_2 and air indicated in B) do also apply for A). Reprinted with permission from ref. [258].

4.4.4 Identification of Critical Operating States

Two points were particularly relevant to identify the degradation-promoting parameter sets, namely (1) at low current densities; negative currents occur within the active area after ~300 hours of operation, and (2) water droplets near the anode outlet cause local hydrogen starvation. To analyze the entire test sequence, the CDD maps were viewed in video format, as one map was recorded every five seconds. Since videos cannot be printed in this thesis, we introduce the balanced area $A_{bal} = A_{Active} \cdot A_{total}^{-1}$, where A_{Active} is the areal sum of

measurement segments on the CSD that are in the range of ± 25% of the mean current density and A_{total} is the total active area of the MEA (288 cm^2). The lower A_{bal}, the more inhomogeneous the CDD. As shown in the CDD maps in **Figure 4.34 A** to **C**, A_{bal} decreases over the course of the experiment.

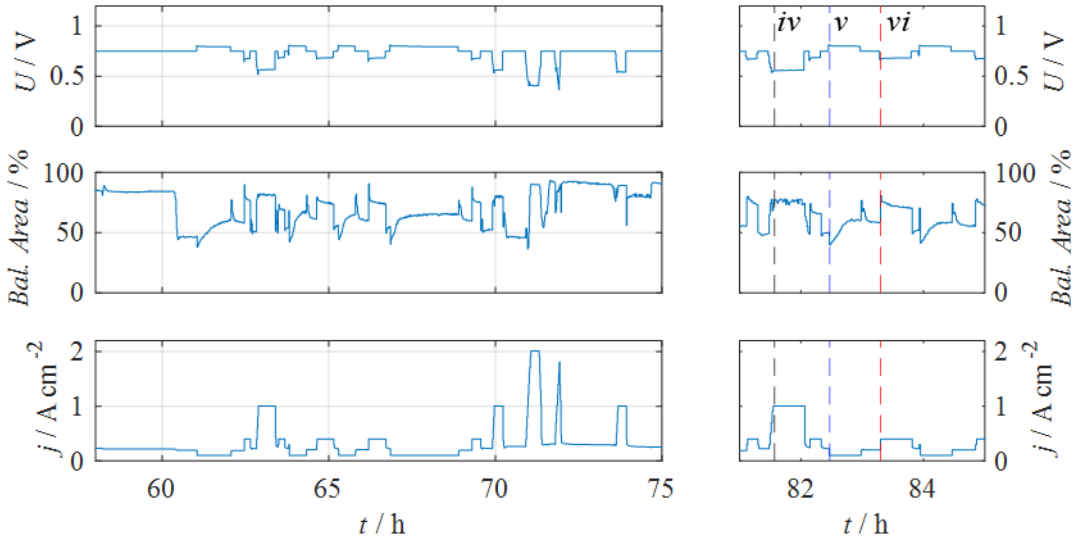

Figure 4.37. Cell voltage *U* (top left), balanced area *Bal. Area* (middle left), and current density *j* (bottom left) of parameter cycle 4 **Figure 4.32**. The operating hours 81 to 85 are enlarged on the right.

Figure 4.37 (left) shows the voltage *U* (top), balanced area *Bal. Area* (middle) and current density *j* (bottom) of cycle 4. The balanced area varies in the range of 36% to 93% within the fifth cycle. The time between 81 h and 85 hours is shown magnified on the right in **Figure 4.37** with the current densities *(iv)* 1 A cm^{-2}, *(v)* 0.1 A cm^{-2} and *(vi)* 0.4 A cm^{-2} marked with vertical lines. At point *(iv)*, the current density is homogeneously distributed ($A_{bal} \approx 82\%$), with A_{bal} varying by ± 5%. Point *(v)* represents the driest set of operating parameters due to the low current density and humidifier settings. The balanced area is at 40% at the beginning of this condition and increases continuously, whereby it takes ~18 min to reach the stable value of 60%. Point *(vi)* shows the opposite picture. Here the balanced area drops from 81% to 70% without reaching a plateau. We hypothesize that at current densities above 0.4 A cm^{-2}, water droplets are trapped at the anode due to the increased water production, but these can be largely discharged from the cell due to the large hydrogen volume flow. However, if one switches to lower current densities and thus

lower hydrogen mass flows, the droplets can no longer be removed, and local hydrogen starvation occurs. Since the operating points at 0.1 A cm^{-2} are relatively dry, the water is discharged from the anode *via* evaporation, which could explain the 18 minutes it takes to reach the maximum balanced area in point *(v)*. Consequently, one cannot designate one operating point as the cause of voltage degradation, but the sequence of a wet operating point with large H_2 volume flows and a dry operating point with low H_2 volume flows leads to local hydrogen starvation, which is the dominant degradation effect here.

4.4.5 *Ex-situ* Results and Summary

During local hydrogen starvation, the local cathode potential rises above 1.23 V, with COR taking place and degrading the carbon support.[57] To investigate this effect in more detail, two cross-sections of the cathode catalyst layer were analyzed with a scanning electron microscope, with one sample taken near the hydrogen inflow and one near the outflow. The corresponding images are shown in **Figure 4.38 A** and **B**. The typical porous structure of the catalyst near the anode inlet is still clearly visible, whereas the structure near the outlet has collapsed. In addition, the thickness of the catalyst layer is 6.8 µm at the H_2-inflow and 4.8 µm at the H_2-outflow implying carbon corrosion. **Figure 4.38 C** shows a compilation of the distribution of relative humidity in the anode layer and current density, as well as the overview photo of the cathode. The cathode catalyst collapsed at the point where (1) the highest relative humidity was during operation, (2) local current densities were zero and even negative, (3) the MPL stuck strongly to the CCM, and (4) cracks were evident in the CCM. The H_2-undersupplied area increased throughout the test (see **Figure 4.34 A** to **C**), indicating that hydrogen starvation is a self-reinforcing effect. This can be explained as cracks in the cathode CCM lead to flooding,[293] which causes anode flooding due to back diffusion through the polymer membrane.

In the automotive single cell test presented here, local hydrogen starvation was the most critical degradation mechanism. The CDD was dominated by hydrogen partial pressure due to water droplets near the hydrogen outflow, which degraded the cathode catalyst layer in this area. Since the weak point in operation was the transition from wet operating points with high hydrogen flows to dry points at low current densities, the problem could be solved by increasing the volume flows on the anode and cathode during this transition. For this purpose, however, the malfunction must be identified in real-time during operation, which may be possible in the future by means of EIS.

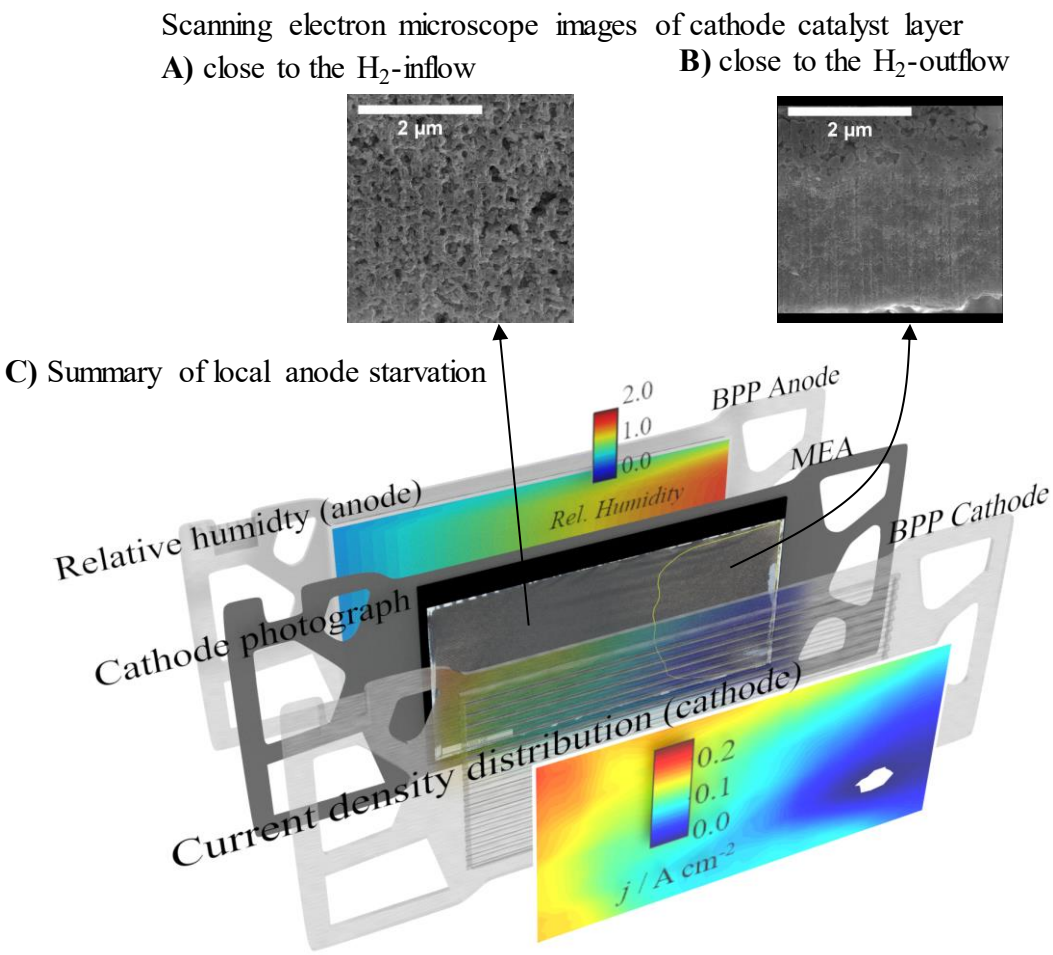

Figure 4.38. Mechanism of local anode starvation. **A)** Scanning electron microscopy (SEM) images of the cathode catalyst layer close to the hydrogen inflow and **B)** close to the hydrogen outflow. **C)** Summary of spatially resolved relative humidity in the anode catalyst layer (from **Figure 4.36 A**), photo of the cathode catalyst layer (from **Figure 4.36 B**), and current density distribution after 300 h at 0.1 A cm^{-2} (from **Figure 4.34 C**). The corresponding flow regime is illustrated in **Figure 2.3** on page 12. Abbreviations: Bipolar plates (BPPs) and membrane electrode assembly (MEA). Reprinted with permission from ref. [258].

4.5 Fuel Cell Monitoring Proposal

This brief section provides a recommendation for the necessary procedure of impedance-based real-time diagnosis of PEMFCs in automotive applications. The hypotheses mentioned here build on the findings of this thesis and have not yet been experimentally validated. In this regard, the chapter is intended to provide a motivation for further research in this area. Detecting failure modes during FCEV operation helps to increase its lifetime. Based on the linearized DIA proposed in chapter 4.1, membrane resistance, charge transfer resistance, and cell capacitance can be determined as characteristic quantities of the cell with a resolution in the range of milliseconds. It has already been described that these EEC elements can be assigned to different PEMFC malfunctions, but also cross-influences exist. This chapter recommends for the detection of faults, (1) a decision matrix to minimize cross-influences, (2) limits for the characteristic impedance parameters of the PEMFC, and the experimental determination of those.

4.5.1 Decision Process for Fault Identification

We restrict ourselves to the detection of polymer dehydration, electrode flooding, hydrogen and oxygen starvation. Since parameter variations in the entire operating parameter field of automotive PEMFCs were run within the scope of this work, we assume that other faults play a secondary role - excluding the formation of pinholes. However, since pinhole formation is often a consequence of misbehaviors,[158,159] its occurrence should be reduced by the approach presented here. The membrane resistance was significantly dependent on the humidification of the reactants and had a low cross-sensitivity to other operating parameters such as temperature and current density (see **Figure 4.11** and **Figure 4.12**). Since electrode flooding affects charge transfer resistance and cell capacitance, it is thus useful to first determine the hydration state of the membrane, which is shown as $R_{mem} > P_i$ in **Figure 4.39**. If R_{mem} exceeds a threshold value P_i, the polymer hydration is too low. This has already been published in numerous papers.[77,78,164] However, it is important to note that in the case shown here, R_{mem}, is determined with the RTIM approach and thus is less sensitive, for example, to flooding phenomena.

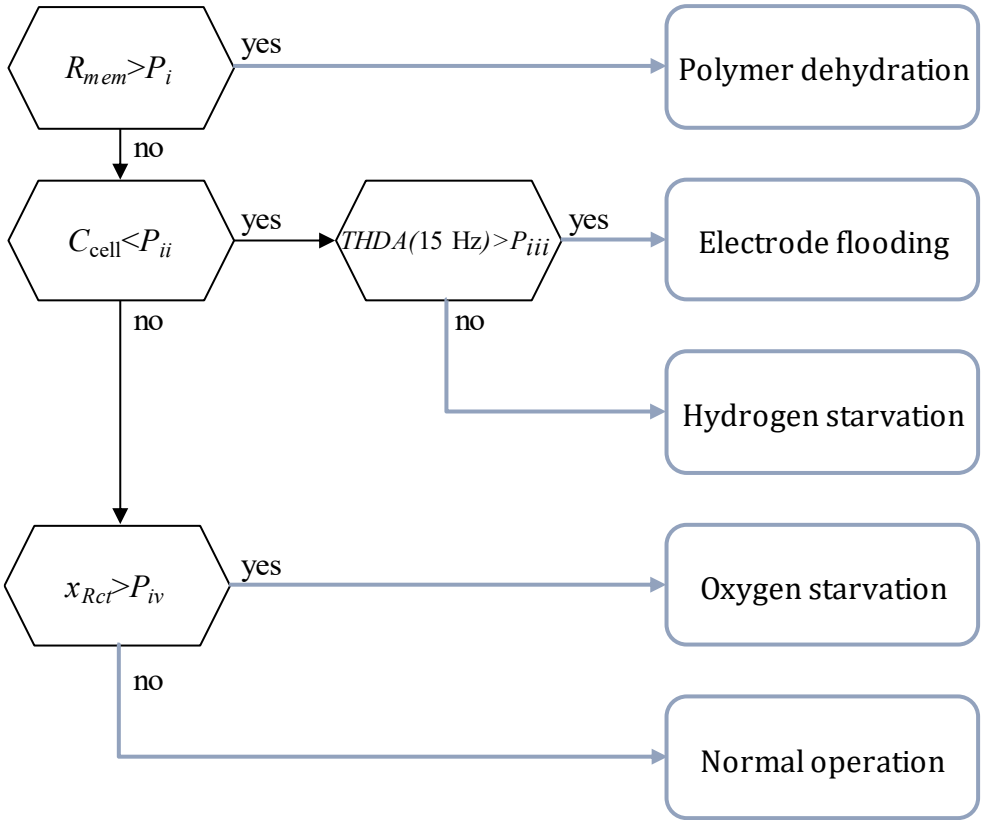

Figure 4.39. Identification of fuel cell malfunctions based on real-time impedance monitoring. Abbreviations: Membrane resistance, R_{mem}, cell capacitance, C_{cell}, charge transfer resistance error, x_{Rct}, total harmonic distortion, *THDA*, limiting parameters, *P*.

Since the charge transfer resistance alone cannot distinguish between hydrogen and oxygen starvation (see chapter 4.2.3), the cell capacitance, C_{cell}, is evaluated in a second decision step in **Figure 4.39**. If C_{cell} is smaller than a reference value P_{ii}, there is a problem at the anode electrode. The dependence of C_{cell} on the humidification is not considered here because in case of dehydration the decision matrix already indicates polymer dehydration in the first step. If the cell capacitance is low, this may be due to either electrode flooding (presumably at the anode) or hydrogen starvation. Electrode flooding was not analyzed in this work, so the reference is made to the procedure of Roy *et al.* where the standard deviation of cell impedance with respect to time is used as a criterion.[183] Since cell impedance is sensitive to most operating parameters, we propose instead to look more closely at total harmonic distortions (THDA) at frequencies of ~15 Hz as a criterion of electrode flooding. Since harmonics within the impedance response only occur during fault

conditions due to the nonlinear current-voltage behavior of the PEMFC, the cross-influences from processes during normal operation are minimal.[294,295] We hypothesize that local anode starvation is a more stable condition than droplet formation and thus has a smaller impact on THDA. Finally, the charge transfer resistance, R_{ct}, can be considered free from disturbances due to polymer dehydration, flooding or hydrogen undersupply. As described in chapter 4.2, the deviation from a theoretically calculated value for R_{ct} and the measured R_{ct} is considered (x_{Rct}) to account for current and temperature. If x_{Rct} is greater than the limit value P_{iv}, the supply of oxygen to the cathode is too low, if x_{Rct} is less than P_{iv}, the PEMFC is in normal operation.

4.5.2 Determining Parameter Limits for Fault Identification

The decision matrix in **Figure 4.39** is based on the knowledge of the parameter limits P_i to P_{iv}. This section will describe how these can be determined empirically, with the limits being specific to the individual cell setup. The data shown here correspond to the experiments in section 3.2.2 for an automotive size PEMFC. The limit of membrane resistance was determined by recording it at various current densities and humidification. **Figure 4.40 A** shows that the membrane resistance is at ~70 mΩ cm² at most operating points and only increases above 100 mΩ cm² at low humidification, which is therefore proposed as the upper limit P_i. The lower limit of the cell capacitance can be based on a CV measurement. When recording this CV, it must be ensured that the membrane resistance corresponds to the normal state (here ~70 mΩ cm²). **Figure 4.40 B** illustrates a CV measurement of an automotive size cell, including the cell capacitance during a hydrogen starvation experiment. As also described earlier (**Figure 4.12 C**), the cell capacitance collapses by more than 50%, so the lower limit of cell capacitance P_{ii} is set to 30% of the double layer capacitance extracted from CV measurements. Since no harmonic impedance analyses were presented in this work, no value for P_{iii} is suggested. The limit for the error of calculated and measured R_{ct} for the detection of low oxygen supply has already been presented in chapter 4.2.2 as $P_{iv} = 0.5$. At this value, the influence of the homogeneity of the CDD is negligible. In order to calculate the expected value of R_{ct} its diffusive components, R_{diff} must first be determined experimentally. For this purpose, R_{ct} must be measured as a function of temperature whereby the result is empirically fitted and R_{diff} can be extracted (see **Figure 4.16 A**).

A) Sensitivity of membrane resistance

B) Sensitivity of cell capacitance

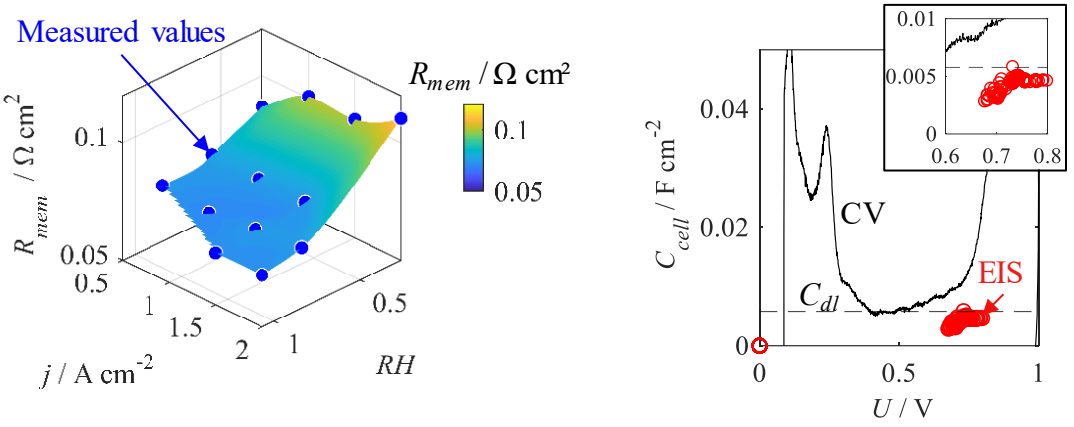

Figure 4.40. A) Sensitivity of membrane resistance, R_{mem}, on current density, j, and reactant gas humidification, RH. **B)** Cyclic voltammogram of an automotive size cell (black line) , including the cell capacitance extracted by impedance spectroscopy during a hydrogen starvation event (red dots). The black dashed horizontal line indicates the double layer capacitance, C_{dl}.

The following points should additionally be considered to extend the approach presented here. (1) Determining the dependence of the cell capacitance on polymer humidification improves the detection of anode starvation. (2) The influence of humidification on charge transfer resistance. (3) Harmonic impedance analysis as a complement or substitute for distinguishing oxygen and hydrogen starvation.

5 Conclusions and Outlook

This work aimed to develop an impedance-based measurement method that allows a physically interpretable real-time characterization of fuel cells in electric vehicles and the identification of critical operating conditions.

Cell voltage alone cannot be used to identify harmful operating conditions, which is why impedance spectroscopy on polymer electrolyte membrane fuel cells (PEMFCs) has become more relevant in recent times. As it takes ~300 s to record a full electrochemical impedance spectrum, state-of-the-art impedance-based characterizations on electric vehicles only measure at selected individual frequencies. This leads to misinterpretation, as, for example, a change in cell capacitance or electrode flooding gives the appearance of membrane dehydration. Differential impedance analysis (DIA) is less dependent on frequency shifts of the fuel cell processes than measurements at single frequencies. In order to use the DIA as real-time impedance monitoring (RTIM), a linearized approach of the DIA was developed based on five measurement frequencies. This allows the determination of the membrane resistance, charge transfer resistance and cell capacitance with similar accuracy as complex non-linear least-squares fitting procedures. The narrower the range of the five measurement frequencies, the greater the theoretical accuracy of the method. For practical applications, a spread of $\Delta f = \log_{10}(f_1/f_2) = 0.1$ allows an accuracy of 99%, which is why frequencies in the range of 119 Hz to 238 Hz are recommended. Air starvation, hydrogen starvation, and membrane dehydration can be distinguished with a time resolution of 50 ms to 100 ms using the RTIM methodology.

The semicircle in the Nyquist plot of automotive size PEMFCs in the range of ~50 Hz to ~500 Hz cannot be reproduced when assuming the oxygen reduction reaction kinetic behavior solely. We hypothesize that diffusive components in the range between 0.5 A cm^{-2} to 2.0 A cm^{-2} influence the impedance in this frequency range, which is consistent with physical models in the literature. The charge transfer resistance can be predicted based on

the current density and the temperature dependence of its diffusive components, which allows the identification of oxygen starvation during operation. The more inhomogeneous the current density distribution, the greater is the charge transfer resistance independent of the air stoichiometry. This disturbing influence is especially relevant at low current densities of 0.1 A cm^{-2} and leads to the overestimation of the charge transfer resistance of up to 12% in the operating range relevant for automotive PEMFCs, which impedes an accurate determination of the air stoichiometry.

The cell capacitance in fuel cells was less sensitive to operating conditions compared to the charge transfer resistance. The steady-state impedance and dynamic CV measurements yielded comparable results for the hydrogen underpotential deposition (HUPD) and double layer capacitances in oxygen-free operation. A drawback of the impedance-based evaluation is the voltage amplitude of the measurement, which leads to the hydrogen evolution reaction (~90 mV) interfering with the HUPD capacitance at low voltages. Since the formation of Pt-OH is comparatively slow, associated adsorption processes cannot be identified with a steady-state impedance measurement in PEMFCs. If oxygen is supplied to the cathode, the adsorption capacitance of the HUPD drops continuously until the total cell capacitance corresponds to solely the double layer. At an oxygen partial pressure of ~15 vol.% the total capacitance and double layer capacitance are equal. The oxygen reacts at the cathode *via* an intermediate step of $^{*}OH$ to form water. We believe that $^{*}OH$-adsorption occurs very rapidly at low cathode potentials of 0.09 V to 0.4 V and cannot be detected by the EIS measurement. Therefore, only regions where hydrogen is present contribute to the adsorption capacitance of the cell. Consequently, oxygen starvation of a PEMFC and the subsequent collapse of the cell voltage to below 0.4 V can be identified by an increase in cell capacitance. In contrast, during local hydrogen starvation, the cell capacitance collapses, which might be caused by (1) local anode potentials above 0.4 V, where the HUPD no longer takes place and (2) no available hydrogen for the HUPD.

Local hydrogen starvation due to water droplet formation was the dominant degradation mechanism during on-road drive cycles of an automotive size PEMFC. We hypothesize that the local hydrogen concentration impacts the area where the oxygen reduction reaction takes place. In areas with hydrogen starvation, carbon reduction takes place at the cathode while oxygen reduction is suppressed. Due to the smaller area available for oxygen reduction, the performance of the cell is reduced. The origin of the water droplet formation

was not a single parameter set but the succession of two parameter sets. If a lot of water is generated initially, for example, at high current densities, and then a transition is made to an operating point with low volume flows, removing excess water from the electrode layers can take up to 20 minutes. Hydrogen starvation can lead to cracks within the catalyst layer, which enhances water accumulation, leading to an increase in the starved area. Since this degradation mechanism leads to a shift of the local potentials, it can potentially be detected *via* an impedance-based real-time diagnosis, which allows the optimization of transitions between operating points.

In this work, we were able to describe a measurement method that can be used to detect common failures in PEMFCs, such as membrane dehydration and gas starvations in real-time. During fuel cell malfunctions, the cell's impedance takes on extreme values, which facilitates their detection. To characterize the air stoichiometry or temperature in normal operating points, more precise physical impedance models are required. In this context, it is essential to understand the dependence of the diffusion resistances on temperature. In addition, the influence of gas humidification on the cell capacitance and the charge transfer resistance should be further analyzed. One promising method in this regard is harmonic distortions in the impedance signal of PEMFCs. However, to date, relatively little work has been published based on physical models using harmonics for automotive size fuel cells.

We were able to show that impedance-based diagnostics of fuel cell systems may replace the use of expensive and fragile sensor technologies for the measurement of stack temperatures and single-cell voltages. Impedance offers the additional advantage of direct communication with the electrochemically active layer, which is currently the component of a fuel cell electric vehicle that needs the most protection from harmful operating conditions.

6 References

1. BMW Group, “The powertrain for the BMW i Hydrogen NEXT: BMW Group reaffirms its ongoing commitment to hydrogen fuel cell technology.”, can be found under https://www.press.bmwgroup.com/global/article/detail/T0306930EN/the-powertrain-for-the-bmw-i-hydrogen-next:-bmw-group-reaffirms-its-ongoing-commitment-to-hydrogen-fuel-cell-technology?language=en, **2020**.

2. UNFCCC, "Adoption of the Paris Agreement. Proposal by the President.", can be found under https://unfccc.int/resource/docs/2015/cop21/eng/l09r01.pdf, **2015**.

3. J. Rogelj, M. den Elzen, N. Höhne, T. Fransen, H. Fekete, H. Winkler, R. Schaeffer, F. Sha, K. Riahi, M. Meinshausen, *Nature* **2016**, *534*, 631-639.

4. H. Chen, H. Liao, B.-J. Tang, Y.-M. Wei, *Energy Economics* **2016**, *57*, 42-49.

5. R. Vakulchuk, I. Overland, D. Scholten, *Renewable Sustainable Energy Rev.* **2020**, DOI 10.1016/j.rser.2019.109547.

6. C. Liu, R. Chen, F. Sera, A. M. Vicedo-Cabrera, Y. Guo, S. Tong, M. S.Z.S. Coelho, P. H.N. Saldiva, E. Lavigne, P. Matus, N. Valdes Ortega, S. Osorio Garcia, M. Pascal, M. Stafoggia, M. Scortichini, M. Hashizume, Y. Honda, M. Hurtado-Díaz, J. Cruz, B. Nunes, J. P. Teixeira, H. Kim, A. Tobias, C. Íñiguez, B. Forsberg, C. Åström, M. S. Ragettli, Y.-L. Guo, B.-Y. Chen, M. L. Bell, C. Y. Wright, N. Scovronick, R. M. Garland, A. Milojevic, J. Kyselý, A. Urban, H. Orru, E. Indermitte, J. J. K. Jaakkola, N. R. I. Ryti, K. Katsouyanni, A. Analitis, A. Zanobetti, J. Schwartz, J. Chen, T. Wu, A. Cohen, A. Gasparrini, H. Kan, *N. Engl. J. Med.* **2019**, *381*, 705-715.

7. J. Guo, X. Zhang, F. Gu, H. Zhang, Y. Fan, *J. Cleaner Prod.* **2020**, *249*, 119372.

8. T. André, F. Appavou, A. Brown, G. Ellis, B. Epp, D. Gibb, F. Guerra, F. Joubert, R. Kamara, B. Kondev, R. Levin, H. E. Murdock, J. L. Sawin, K. Seyboth, J. Skeen, F. Sverrisson, G. Wright, ‘‘Renewables 2020. Global status report’’, can be found under https://www.ren21.net/reports/global-status-report/, **2020**.

9. I. Staffell, D. Scamman, A. V. Abad, P. Balcombe, P. E. Dodds, P. Ekins, N. Shah, K. R. Ward, *Energy Environ. Sci.* **2019**, *12*, 463-491.

10. Z. J. Schiffer, K. Manthiram, *Joule* **2017**, *1*, 10-14.

11. IEA 2020, "Energy Technology Perspectives", can be found under https://www.iea.org/topics/energy-technology-perspectives, **2020**.

12. IEA, "Global EV Outlook 2019", can be found under https://www.iea.org/reports/global-ev-outlook-2019, **2019**.

13. IEA, "Global EV Outlook 2020", can be found under https://www.iea.org/reports/global-ev-outlook-2020, **2020**.

14. C. Bataille, M. Åhman, K. Neuhoff, L. J. Nilsson, M. Fischedick, S. Lechtenböhmer, B. Solano-Rodriquez, A. Denis-Ryan, S. Stiebert, H. Waisman, O. Sartor, S. Rahbar, *J. Cleaner Prod.* **2018**, *187*, 960-973.

15. Y. Kim, E. Worrell, *Energy Policy* **2002**, *30*, 827-838.

16. Z. Liu, *Appl. Energy* **2016**, *166*, 239-244.

17. Y. Bicer, I. Dincer, G. Vezina, F. Raso, *Environ. Manage.* **2017**, *59*, 842–855.

18. A. Otto, M. Robinius, T. Grube, S. Schiebahn, A. Praktiknjo, D. Stolten, *Energies* **2017**, *10*, 451.

19. T. Ariyama, M. Sato, *ISIJ Int.* **2006**, *46*, 1736-1744.

20. F. Appavou, A. Brown, B. Epp, D. Gibb, B. Kondev, A. McCrone, H. E. Murdock, E. Musolino, L. Ranalder, J. L. Sawin, K. Seyboth, J. Skeen, F. Sverrisson, ‘‘Renewables 2019. Global status report’’, can be found under https://www.ren21.net/reports/global-status-report/, **2019**.

21. C. Mac Domhnaill, L. Ryan, *Renewable Energy* **2020**, *154*, 955-965.

22. M. Victoria, K. Zhu, T. Brown, G. B. Andresen, M. Greiner, *Energy Convers. Manage.* **2019**, *201*, 111977.

23. P. Sterchele, J. Brandes, J. Heilig, D. Wrede, C. Kost, T. Schlegl, A. Bett, H.-M. Henning, "Wege zu einem klimaneutralen Energiesystem: Die deutsche Energiewende im Kontext gesellschaftlicher Verhaltensweisen", can be found under https://www.ise.fraunhofer.de/de/veroeffentlichungen/studien/wege-zu-einem-klimaneutralen-energiesystem.html, **2020**.

24. A. M. Andwari, A. Pesiridis, S. Rajoo, R. Martinez-Botas, V. Esfahanian, *Renewable Sustainable Energy Rev.* **2017**, *78*, 414-430.

25. K. Forrest, M. Mac Kinnon, B. Tarroja, S. Samuelsen, *Appl. Energy* **2020**, *276*, 115439.

26. B. G. Pollet, I. Staffell, J. L. Shang, *Electrochim. Acta* **2012**, *84*, 235-249.

27. S. Mekhilef, R. Saidur, A. Safari, *Renewable Sustainable Energy Rev.* **2012**, *16*, 981-989.

28. Y. Ligen, H. Vrubel, H. H. Girault, *World Electr. Veh. J.* **2018**, *9*, 3.

29. T. Brown, D. Schlachtberger, A. Kies, S. Schramm, M. Greiner, *Energy* **2018**, *160*, 720-739.

30. Hydrogen Council, "Path to Hydrogen Competitiveness: A Cost Perspective", can be found under https://hydrogencouncil.com/en/path-to-hydrogen-competitiveness-a-cost-perspective/, **2020**.

31. S. Bruce, M. Temminghoff, J. Hayward, E. Schmidt, C. Munnings, D. Palfreyma, "National Hydrogen Roadmap. Pathways to an economically sustainable hydrogen industry in Australia", can be found under https://www.csiro.au/en/Do-business/Futures/Reports/Energy-and-Resources/Hydrogen-Roadmap, **2018**.

32. O. Gröger, H. A. Gasteiger, J.-P. Suchsland, *J. Electrochem. Soc.* **2015**, *162*, A2605-A2622.

33. R. Rath, P. Kumar, S. Mohanty, S. K. Nayak, *Int. J. Energy Res.* **2019**, *43*, 8931-8955.

34. Daimler Truck AG, "Daimler Truck AG gründet neue Daimler Truck Fuel Cell GmbH & Co. KG – Bündelung aller konzernweiter Brennstoffzellen-Aktivitäten", can be found under https://media.daimler.com/marsMediaSite/ko/de/46531890, **2020**.

35. B. K. Hong, S. H. Kim, *ECS Trans.* **2018**, *86*, 3-11.

36. Toyota Motor Corporation, "Toyota moves to expand mass-production of fuel cell stacks and hydrogen tanks towards ten-fold increase post-2020", can be found under https://global.toyota/en/newsroom/corporate/22647198.html, **2018**.

37. S. Tanaka, K. Nagumo, M. Yamamoto, H. Chiba, K. Yoshida, R. Okano, *eTransportation* **2020**, *3*, 100046.

38. BMW Group, "Statement and Presentation by Oliver Zipse, Chairman of the Board of Management of BMW AG, 100th Annual General Meeting in Munich on 14th May 2020", can be found under https://www.press.bmwgroup.com/global/article/detail/T0308457EN/statement-and-presentation-by-oliver-zipse-chairman-of-the-board-of-management-of-bmw-ag-100th-annual-general-meeting-in-munich-on-14th-may-2020?language=en, **2020**.

39. O. Tlili, C. Mansilla, D. Frimat, Y. Perez, *Int. J. Hydrogen Energy* **2019**, *44*, 16048-16068.

40. R. C. Samsun, L. Antoni, M. Rex, "Mobile fuel cell application: Tracking market trends", can be found under https://www.ieafuelcell.com/fileadmin/publications /2020_AFCTCP_Mobile_FC_Application_Tracking_Market_Trends_2020.pdf, **2019**.

41. D. Apostolou, G. Xydis, *Renewable Sustainable Energy Rev.* **2019**, *113*, 109292.

42. J. Meckling, J. Nahm, *Energy Policy* **2019**, *126*, 470-479.

43. P. Plötz, J. Axsen, S. A. Funke, T. Gnann, *Nat Sustain* **2019**, *2*, 534-536.

44. G. Trencher, *Energy Reports* **2020**, *6*, 2503-2519.

45. J. Yunzhe, Z. Bowei, W. Feifei, L. Mengmeng, *IOP Conf. Ser.: Earth Environ. Sci.* **2020**, *512*, 012136.

46. G. Trencher, A. Taeihagh, M. Yarime, *Energy Policy* **2020**, *142*, 111533.

47. A. Ajanovic, R. Haas, *Int. J. Hydrogen Energy* **2020**, in press, DOI 10.1016/j.ijhydene.2020.03.122.

48. A. G. Olabi, T. Wilberforce, M. A. Abdelkareem, *Energy* **2021**, *214*, 118955.

49. K. D. Rasmussen, H. Wenzel, C. Bangs, E. Petavratzi, G. Liu, *Environ. Sci. Technol.* **2019**, *53*, 11541-11551.

50. C. Couderc, *Platinum Met. Rev.* **2010**, *54*, 186–191.

51. S. Singh, S. Jain, V. PS, A. K. Tiwari, M. R. Nouni, J. K. Pandey, S. Goel, *Renewable Sustainable Energy Rev.* **2015**, *51*, 623-633.

52. U. Eberle, R. von Helmolt, *Energy Environ. Sci.* **2010**, *3*, 689-699.

53. J. Zhao, X. Li, *Energy Convers. Manage.* **2019**, *199*, 112022.

54. J. Wang, *Energy* **2015**, *80*, 509-521.

55. J. Du, M. Ouyang, J. Chen, *Energy* **2017**, *120*, 584-596.

56. U.S. Department of Energy, "DOE Technical Targets for Fuel Cell Systems and Stacks for Transportation Applications", can be found under https://www.energy.gov/eere/fuelcells/doe-technical-targets-fuel-cell-systems-and-stacks-transportation-applications, **2015**.

57. C. A. Reiser, L. Bregoli, T. W. Patterson, J. S. Yi, J. D. Yang, M. L. Perry, T. D. Jarvi, *Electrochem. Solid-State Lett.* **2005**, *8*, A273-A276.

58. M. Obermaier, M. Rauber, A. Bauer, T. Lochner, F. Du, C. Scheu, *Fuel Cells* **2020**, *20*, 394-402.

59. P. Pei, H. Chen, *Appl. Energy* **2014**, *125*, 60-75.

60. K. Yezerska, A. Dushina, F. Liu, M. Rastedt, P. Wagner, A. Dyck, M. Wark, *Int. J. Hydrogen Energy* **2019**, *44*, 18330-18339.

61. M. Muthukumar, N. Rengarajan, B. Velliyangiri, M. A. Omprakas, C. B. Rohit, U. K. Raja, *Mater. Today: Proc.* **2020**, in press, DOI 10.1016/j.matpr.2020.03.679.

62. F. Nandjou, J.-P. Poirot-Crouvezier, M. Chandesris, J.-F. Blachot, C. Bonnaud, Y. Bultel, *J. Power Sources* **2016**, *326*, 182-192.

63. M. M. Whiston, I. L. Azevedo, S. Litster, K. S. Whitefoot, C. Samaras, J. F. Whitacre, *Proc. Natl. Acad. Sci. U. S. A.* **2019**, *116*, 4899-4904.

64. M. A. Rubio, A. Urquia, S. Dormido, *Int. J. Hydrogen Energy* **2010**, *35*, 2586-2590.

65. D. Aaron, S. Yiacoumi, C. Tsouris, *Sep. Sci. Technol.* **2008**, *43*, 2307-2320.

66. S. M. R. Niya, M. Hoorfar, *J. Power Sources* **2013**, *240*, 281-293.

67. D. Malevich, E. Halliop, B. Peppley, J. Pharoah, K. Karan, *ECS Trans.* **2008**, *16*, 1763-1774.

68. M. A. Danzer, E. P. Hofer, *J. Power Sources* **2009**, *190*, 25-33.

69. N. Fouquet, C. Doulet, C. Nouillant, G. Dauphin-Tanguy, B. Ould-Bouamama, *J. Power Sources* **2006**, *159*, 905-913.

70. A. Kulikovsky, *eTransportation* **2019**, *2*, 100026.

71. A. Kulikovsky, *J. Electroanal. Chem.* **2018**, *823*, 335-341.

72. A. A. Kulikovsky, *J. Electrochem. Soc.* **2014**, *162*, F217-F222.

73. P. Boillat, F. N. Büchi, L. Gubler, T. J. Schmidt, *Meet. Abstr.* **2019**, *MA2019-02*, 1435.

74. I. A. Schneider, M. H. Bayer, A. Wokaun, G. G. Scherer, *ECS Trans.* **2009**, *25*, 937-948.

75. T. E. Springer, T. A. Zawodzinski, S. Gottesfeld, *J. Electrochem. Soc.* **1991**, *138*, 2334-2342.

76. T. Reshetenko, A. Kulikovsky, *RSC Adv.* **2019**, *9*, 38797-38806.

77. T. Kurz, A. Hakenjos, J. Krämer, M. Zedda, C. Agert, *J. Power Sources* **2008**, *180*, 742-747.

78. N. Kitamura, K. Manabe, Y. Nonobe, M. Kizaki, *SAE [Tech. Pap.]* **2010**, DOI 10.4271/2010-01-1088.

79. N. Fouquet, *2010 IEEE VPPC* **2010**, DOI 10.1109/VPPC.2010.5729160.

80. P. Kurzweil, H.-J. Fischle, *J. Power Sources* **2004**, *127*, 331-340.

81. H. Nakajima, T. Kitahara, *Heat Mass Transfer* **2018**, *54*, 2551–2558.

82. G. Dotelli, R. Ferrero, P. Gallo Stampino, S. Latorrata, S. Toscani, *IEEE Trans. Instrum. Meas.* **2016**, *65*, 1007-1014.

83. C. Brunetto, A. Moschetto, G. Tina, *Electr. Power Syst. Res.* **2009**, *79*, 17-26.

84. F. Mack, R. Laukenmann, S. Galbiati, J. A. Kerres, R. Zeis, *ECS Trans.* **2015**, *69*, 1075-1087.

85. J. O'Rourke, M. Ramani, M. Arcak, *Int. J. Hydrogen Energy* **2008**, *33*, 4694-4701.

86. J. P. Schmidt, S. Arnold, A. Loges, D. Werner, T. Wetzel, E. Ivers-Tiffée, *J. Power Sources* **2013**, *243*, 110-117.

87. T. Lochner, R. M. Kluge, J. Fichtner, H. A. El-Sayed, B. Garlyyev, A. S. Bandarenka, *ChemElectroChem* **2020**, *7*, 3545-3568.

88. K. Yamada, K. Suzuki, Y. Tabe, T. Chikahisa, *ECS Trans.* **2013**, *58*, 463-471.

89. D. M. Bernardi, M. W. Verbrugge, *AIChE J.* **1991**, *37*, 1151-1163.

90. W. Sheng, H. A. Gasteiger, Y. Shao-Horn, *J. Electrochem. Soc.* **2010**, *157*, B1529.

91. K. C. Neyerlin, W. Gu, J. Jorne, H. A. Gasteiger, *J. Electrochem. Soc.* **2006**, *153*, A1955.

92. E. H. Majlan, D. Rohendi, W. R. W. Daud, T. Husaini, M. A. Haque, *Renewable Sustainable Energy Rev.* **2018**, *89*, 117-134.

93. T. Yoshida, K. Kojima, *Electrochem. Soc. Interface* **2015**, *24*, 45-49.

94. A. Kongkanand, M. F. Mathias, *J. Phys. Chem. Lett.* **2016**, *7*, 1127-1137.

95. M. L. Perry, J. Newman, E. J. Cairns, *J. Electrochem. Soc.* **1998**, *145*, 5-15.

96. K. C. Neyerlin, H. A. Gasteiger, C. K. Mittelsteadt, J. Jorne, W. Gu, *J. Electrochem. Soc.* **2005**, *152*, A1073-A1080.

97. K.-H. Kim, K.-Y. Lee, H.-J. Kim, E. Cho, S.-Y. Lee, T.-H. Lim, S. P. Yoon, I. C. Hwang, J. H. Jang, *Int. J. Hydrogen Energy* **2010**, *35*, 2119-2126.

98. S. Ott, A. Orfanidi, H. Schmies, B. Anke, H. N. Nong, J. Hübner, U. Gernert, M. Gliech, M. Lerch, P. Strasser, *Nat. Mater.* **2020**, *19*, 77-85.

99. D. Qiu, L. Peng, X. Lai, M. Ni, W. Lehnert, *Renewable Sustainable Energy Rev.* **2019**, *113*, 109289.

100. Q. Li, D. Aili, R. F. Savinell, J. O. Jensen in *High Temperature Polymer Electrolyte Membrane Fuel Cells. Approaches, Status, and Perspectives*, (Eds.: Q. Li, D. Aili, H. A. Hjuler, J. O. Jensen), Springer International Publishing, **2016**, pp. 37-57.

101. A. Kraytsberg, Y. Ein-Eli, *Energy Fuels* **2014**, *28*, 7303-7330.

102. R. L. Borup, R. Mukundan, K. L. More, K. C. Neyerlin, A. Weber, D. J. Myers, R. Ahluwalia, "PEM Fuel Cell Catalyst Layer (MEA) Architectures", can be found under https://www.osti.gov/biblio/1440415, **2018**.

103. S. S. Kocha, J. Deliang Yang, J. S. Yi, *AIChE J.* **2006**, *52*, 1916-1925.

104. Y. Chang, J. Liu, R. Li, J. Zhao, Y. Qin, J. Zhang, Y. Yin, X. Li, *Energy Convers. Manage.* **2019**, *189*, 24-32.

105. E. L. Thompson, J. Jorne, W. Gu, H. A. Gasteiger, *J. Electrochem. Soc.* **2008**, *155*, B625-B634.

106. R. Borup, J. Meyers, B. Pivovar, Y. S. Kim, R. Mukundan, N. Garland, D. Myers, M. Wilson, F. Garzon, D. Wood, P. Zelenay, K. More, K. Stroh, T. Zawodzinski, J. Boncella, J. E. McGrath, M. Inaba, K. Miyatake, M. Hori, K. Ota, Z. Ogumi, S. Miyata, A. Nishikata, Z. Siroma, Y. Uchimoto, K. Yasuda, K.-i. Kimijima, N. Iwashita, *Chem. Rev.* **2007**, *107*, 3904-3951.

107. J. C. Meier, C. Galeano, I. Katsounaros, J. Witte, H. J. Bongard, A. A. Topalov, C. Baldizzone, S. Mezzavilla, F. Schüth, K. J. J. Mayrhofer, *Beilstein J. Nanotechnol.* **2014**, *5*, 44-67.

108. W. Bi, G. E. Gray, T. F. Fuller, *Electrochem. Solid-State Lett.* **2007**, *10*, B101.

109. W. Bi, T. F. Fuller, *ECS Trans.* **2007**, *11*, 1235.

110. S. R. Dhanushkodi, S. Kundu, M. W. Fowler, M. D. Pritzker, *J. Power Sources* **2014**, *245*, 1035-1045.

111. T. Mittermeier, A. Weiß, F. Hasché, G. Hübner, H. A. Gasteiger, *J. Electrochem. Soc.* **2016**, *164*, F127-F137.

112. D. A. Stevens, J. R. Dahn, *Carbon* **2005**, *43*, 179-188.

113. L. Castanheira, W. O. Silva, F. H. B. Lima, A. Crisci, L. Dubau, F. Maillard, *ACS Catal.* **2015**, *5*, 2184-2194.

114. K. H. Lim, H.-S. Oh, S.-E. Jang, Y.-J. Ko, H.-J. Kim, H. Kim, *J. Power Sources* **2009**, *193*, 575-579.

115. J. Park, H. Oh, T. Ha, Y. I. Lee, K. Min, *Appl. Energy* **2015**, *155*, 866-880.

116. R. L. Borup, R. Mukundan, *ECS Trans.* **2010**, *33*, 17-26.

117. P. Irmscher, D. Qui, H. Janßen, W. Lehnert, D. Stolten, *Int. J. Hydrogen Energy* **2019**, *44*, 23406-23415.

118. A. Forner-Cuenca, V. Manzi-Orezzoli, P. M. Kristiansen, L. Gubler, T. J. Schmidt, P. Boillat, *Radiat. Phys. Chem.* **2017**, *135*, 133-141.

119. X.-Z. Yuan, E. Gu, R. Bredin, M. Baker, S. Lee, T. Biggs, A. Bock, V. Banhardt, J. Russell, F. Girard, *J. Power Sources* **2020**, *477*, 229009.

120. T. Chen, S. Liu, J. Zhang, M. Tang, *Int. J. Heat Mass Transfer* **2019**, *128*, 1168-1174.

121. Y. Chen, C. Jiang, C. Cho, *Polymers* **2019**, *11*, 428.

122. Q. Meyer, Y. Zeng, C. Zhao, *Adv. Mater.* **2019**, *31*, 1901900.

123. X. Xie, R. Wang, K. Jiao, G. Zhang, J. Zhou, Q. Du, *Renewable Energy* **2018**, *117*, 125-134.

124. F. Onishi, Y. Tabe, T. Chikahisa, *ECS Trans.* **2018**, *86*, 89-96.

125. I. Nitta, T. Hottinen, O. Himanen, M. Mikkola, *J. Power Sources* **2007**, *171*, 26-36.

126. T. Lochner, M. Perchthaler, F. Hnyk, D. Sick, J. P. Sabawa, A. S. Bandarenka, *ChemElectroChem* **2020**, *8*, 96-102.

127. G. Zhang, S. G. Kandlikar, *Int. J. Hydrogen Energy* **2012**, *37*, 2412-2429.

128. A. Faghri, Z. Guo, *Int. J. Heat Mass Transfer* **2005**, *48*, 3891-3920.

129. M. Ramezanizadeh, M. A. Nazari, M. H. Ahmadi, L. Chen, *Int. J. Heat Mass Transfer* **2019**, *139*, 517-525.

130. S. Kang, K. Min, F. Mueller, J. Brouwer, *Int. J. Hydrogen Energy* **2009**, *34*, 6749-6764.

131. R. Shimoi, M. Masuda, K. Fushinobu, Y. Kozawa, K. Okazaki, *J. Energy Resour. Technol* **2004**, *126*, 258-261.

132. A. Hakenjos, H. Muenter, U. Wittstadt, C. Hebling, *J. Power Sources* **2004**, *131*, 213-216.

133. M. Wang, H. Guo, C. Ma, *J. Power Sources* **2006**, *157*, 181-187.

134. T.-F. Cao, Y.-T. Mu, J. Ding, H. Lin, Y.-L. He, W.-Q. Tao, *Int. J. Heat Mass Transfer* **2015**, *87*, 544-556.

135. S. Basu, M. W. Renfro, B. M. Cetegen, *J. Power Sources* **2006**, *162*, 286-293.

136. B. Wu, M. A. Parkes, L. de Benedetti, A. J. Marquis, G. J. Offer, N. P. Brandon, *J. Appl. Electrochem.* **2016**, *46*, 1157–1162.

137. M. Noorkami, J. B. Robinson, Q. Meyer, O. A. Obeisun, E. S. Fraga, T. Reisch, P. R. Shearing, D. J. L. Brett, *Int. J. Hydrogen Energy* **2014**, *39*, 1439-1448.

138. W. Schmittinger, A. Vahidi, *J. Power Sources* **2008**, *180*, 1-14.

139. C. Qin, J. Wang, D. Yang, B. Li, C. Zhang, *Catalysts* **2016**, *6*, 197.

140. H. Chen, X. Zhao, T. Zhang, P. Pei, *Energy Convers. Manage.* **2019**, *182*, 282-298.

141. A. Taniguchi, T. Akita, K. Yasuda, Y. Miyazaki, *J. Power Sources* **2004**, *130*, 42-49.

142. D. Liang, Q. Shen, M. Hou, Z. Shao, B. Yi, *J. Power Sources* **2009**, *194*, 847-853.

143. M. A. Travassos, V. V. Lopes, R. A. Silva, A. Q. Novais, C. M. Rangel, *Int. J. Hydrogen Energy* **2013**, *38*, 7684-7696.

144. P. Mandal, B. K. Hong, J.-G. Oh, S. Litster, *J. Power Sources* **2018**, *397*, 397-404.

145. X.-G. Yang, Q. Ye, P. Cheng, *Int. J. Hydrogen Energy* **2012**, *37*, 14439-14453.

146. F. Zhou, S. J. Andreasen, S. K. Kær, D. Yu, *Int. J. Hydrogen Energy* **2015**, *40*, 2833-2839.

147. W. R. R. Baumgartner, E. Wallnöfer, T. Schaffer, V. Hacker, V. Peinecke, P. Prenninger, *ECS Trans.* **2006**, *3*, 811-825.

148. P. T. Yu, W. Gu, J. Zhang, R. Makharia, F. T. Wagner, H. A. Gasteiger in *Polymer Electrolyte Fuel Cell Durability*, Vol. 1 (Eds.: F. N. Büchi, I. Minoru, T. J. Schmidt), Springer, New York, **2009**, pp. 29-53.

149. W. Gu, P. T. Yu, R. N. Carter, R. Makharia, H. A. Gasteiger in *Modeling and Diagnostics of Polymer Electrolyte Fuel Cells*, (Eds.: U. Pasaogullari, C.-Y. Wang), Springer, New York, **2010**, pp. 45-87.

150. J. P. Meyers, R. M. Darling, *J. Electrochem. Soc.* **2006**, *153*, A1432-A1442.

151. S. Abbou, J. Dillet, G. Maranzana, S. Didierjean, O. Lottin, *J. Power Sources* **2017**, *340*, 419-427.

152. A. Taniguchi, T. Akita, K. Yasuda, Y. Miyazaki, *Int. J. Hydrogen Energy* **2008**, *33*, 2323-2329.

153. M. Dou, M. Hou, D. Liang, Q. Shen, H. Zhang, W. Lu, Z. Shao, B. Yi, *J. Power Sources* **2011**, *196*, 2759-2762.

154. N. Zamel, R. Hanke-Rauschenbach, S. Kirsch, A. Bhattarai, D. Gerteisen, *Int. J. Hydrogen Energy* **2013**, *38*, 15318-15327.

155. M. Bodner, A. Schenk, D. Salaberger, M. Rami, C. Hochenauer, V. Hacker, *Fuel Cells* **2017**, *17*, 18-26.

156. S. Qu, X. Li, M. Hou, Z. Shao, B. Yi, *J. Power Sources* **2008**, *185*, 302-310.

157. W. Lü, Z. Liu, C. Wang, Z. Mao, M. Zhang, *Int. J. Energy Res.* **2011**, *35*, 24-30.

158. L. Ghassemzadeh, S. Holdcroft, *J. Am. Chem. Soc.* **2013**, *135*, 8181-8184.

159. S. Kreitmeier, M. Michiardi, A. Wokaun, F. N. Büchi, *Electrochim. Acta* **2012**, *80*, 240-247.

160. M. Hu, G. Cao, *Int. J. Hydrogen Energy* **2014**, *39*, 7940-7954.

161. M. Bodner, C. Hochenauer, V. Hacker, *J. Power Sources* **2015**, *295*, 336-348.

162. M. Mamlouk, T. Sousa, K. Scott, *Int. J. Electrochem.* **2011**, *2011*, 520473.

163. T. Ruiu, A. M. Dreizler, J. Mitzel, E. Gülzow, *J. Power Sources* **2016**, *303*, 257-266.

164. Z. Tang, Q.-A. Huang, Y.-J. Wang, F. Zhang, W. Li, A. Li, L. Zhang, J. Zhang, *J. Power Sources* **2020**, *468*, 228361.

165. Q.-A. Huang, R. Hui, B. Wang, J. Zhang, *Electrochim. Acta* **2007**, *52*, 8144-8164.

166. A. A. Al-Ali, A. S. Elwakil, B. J. Maundy, *2018 IEEE MWSCAS* **2018**, DOI 10.1109/MWSCAS.2018.8623938.

167. M. A. Mousa, A. AboBakr, L. A. Said, A. H. Madian, A. S. Elwakil, A. G. Radwan, *2019 Fourth International Conference ACTEA* **2019**, DOI 10.1109/ACTEA.2019.8851098.

168. R. Mattiello, M. A. Amaral, E. Mundstock, P. K. Ziegelmann, *Clin. Nutr.* **2020**, *39*, 1411-1417.

169. D. G. Sanchez, T. Ruiu, K. A. Friedrich, J. Sanchez-Monreal, M. Vera, *J. Electrochem. Soc.* **2016**, *163*, F150-F159.

170. M. E. Orazem, B. Tribollet, *Electrochemical Impedance Spectroscopy*, Vol. 2, John Wiley & Sons, Incorporated, **2008**, pp. i-xxxi.

171. X. Yuan, H. Wang, J. C. Sun, J. Zhang, *Int. J. Hydrogen Energy* **2007**, *32*, 4365-4380.

172. H. Wang, A. Gaillard, D. Hissel, *Renewable Energy* **2019**, *141*, 124-138.

173. A. Lasia, Electrochemical Impedance Spectroscopy and its Applications, Springer, New York, **2014**, pp. 7-66.

174. X.-Z. Yuan, C. Song, H. Wang, J. Zhang, Electrochemical Impedance Spectroscopy in PEM Fuel Cells: Fundamentals and Applications, Springer, London, **2010**, pp. 39-93, pp. 139-192 and pp. 347-420.

175. B. A. Boukamp, *Solid State Ionics* **1993**, *62*, 131-141.

176. J. R. Macdonald, *Electrochim. Acta* **1993**, *38*, 1883-1890.

177. K. Darowicki, E. Janicka, M. Mielniczek, A. Zielinski, L. Gawel, J. Mitzel, J. Hunger, *Electrochim. Acta* **2018**, *292*, 383-389.

178. G. Wang, Y. Yu, H. Liu, C. Gong, S. Wen, X. Wang, Z. Tu, *Fuel Process. Technol.* **2018**, *179*, 203-228.

179. H. Wang, A. Gaillard, D. Hissel, *Int. J. Hydrogen Energy* **2019**, *44*, 1110-1121.

180. H.-S. Park, M.-H. Shin, T.-H. Eom, C.-Y. Won, S.-D. Kang, T.-H. Min, *IFEEC 2017 - ECCE Asia* **2017**, DOI 10.1109/IFEEC.2017.7992286.

181. K. Tajiri, C.-Y. Wang, Y. Tabuchi, *Electrochim. Acta* **2008**, *53*, 6337-6343.

182. S. Yuan, F. Zhou, Q. Ren, J. Yu, Y. Xu, Y. Zhang, *2019 CAC* **2019**, DOI 10.1109/CAC48633.2019.8996819.

183. S. K. Roy, M. E. Orazem, *J. Power Sources* **2008**, *184*, 212-219.

184. O. Bethoux, M. Hilairet, T. Azib, *2009 35th Annual Conference of IEEE Industrial Electronics* **2009**, DOI 10.1109/IECON.2009.5415422.

185. T. Ma, Z. Zhang, W. Lin, J. Kang, Y. Yang, *SAE [Tech. Pap.]* **2020**, DOI 10.4271/2020-01-5131.

186. T. Sutharssan, D. Montalvao, Y. K. Chen, W.-C. Wang, C. Pisac, H. Elemara, *Renewable Sustainable Energy Rev.* **2017**, *75*, 440-450.

187. J.-M. Le Canut, R. M. Abouatallah, D. A. Harrington, *J. Electrochem. Soc.* **2006**, *153*, A857-A864.

188. P. Hong, L. Xu, H. Jiang, J. Li, M. Ouyang, *Int. J. Hydrogen Energy* **2017**, *42*, 19156-19169.

189. P. Ren, P. Pei, Y. Li, Z. Wu, D. Chen, S. Huang, X. Jia, *Appl. Energy* **2019**, *239*, 785-792.

190. J. E. B. Randles, *Discuss. Faraday Soc.* **1947**, *1*, 11-19.

191. A. Kulikovsky, *J. Electrochem. Soc.* **2019**, *166*, F306-F311.

192. A. Kulikovsky, *Electrochem. Commun.* **2017**, *84*, 28-31.

193. N. Wagner, E. Gülzow, *J. Power Sources* **2004**, *127*, 341-347.

194. D. Vladikova, Z. Stoynov, *J. Electroanal. Chem.* **2004**, *572*, 377-387.

195. B. Sanchez, A. S. Bandarenka, G. Vandersteen, J. Schoukens, R. Bragos, *Med. Eng. Phys.* **2013**, *35*, 1349-1357.

196. D. Vladikova, P. Zoltowski, E. Makowska, Z. Stoynov, *Electrochim. Acta* **2002**, *47*, 2943-2951.

197. E. Ivers-Tiffée, A. Weber, *J. Ceram. Soc. Jpn.* **2017**, *125*, 193-201.

198. A. Weiß, S. Schindler, S. Galbiati, M. A. Danzer, R. Zeis, *Electrochim. Acta* **2017**, *230*, 391-398.

199. T. Lochner, M. Perchthaler, J. T. Binder, J. P. Sabawa, T. A. Dao, A. S. Bandarenka, *ChemElectroChem* **2020**, *7*, 2784-2791.

200. D. Malevich, E. Halliop, B. A. Peppley, J. G. Pharoah, K. Karan, *J. Electrochem. Soc.* **2009**, *156*, B216-B224.

201. D. D. Macdonald, M. C. H. McKubre in *Impedance Spectroscopy: Theory, Experiment, and Applications*, Vol. 2 (Eds.: E. Barsoukov, J. R. Macdonald), John Wiley & Sons, Inc., Hoboken, New Jersey **2005**, pp. 343-429.

202. S. Watzele, J. Fichtner, B. Garlyyev, J. N. Schwämmlein, A. S. Bandarenka, *ACS Catal.* **2018**, *8*, 9456-9462.

203. D. R. Franceschetti, *J. Electroanal. Chem. Interfacial Electrochem.* **1984**, *178*, 1-9.

204. A. S. Bondarenko, *Anal. Chim. Acta* **2012**, *743*, 41-50.

205. J. P. Sabawa, A. S. Bandarenka, *Electrochim. Acta* **2019**, *311*, 21-29.

206. A. S. Bondarenko, I. E. L. Stephens, H. A. Hansen, F. J. Pérez-Alonso, V. Tripkovic, T. P. Johansson, J. Rossmeisl, J. K. Nørskov, I. Chorkendorff, *Langmuir* **2011**, *27*, 2058-2066.

207. M. D. Pohl, V. Colic, D. Scieszka, A. S. Bandarenka, *Phys. Chem. Chem. Phys.* **2016**, *18*, 10792-10799.

208. J. Tymoczko, W. Schuhmann, A. S. Bandarenka, *Electrochem. Commun.* **2013**, *27*, 42-45.

209. E. Sibert, R. Faure, R. Durand, *J. Electroanal. Chem.* **2001**, *515*, 71-81.

210. T. Pajkossy, D. M. Kolb, *Electrochim. Acta* **2001**, *46*, 3063-3071.

211. T. E. Springer, T. A. Zawodzinski, M. S. Wilson, S. Gottesfeld, *J. Electrochem. Soc.* **1996**, *143*, 587-599.

212. S. Jeon, J. Lee, G. M. Rios, H.-J. Kim, S.-Y. Lee, E. Cho, T.-H. Lim, J. H. Jang, *Int. J. Hydrogen Energy* **2010**, *35*, 9678-9686.

213. Y. Bultel, K. Wiezell, F. Jaouen, P. Ozil, G. Lindbergh, *Electrochim. Acta* **2005**, *51*, 474-488.

214. J. Zhang, Y. Tang, C. Song, Z. Xia, H. Li, H. Wang, J. Zhang, *Electrochim. Acta* **2008**, *53*, 5315-5321.

215. S.-J. Lim, G.-G. Park, J.-S. Park, Y.-J. Sohn, S.-D. Yim, T.-H. Yang, B. K. Hong, C.-S. Kim, *Int. J. Hydrogen Energy* **2010**, *35*, 13111-13117.

216. J.-M. Le Canut, R. Latham, W. Mérida, D. A. Harrington, *J. Power Sources* **2009**, *192*, 457-466.

217. H. P. L. H. van Bussel, F. G. H. Koene, R. K. A. M. Mallant, *J. Power Sources* **1998**, *71*, 218-222.

218. K. Jiao, X. Li, *Prog. Energy Combust. Sci.* **2011**, *37*, 221-291.

219. Q. Yan, H. Toghiani, J. Wu, *J. Power Sources* **2006**, *158*, 316-325.

220. S. Asghari, A. Mokmeli, M. Samavati, *Int. J. Hydrogen Energy* **2010**, *35*, 9283-9290.

221. G. H. Mousa (Simon Fraser University), J. W. De Vaal (Ballard Power Systems Inc), F. Golnaraghi (Ballard Power Systems Inc), US 10 581 099 B2, **2020**.

222. J. Zhang, Y. Tang, C. Song, J. Zhang, *J. Power Sources* **2007**, *172*, 163-171.

223. Q. Zhang, R. Lin, L. Técher, X. Cui, *Energy* **2016**, *115*, 550-560.

224. X. Yuan, J. C. Sun, M. Blanco, H. Wang, J. Zhang, D. P. Wilkinson, *J. Power Sources* **2006**, *161*, 920-928.

225. Y. Oono, T. Fukuda, A. Sounai, M. Hori, *J. Power Sources* **2010**, *195*, 1007-1014.

226. N. Wakabayashi, M. Takeichi, M. Itagaki, H. Uchida, M. Watanabe, *J. Electroanal. Chem.* **2005**, *574*, 339-346.

227. A. Damjanovic, *J. Electroanal. Chem.* **1993**, *355*, 57-77.

228. C. Song, J. Zhang in *PEM Fuel Cell Electrocatalysts and Catalyst Layers*, (Eds.: J. Zhang), Springer, London, **2008**, pp. 89-134.

229. H. Xu, Y. Song, H. R. Kunz, J. M. Fenton, *J. Electrochem. Soc.* **2005**, *152*, A1828-A1836.

230. Y. Liu, M. W. Murphy, D. R. Baker, W. Gu, C. Ji, J. Jorne, H. A. Gasteiger, *J. Electrochem. Soc.* **2009**, *156*, B970-B980.

231. F. A. Uribe, T. E. Springer, S. Gottesfeld, *J. Electrochem. Soc.* **1992**, *139*, 765-773.

232. C. Song, Y. Tang, J. L. Zhang, J. Zhang, H. Wang, J. Shen, S. McDermid, J. Li, P. Kozak, *Electrochim. Acta* **2007**, *52*, 2552-2561.

233. A. A. Kulikovsky, *J. Electroanal. Chem.* **2014**, *720–721*, 47-51.

234. R. Makharia, M. F. Mathias, D. R. Baker, *J. Electrochem. Soc.* **2005**, *152*, A970-A977.

235. B. P. Setzler, T. F. Fuller, *J. Electrochem. Soc.* **2015**, *162*, F519-F530.

236. S. K. Roy, M. E. Orazem, B. Tribollet, *J. Electrochem. Soc.* **2007**, *154*, B1378-B1388.

237. S. Watzele, A. S. Bandarenka, *Electroanalysis* **2016**, *28*, 2394-2399.

238. A. S. Bondarenko, I. E. L. Stephens, L. Bech, I. Chorkendorff, *Electrochim. Acta* **2012**, *82*, 517-523.

239. A. Kulikovsky, *Phys. Chem. Chem. Phys.* **2020**, *22*, 19131-19138.

240. I. A. Schneider, S. A. Freunberger, D. Kramer, A. Wokaun, G. G. Scherer, *J. Electrochem. Soc.* **2007**, *154*, B383-B388.

241. A. Bayrakçeken, S. Erkan, L. Türker, I. Eroğlu, *Int. J. Hydrogen Energy* **2008**, *33*, 165-170.

242. İ. Fırtına, S. Güner, A. Albostan, *Int. J. Energy Res.* **2011**, *35*, 146-152.

243. A. P. Manso, F. F. Marzo, J. Barranco, X. Garikano, M. G. Mujika, *Int. J. Hydrogen Energy* **2012**, *37*, 15256-15287.

244. Y. Song, C. Zhang, C.-Y. Ling, M. Han, R.-Y. Yong, D. Sun, J. Chen, *Int. J. Hydrogen Energy* **2020**, *45*, 29832-29847.

245. Fujifilm, "Prescale film", can be found under https://www.fujifilm.com/products/prescale/prescalefilm/, **2020**.

246. Zahner Elektrik, "Electrochemical Workstations", can be found under http://zahner.de/, **2020**.

247. M. Kitamura, Y. Minamida, X. Zhao, Z. Noda, A. Hayashi, K. Sasaki, *ECS Trans.* **2014**, *64*, 755-762.

248. M. Edmundson, F. C. Busby, *ECS Trans.* **2011**, *41*, 661-671.

249. S. Herden, J. A. Hirschfeld, C. Lohri, M. Perchthaler, S. Haase, *J. Power Sources* **2017**, *364*, 449-457.

250. B. A. Boukamp, J. Ross Macdonald, *Solid State Ionics* **1994**, *74*, 85-101.

251. A. S. Bandarenka in *Lecture Notes on Impedance Spectroscopy. Measurement, Modeling and Applications*, Vol. 4 (Eds.: O. Kanoun), CRC Press, Tailor and Francis Group, London, **2013**, pp. 29-36.

252. R. Kraume, "S++ Simulation Services", can be found under http://www.splusplus.com/, **2007**.

253. S. Haase, M. Moser, J. A. Hirschfeld, K. Jozwiak, *J. Power Sources* **2016**, *301*, 251-260.

254. S. Herden, F. Riewald, J. A. Hirschfeld, M. Perchthaler, *J. Power Sources* **2017**, *355*, 36-43.

255. J. A. Hirschfeld, H. Lustfeld, M. Reißel, B. Steffen, *Int. J. Energy Res.* **2010**, *34*, 293-302.

256. M. Zhiani, S. Majidi, *Int. J. Hydrogen Energy* **2013**, *38*, 9819-9825.

257. M. Zhiani, S. Majidi, V. B. Silva, H. Gharibi, *Energy* **2016**, *97*, 560-567.

258. T. Lochner, L. Hallitzky, M. Perchthaler, M. Obermaier, J. Sabawa, S. Enz, A. S. Bandarenka, *Appl. Energy* **2020**, *260*, 114291.

259. X. R. Wang, Y. Ma, J. Gao, T. Li, G. Z. Jiang, Z. Y. Sun, *Int. J. Hydrogen Energy* **2020**, in press, DOI 10.1016/j.ijhydene.2020.06.211.

260. N. Yousfi-Steiner, Ph. Moçotéguy, D. Candusso, D. Hissel, A. Hernandez, A. Aslanides, *J. Power Sources* **2008**, *183*, 260-274.

261. T. J. Schmidt, J. Baurmeister, *J. Power Sources* **2008**, *176*, 428-434.

262. M. Heinzmann, A. Weber, E. Ivers-Tiffée, *J. Power Sources* **2019**, *444*, 227279.

263. M. Obermaier, A. S. Bandarenka, C. Lohri-Tymozhynsky, *Sci Rep* **2018**, *8*, 4933.

264. M. Ciureanu, R. Roberge, *J. Phys. Chem. B* **2001**, *105*, 3531-3539.

265. S. J. Andreasen, J. R. Vang, S. K. Kær, *Int. J. Hydrogen Energy* **2011**, *36*, 9815-9830.

266. M. Chandesris, C. Robin, M. Gerard, Y. Bultel, *Electrochim. Acta* **2015**, *180*, 581-590.

267. S. M. R. Niya, R. K. Phillips, M. Hoorfar, *J. Electroanal. Chem.* **2016**, *775*, 273-279.

268. W. R. Mérida Donis, "Diagnosis of PEMFC stack failures via electrochemical impedance spectroscopy", can be found under https://dspace.library.uvic.ca//handle /1828/10312, **2018**.

269. T. Ogawa (Toyota Jidosha Kabushiki Kaisha), Y. Naganuma (Toyota Jidosha Kabushiki Kaisha), US 9 793 561 B2, **2017**.

270. T. H. Min (Hyundai Autron Co., Ltd.), US 9 945 911 B2, **2018**.

271. M. Matsumoto (Nissan Motor Co., Ltd.), K. Hoshi (Nissan Motor Co., Ltd.), T. Aoki (Nissan Motor Co., Ltd.), US 10 177 391 B2, **2019**.

272. M. Sinha (GM Global Technology Operations LLC), P. A. Rapaport (GM Global Technology Operations LLC), H. Yoshida (Honda Motor Co., Ltd.), S. Toyota (Honda Motor Co., Ltd.), Y.-H. Lai (GM Global Technology Operations LLC), US 10 218 018 B2, **2019**.

273. J. H. Jang, S. Jeon, J. H. Cho, S.-K. Kim, S.-Y. Lee, E. Cho, H.-J. Kim, J. Han, T.-H. Lim, *J. Electrochem. Soc.* **2009**, *156*, B1293-B1300.

274. S. Laribi, K. Mammar, Y. Sahli, K. Koussa, *Sustainable Energy Technologies and Assessments* **2019**, *34*, 35-42.

275. J. P. Sabawa, A. S. Bandarenka, *Results in Chemistry* **2020**, *2*, 100078.

276. P. T. Ha, H. Moon, B. H. Kim, H. Y. Ng, I. S. Chang, *Biosens. Bioelectron.* **2010**, *25*, 1629-1634.

277. C. Jeppesen, S. S. Araya, S. L. Sahlin, S. J. Andreasen, S. K. Kær, *Int. J. Hydrogen Energy* **2017**, *42*, 15851-15860.

278. G. A. Ragoisha, N. P. Osipovich, A. S. Bondarenko, J. Zhang, S. Kocha, A. Iiyama, *J. Solid State Electrochem.* **2010**, *14*, 531–542.

279. Y. Liu, M. Mathias, J. Zhang, *Electrochem. Solid-State Lett.* **2010**, *13*, B1-B3.

280. R. N. Carter, S. S. Kocha, F. Wagner, M. Fay, H. A. Gasteiger, *ECS Trans.* **2007**, *11*, 403-410.

281. I. D. Raistrick, D. R. Franceschetti, J. R. Macdonald in *Impedance Spectroscopy: Theory, Experiment, and Applications*, Vol. 2 (Eds.: E. Barsoukov, J. R. Macdonald), John Wiley & Sons, Inc., Hoboken, New Jersey, **2005**, pp. 27-128.

282. A. S. Bandarenka, *Analyst* **2013**, *138*, 5540-5554.

283. D. Natarajan, T. V. Nguyen, *AIChE J.* **2005**, *51*, 2599-2608.

284. S. A. Vilekar, R. Datta, *J. Power Sources* **2010**, *195*, 2241-2247.

285. J. Shan, P. Gazdzicki, R. Lin, M. Schulze, K. A. Friedrich, *Energy* **2017**, *128*, 357-365.

286. Y. Garsany, O. A. Baturina, K. E. Swider-Lyons, S. S. Kocha, *Anal. Chem.* **2010**, *82*, 6321-6328.

287. J. Rossmeisl, G. S. Karlberg, T. Jaramillo, J. K. Nørskov, *Faraday Discuss.* **2009**, *140*, 337-346.

288. W. R. Baumgartner, P. Parz, S. D. Fraser, E. Wallnöfer, V. Hacker, *J. Power Sources* **2008**, *182*, 413-421.

289. A. A. Kulikovsky, *J. Electroanal. Chem.* **2012**, *669*, 28-34.

290. W. Gu, P. T. Yu, R. N. Carter, R. Makharia, H. A. Gasteiger in, *Modeling and Diagnostics of Polymer Electrolyte Fuel Cells* **2010**, DOI 10.1007/978-0-387-98068-3_2.

291. F. N. Büchi, A. B. Geiger, R. P. Neto, *J. Power Sources* **2005**, *145*, 62-67.

292. S. Enz, M. Klages, C. Bergbreiter, M. Messerschmidt, H. Markotter, N. Kardjilov, I. Manke, J. Scholta, *ECS Trans.* **2013**, *51*, 215-226.

293. A. Mehmood, M.-G. An, H. Y. Ha, *Appl. Energy* **2014**, *129*, 346-353.

294. S. Thomas, S. C. Lee, A. K. Sahu, S. Park, *Int. J. Hydrogen Energy* **2014**, *39*, 4558-4565.

295. N. J. Steffy, S. V. Selvaganesh, M. Kumar L, A. K. Sahu, *J. Power Sources* **2018**, *404*, 81-88.